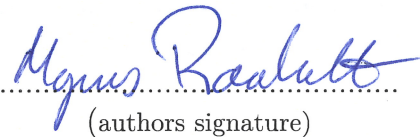




Universitetet
i Stavanger

Faculty of Science and Technology

Master's Thesis

Study program/specialization: Petroleum Engineering Reservoir Technology	Spring semester, 2019 Open access
Author: Raaholt, Magnus Kongestøl	 (authors signature)
Supervisors: Andersen, Pål Østebø Madland, Merete Vadla Korsnes, Reidar Inge	
Thesis title: Reactive Flow Simulation	
Credits: 30	
Keywords: Geochemical modelling Carbonates PHREEQC Strontianite Witherite	Number of pages: 77 + supplemental material: 8 Stavanger, 15th of June 2019

MASTER'S THESIS

REACTIVE FLOW SIMULATION

AUTHOR:

MAGNUS KONGESTØL RAAHOLT

MSc Student, Department of Energy Resources, University of Stavanger, Norway

Supervisors:

PÅL ØSTEBØ ANDERSEN

Assoc. Prof., Department of Energy Resources, University of Stavanger, Norway;
The National IOR Centre of Norway, University of Stavanger, Norway

MERETE VADLA MADLAND

Prof., Department of Energy Resources, University of Stavanger, Norway;
The National IOR Centre of Norway, University of Stavanger, Norway

REIDAR INGE KORSNES

Chief Engineer, Department of Energy Resources, University of Stavanger, Norway;
The National IOR Centre of Norway, University of Stavanger, Norway



University of
Stavanger

FACULTY OF SCIENCE AND ENGINEERING
DEPARTMENT OF ENERGY AND RESOURCES
2019

Abstract

Sea water-injection in carbonate formations leads to reactive processes that are linked to affecting oil recovery via wettability alteration and chemical compaction. The concentrations of divalent ions, such as Ca^{2+} , Mg^{2+} , and SO_4^{2-} , have proved to affect the stability of the carbonate matrix and the oil recovery. These effects are essential for chalk fields such as Ekofisk and Valhall on the Norwegian Continental Shelf (NCS).

This study considers history matching of recently performed brine injection experiments of three Mons Belgium chalk cores, with specific ion composition at reservoir (Ekofisk) conditions.

A 1D advection-dispersion-reaction (ADR) geochemical model is developed in PHREEQC, to capture the geochemical effects of Ba^{2+} , Ca^{2+} , Mg^{2+} , Sr^{2+} , and SO_4^{2-} in the injection brine. The model considers steady-state dissolution and precipitation reactions of anhydrite (CaSO_4), calcite (CaCO_3), celestite (SrSO_4), magnesite (MgCO_3), strontianite (SrCO_3), and witherite (BaCO_3). The minerals are selected based on a static model, experimental findings, and literature. Literature reaction rate kinetics give too high dissolution and precipitation rates, hence direct application does not match experimental results. To match experiments tuning parameters are introduced to the reaction rate equation, to reduce the literature reaction kinetic rates.

The model produces suitable calcite precipitation and magnesite precipitation, both considering effluent concentrations and post-flooding mineral distribution. The behaviour of witherite was captured, but its precipitating rate seems to have a higher meta-stable saturation, hence require a higher super-saturation for precipitation initiation. Moreover, at super-saturations beyond the meta-stable level, the precipitation rate accelerates faster, compared to calcite and magnesite. The lack of reaction kinetic data for strontianite introduces great uncertainty to the simulation. Consequently, simulations of Sr^{2+} injection sequences were adjusted to match effluents, but mineral distributions were not matched. Transient effluent behaviour during sulphate-bearing mineral precipitation was not matched.

Preface

This Master of Science thesis presents my graduating work, specializing in reservoir technology. The focus of this research is improving the knowledge of geochemical alterations induced by reactive flow in chalk material, by developing a model to match experimental results.

I want to express my gratitude towards Pål Ø. Andersen for technical supervision, Reidar I. Korsnes for providing experimental results, and Mona W. Minde for performing and explaining the SEM analysis.

This thesis is not only the result of one semester of hard work. It is the result of 5 years of academic studies at the University of Stavanger, thorough and well written scientific literature, personal experience from internships in Statoil (Equinor) and Aker BP, both academic and non-academic discussion with fellow students, and last but not least, the support from friends and family.

Without the possibility of discussing academic problems with professors and fellow students, I would not have achieved the same level knowledge.

Without fellow students from other disciplines and professionals from the industry, my know-how would not have reached this far.

Without the support from friends and family, I would not have had the time and energy to complete this work.

I want to share with you, a great quote, from a fantastic book, written by a genius author:

We never know which lives we influence, or when, or why.

- Stephen King (2012), 11/22/63

Thank you, for influencing mine.

Contents

Abstract	i
Preface	ii
List of Figures	vi
List of Tables	vii
Nomenclature	viii
1 Introduction	1
2 Interpreted Experimental System and Dataset	5
2.1 Chalk Core Flooding by Andersen et al. (2018)	7
2.2 Chalk Core Flooding by Korsnes and Madland (2017)	7
2.3 Dataset From Experimental Results	8
2.4 Core Analysis After Flooding	11
2.4.1 Whole-rock Geochemical Analysis	11
2.4.2 Electron Microscopy Analysis	13
3 Theory	14
3.1 Chemistry	14
3.1.1 Chemical Equilibrium	14
3.1.2 The Carbonic Acid System	15
3.1.3 Charge Balance	17
3.1.4 Mineral Dissolution and Precipitation	17
3.2 Transport Equations	19
3.2.1 Advection	19
3.2.2 Diffusion	19
3.2.3 Dispersion	20
3.2.4 Initial State	21
3.2.5 Boundary Conditions	21
3.2.6 Advection-Dispersion-Reaction Equation	21
3.3 PHREEQC	23
3.3.1 Transport Calculations	23
4 Methodology	24
4.1 Static Model	24
4.2 Dynamic Model	24

5	Modeling Methodology	25
5.1	Static Model	25
5.2	Dynamic Model	25
5.2.1	Defining the Initial System	25
5.2.2	Minerals Included in Model	26
5.2.3	Dispersion	27
5.2.4	Kinetic Reaction Rates	27
6	Results and Discussion	32
6.1	Mineral Selection from the Static Model	32
6.2	Kinetic Parameters in the Dynamic Model	37
6.2.1	Dispersion	37
6.2.2	Tuning of Reaction Kinetic Parameters	39
6.3	Full Experiment Simulations	56
6.3.1	Mineral Distribution	65
6.3.2	Dissolution-Precipitation Behaviour	66
7	Conclusion	69
7.1	Future Work	70
	Bibliography	71
A	Electron Microscopy Analysis	A1
B	Poster Presentations	B1

List of Figures

2.1	Injected and effluent concentrations of divalent ions from the MO10 core (Andersen et al., 2018)	8
2.2	Injected and effluent concentrations of divalent ions from the M12 core, from the first 5 flooding sequences (Korsnes and Madland, 2017).	9
2.3	Injected and effluent concentrations of divalent ions from the M12 core, from the 5 last flooding sequences (Korsnes and Madland, 2017).	9
2.4	Injected and effluent concentrations of divalent ions from the M9 core (Korsnes and Madland, 2017).	10
2.5	Illustration of how core was cut and the slices are enumerated after flooding.	11
3.1	The carbonate phase plotted against pH in a simplified system, at ambient temperature.	16
3.2	Regimes of crystal growth.	18
3.3	Linearised 1D reservoir.	19
6.1	Normalized Cl concentrations for brines used when flooding the M12 core.	37
6.2	Normalized Cl concentrations in accordance with equation (5.3) for brines used when flooding the M12 core.	38
6.3	Demonstration of the effect of using $p < 1$ comparing with mineral distribution of MO10.	41
6.4	Matching the distribution of magnesite content relative to the outlet slice, with the simulated relative kinetic precipitation rate of magnesite.	41
6.5	Best match of MO10 effluent concentration.	42
6.6	Best match of M12 effluent concentration of flooding with brine 4 and 6.	43
6.7	Best match of M12 effluent concentration of flooding with brine 7.	44
6.8	Matching of effluent Sr^{2+} concentration in M9 brine 3, with zero witherite (BaCO_3) precipitation rate.	45
6.9	The effluent concentrations of M12 from brine 8 sequence, using RF_{str}^{prec} from the M9 matching.	46
6.10	Matching of effluents from M12 brine 8 by adjusting RF_{mag}^{dis} and RF_{str}^{prec}	47
6.11	Matching the effluents from last injection sequence in M12 using $p_{wit} = 0.5$	48
6.12	Poor matching M9 effluents using parameters adjusted for M12, with $p_{wit} = 0.5$	49
6.13	M9 matching brine 3, using final tuning parameters for calcite (CaCO_3), strontianite (SrCO_3) and witherite (BaCO_3).	50
6.14	M12 matching brine 10, using final tuning parameters for calcite (CaCO_3), magnesite (MgCO_3), strontianite (SrCO_3) and witherite (BaCO_3).	51
6.15	M12 matching brine 9 sequence 8, using final tuning parameters for calcite (CaCO_3), magnesite (MgCO_3), strontianite (SrCO_3) and witherite (BaCO_3).	52

6.16	M12 matching brine 9 sequence 10, using final tuning parameters for calcite (CaCO_3), magnesite (MgCO_3), strontianite (SrCO_3) and witherite (BaCO_3).	52
6.17	Demonstrating one of the several simulations used to capture the geochemical alteration from brine 5 flooding of M9, which did not give a great match.	55
6.18	Final simulated results in the MO10 core.	57
6.19	Final simulated results in the 5 first sequences of the M12 core.	58
6.20	Final simulated results in the last 5 sequences of the M12 core.	59
6.21	Final simulated results in the M9 core.	60
6.22	Comparing the computed MgO distribution with geochemically determined distribution of MO10.	61
6.23	Comparing the computed CaO distribution with geochemically determined distribution of MO10.	61
6.24	Comparing the computed MgO distribution with geochemically determined distribution of M12.	62
6.25	Comparing the computed CaO distribution with geochemically determined distribution of M12.	62
6.26	Comparing the computed Ba distribution with geochemically determined distribution of M12.	63
6.27	Comparing the computed Sr distribution with geochemically determined distribution of M12.	63
6.28	Comparing the computed CaO distribution with geochemically determined distribution of M9.	64
6.29	Comparing the computed Ba distribution with geochemically determined distribution of M9.	64
6.30	Comparing the computed Sr distribution with geochemically determined distribution of M9.	65
A.1	EDS of the inlet slice of M9 indicating Sr bearing sulphate.	A2
A.2	EDS of the inlet slice of M12 indicating calcite.	A3
A.3	EDS of the inlet slice of M12 indicating Sr bearing carbonate.	A4
A.4	EDS of the inlet slice of M12 indicating Ba bearing carbonate.	A5

List of Tables

2.1	Composition of brines used in experiments.	5
2.2	Physical properties of outcrop chalk coress used in flooding experiments by Andersen et al. (2018) (MO10) and Korsnes and Madland (2017) (M9 and M12).	6
2.3	Distribution of most relevant elements from ICP-MS analysis of core from Andersen et al. (2018).	12
2.4	Distribution of most relevant elements from ICP-MS analysis performed on cores from Korsnes and Madland (2017).	12
5.1	Initial calcite concentration and reactive surface area per litre pore volume for each core, calculated using equation (5.1) and (5.2).	26
5.2	Dissolution reaction of included minerals.	26
5.3	Properties of the minerals used in dynamic model. K_{eq} is the equilibrium constant, ρ the mineral density, MW the molecular weight.	27
6.1	Mineral saturation indexes, SI , in static equilibrium between brines listed in table 2.1 with pure calcite, CaCO_3	36
6.2	Tuning parameters summarized.	55
6.3	Re-presentating composition of brines used in experiments.	56
7.1	Carbonate tuning parameters summarized.	69
A.1	Semi-quantification of elements from EDS analysis.	A1

Nomenclature

ADR Advection-diffusion-reaction

b.d.l. Below detection limit

BSE Backscattered electrons

DW Distilled water

EDS Energy dispersive X-ray spectroscopy

IAP Ion activity product

ICP Inductively coupled plasma

ICP-MS Inductively coupled plasma mass spectrometry

LMA Law of mass action

LMB Lattice Boltzmann method

MS Mass spectrometry

NCS Norwegian Continental Shelf

ND Not defined

PV Pore volume

SE Secondary electrons

SEM Scanning electron microscopy

TIC Total inorganic carbon

TOT/C Total carbon *wt%*

TOT/S Total sulphide *wt%*

TST Transition state theory

anh Anhydrite, CaSO_4

cal Calcite, CaCO_3

cel Celestite, SrSO_4

mag Magnesite, MgCO_3

str	Strontianite, SrCO ₃	
wit	Witherite, BaCO ₃	
acid	Acidic mechanism	
base	Basic/alkaline mechanism	
dis	Dissolve	
eq	Equilibrium	
neu	Neutral mechanism	
prec	Precipitate	
α_L	Dispersion coefficient	
Δ_{charge}	Charge balance	
\dot{r}	Reaction rate	$\frac{mol}{s}$
$\frac{A_0}{V}$	Initial reactive surface area per litre pore volume	$\frac{m^2}{litre PV}$
γ	Activity coefficient	
Ω	Saturation ratio	
D_L	Hydrodynamic dispersion coefficient	$\frac{m^2}{s}$
E_a	Activation energy	$\frac{kJ}{mol}$
K	Equilibrium constant	
SI	Saturation index	
A	Pre-exponential Arrhenius factor	$\frac{mol}{m^2 s}$
A'	Temperature dependent coefficient used to determine activity coefficients	
B	Temperature dependent coefficient used to determine activity coefficients	
I	Ionic strength	
k	Kinetic reaction rate constant	$\frac{mol}{m^2 s}$
m	Concentration	$\frac{mol}{litre}$
p	Empiric tuning parameter	
q	Empiric tuning parameter	

R	The universal gas constant,	$8.3145 \frac{J}{mol \cdot Kelvin}$
SA	Available surface area	m^2
SSA	Specific surface area	$\frac{m^2}{g}$
T	Temperature	Kelvin or °C
Z	Valence/charge number	

1 | Introduction

On the Norwegian continental shelf (NCS) carbonate fields, such as Ekofisk and Valhall, are experiencing seabed subsidence due to reservoir compaction. Reservoir compaction is affected by more than increased effective stress on the rock matrix, linked to fluid production and pore pressure reduction, such as chemically induced mechanical instabilities. Both Ekofisk and Valhall were initially produced by pressure depletion until seawater injection was initiated in 1987 and 2004, respectively (Hermansen et al., 2000; Kristiansen and Plischke, 2010). Seawater injection was intended to re-pressurize the reservoirs and halt further subsidence. Even though the reservoirs were re-pressurized, compaction continued (Sulak and Danielsen, 1988; Ruddy et al., 1989; Sylte et al., 1999; Hermansen et al., 2000; Kristiansen and Plischke, 2010; Bjørlykke, 2015).

Seawater injection is a well-proven method to improve oil recovery in carbonate reservoirs (Nagel, 2001; Fathi et al., 2011; Austad, 2013; Minde, 2018), and mechanisms related to the method have extensively been studied. Water weakening is one of the studied mechanisms, as it causes an engineering challenge for field development and enhances the compaction drive mechanism (Sulak and Danielsen, 1988; Sylte et al., 1999; Cook et al., 2001; Nagel, 2001). Laboratory experiments of core flooding have demonstrated that the composition of the injected brine is an essential factor when flooding carbonate rock (Zhang et al., 2007; Puntervold, 2008; Fathi et al., 2011; Madland et al., 2011; Austad, 2013; Geitle, 2013; Megawati et al., 2013, 2015; Korsnes and Madland, 2017; Andersen et al., 2018; Minde, 2018; Atree-Williams et al., 2019). The concentration of divalent ions, such as Ca^{2+} , Mg^{2+} , and SO_4^{2-} , has proved to affect the stability of the carbonate matrix and the oil recovery (Zhang et al., 2007; Puntervold, 2008; Fathi et al., 2011; Madland et al., 2011; Andersen et al., 2012; Austad, 2013; Geitle, 2013; Megawati et al., 2013, 2015; Zimmermann et al., 2015; Korsnes and Madland, 2017; Minde, 2018).

In the petroleum industry, dissolution and precipitation of minerals are associated with permeability reduction, scaling, and wellbore instability. Multiple experiments have proved these petrophysical alterations, and methods to reduce these unwanted effects have thoroughly been investigated (Morse and Mackenzie, 1990; Todd and Yuan, 1990; Li et al., 1995; Bedrikovetsky et al., 2004; Fjær et al., 2008; Jordan et al., 2008; Austad, 2013; Chagneau et al., 2015). Observations from Korsnes and Madland (2017) where the creep compaction rate of outcrop chalk cores reduced as Ba^{2+} and Sr^{2+} brines were injected indicated that the incorporation of barium and strontium ions in the carbonate lattice re-stabilize the carbonate matrix. Another interesting observation from Korsnes and Madland (2017) was that even though the chalk strength increased, the permeability was not crucially reduced. In the following sequence in the same experiment, SO_4^{2-} was injected, causing severe permeability reduction. Consequently, indicating that injection of Ba^{2+} and Sr^{2+} brines, absent of SO_4^{2-} , the chalk matrix deformation is retarded, whilst the permeability is preserved. On NCS it

is common practice to inject seawater, which contains sufficiently high amounts of SO_4^{2-} to cause severe scaling (Todd and Yuan, 1990; Jordan et al., 2008; Temple et al., 2019). Consequently, water treatment or scale inhibition are required to preserve permeability in carbonate reservoirs. Water treatment equipment, such as the Seabox™, can reduce the sulphate content of seawater, thus allowing for new long-term strategies for the choice of injection brine composition.

Many reactive flow experiments have demonstrated the effects of specific ions and ion compositions of the injection brine in flooding chalk cores (e.g. Heggheim et al. (2005); Zhang et al. (2007); Madland et al. (2011); Austad (2013); Megawati et al. (2013); Zimmermann et al. (2015); Megawati et al. (2015); Korsnes and Madland (2017); Andersen et al. (2018)), but what compositions that give the desired reactions in these complex systems remains unclear (Hiorth et al., 2013; Minde, 2018). To better understand the effects of specific ions and ion compositions, several kinetic models considering the dissolution-precipitation reaction rate of the general form:

$$\dot{r} = \pm k SA |1 - \Omega|^p, \quad (1.1)$$

have been developed and extensively studied during the past two decades (Evje et al., 2009; Andersen et al., 2012; Atree-Williams et al., 2019). The models are used to match experimental results, such as effluent concentrations, post-flooding mineral distribution, and porosity and permeability variations (Cook et al., 2001; Evje et al., 2009; Andersen et al., 2012; Hiorth et al., 2013; Meling, 2013; Chagneau et al., 2015; Korrani et al., 2015; Pedersen et al., 2016; Andersen et al., 2018; Atree-Williams et al., 2019).

Evje et al. (2009) developed a 1D model to capture and couple geochemical alterations induced by MgCl_2 -brine flooding in cores of chalk, which considered calcite, and magnesite. The model consisted of advection-diffusion-reaction (ADR) equations for the ions, and differential equations for the minerals included. Evje et al. (2009) matched the steady-state effluent concentrations, but did not capture the transient state reactions. Madland et al. (2011) used the 1D model by Evje et al. (2009) to match core flooding experiments, and proposed that gradual transition towards steady-state could be explained by ion exchange processes, where desorption of Ca^{2+} and adsorption of Mg^{2+} occur. The 1D model was further developed by Andersen (2010) to include dolomite and let porosity and permeability be functions of the rock composition. Later, the model was improved to include more complex elements, such as dissolution of gaseous CO_2 into the brine, aqueous complexation, and the effects of cation exchange of Ca^{2+} , Mg^{2+} , and Na^+ , by Andersen et al. (2012). These later improvements made the model more relevant for the interpretation of water-rock chemical interaction related to water weakening effects (Andersen et al., 2012).

Hiorth et al. (2013) demonstrated that the integration of a Lattice Boltzmann method (LBM) with a geochemical model makes it possible to simulate local changes, such as mineral dissolution-precipitation reactions, and surface charge, complexation, and potentials. As discussed by Zimmermann et al. (2015), this model makes it possible to predict the effluents and the location of where

precipitation and dissolution occur. Pedersen et al. (2016) further investigated LBM, and further developed it to include the effect of surface coverage, which reduces the dissolution rate. The model considered calcite and magnesite and was used to match a long duration MgCl_2 flooding experiment where the initially pure calcite core was nearly completely converted to magnesite. Based on the effect of surface coverage, it was concluded that the dissolution rate had to be reduced dynamically as magnesite was precipitated to match experimental results. Altree-Williams et al. (2019) developed an analytical 1D model for one phase flow in porous media, accounting for dissolution. It was concluded that experimental data were better matched when the available surface area was varied by a function compared to a constant surface area.

In the literature, there are available compilations of kinetic parameters, such as Palandri and Kharaka (2004), Declercq and Oelkers (2014), and Marty et al. (2015). Such databases are necessary to develop reaction kinetic models, due to the requirement of reliable and consistent reaction kinetic input parameters, that make the foundation. In these mentioned databases, the authors have collected many experimental results and used these to predict the parameters presented.

Using reaction rate equations similar to equation (1.1), the kinetic reaction rate constants based experimental methods, such as bulk powder experiments and rotating disc, give too high reaction rates (Blount, 1974; Pedersen et al., 2016; Andersen et al., 2018). Blount (1974) addressed the formation rate difference of laboratory synthesized minerals, using clean equipment, and the not *laboratory-clean* mineral formation. Moreover, both Pedersen et al. (2016) and Andersen et al. (2018) had to adjust the literature reaction rates to match experimental results. Pedersen et al. (2016) suggested that the reaction kinetics for calcite have to be reduced by a factor of $\sim 10^4$, and $\sim 10^2$ for magnesite. Andersen et al. (2018) reduced the reaction rate constants for calcite and magnesite by $\sim 10^7$ and $\sim 10^4$, respectively.

Objective

The objective of this thesis is to improve the knowledge of geochemical alterations induced by reactive flow in porous chalk media by developing a 1D advection-dispersion-reaction (ADR) model. The ADR model will be developed in PHREEQC (an aqueous geochemical simulation tool) and is used to history match experimental results of three Mons Belgium outcrop chalk cores. The cores were injected with specific brine compositions at Ekofisk conditions, i.e. 130°C , to induce geochemical and geomechanical alterations. The scope is to use literature defined dissolution-precipitation rate kinetic parameters to history match and study steady-state effluent concentrations and post-flooding mineral distribution.

The novelty of this work is to further improve geochemical modeling by introducing the barium and strontium carbonates, witherite (BaCO_3) and strontianite (SrCO_3). These carbonates are potential precipitants in carbonate flooding systems, but rarely considered. When Ba^{2+} and Sr^{2+} are consid-

ered in experimental work and modeling, they are regularly related to the formation of sulphates, such as barite (BaSO_4) and celestite (SrSO_4), and formation damage (Li et al., 1995; Rocha et al., 2001; Bedrikovetsky et al., 2004; BinMerhdah et al., 2010; Kamari et al., 2014). Nevertheless, as demonstrated by Korsnes and Madland (2017), when Ba^{2+} and Sr^{2+} were injected into chalk cores, in the absence of sulphate, the compaction rate was reduced or completely stalled. If these ion-induced stabilizing effects are highly repeatable, this may adjust the focus of chalk-matrix experiments towards the formation of barium and strontium bearing carbonates. This knowledge can further be applied to predict, prevent, and control carbonate instability problems.

Structure

Here the thesis structure is presented. In chapter 2, the experimental set-up, material, and results from Andersen et al. (2018) and Korsnes and Madland (2017) for the evaluated cores are presented. The results used in the evaluation are effluent concentrations, geochemical analysis, and scanning electron microscopy (SEM) imaging. By using the theory presented in chapter 3, such as chemistry related to dissolution and precipitation of minerals, and transportation calculations, the numerical method used in PHREEQC (i.e. the software used) is presented. In chapter 4, the matching methodology is summarized in bullet points, and it is more thoroughly presented in the modeling chapter, that is chapter 5. The results from both the static and the dynamic model are presented and discussed in chapter 6. Chapter 7 is the conclusion, and in section 7.1 suggested experimental work and elements that can improve the model and the geochemical knowledge are presented. In the appendix results from scanning electron microscopy (SEM) imaging are of M9 and M12 are presented, followed by two posters used to present this thesis on the IOR NORWAY 2019 conference, and the graduation ceremony.

2 | Interpreted Experimental System and Dataset

In this chapter, the experimental material, flooding procedure, and experimental results from Andersen et al. (2018) and Korsnes and Madland (2017) are presented. The MO10 core from Andersen et al. (2018) was prior to this study evaluated through geochemical analysis and scanning electron microscopy (SEM) analysis. Thus, the experimental results presented herein are previously published in Andersen et al. (2018). The effluent concentrations and physical properties of M9 and M12 are retrieved from Korsnes and Madland (2017), whilst geochemical and SEM analysis were performed to support this study.

The outcrop chalk cores evaluated in this thesis are from the Harmignies quarry in Mons, Belgium. The Mons chalk is of Campanian age and has a 99 wt% clean calcium carbonate content and specific surface area of 1.81 m²/g (Megawati et al., 2015; Andersen et al., 2018). The brine compositions and physical core properties are summarized in tables 2.1 and 2.2, respectively.

Brine	1	2	3	4	5	6	7	8	9	10	MgCl ₂
Ions [<i>mol/L</i>]											
Cl ⁻	0.657	0.585	0.633	0.561	0.561	0.561	0.465	0.465	0.525	0.465	0.438
Na ⁺	0.657	0.633	0.585	0.561	0.561	0.513	0.225	0.225	0.405	0.225	
SO ₄ ²⁻		0.024		0.024	0.024						
Mg ²⁺				0.024		0.024	0.120				0.219
Ca ²⁺					0.024					0.120	
Sr ²⁺			0.012					0.120			
Ba ²⁺			0.012						0.060		
Flooding sequence in..											
MO10											1
M9	1,3		2		4						
M12	1,3	2		4		5	6	7	8,10	9	

Table 2.1: Composition of brines used in experiments by Korsnes and Madland (2017) (Brine 1-10), and Andersen et al. (2018) (MgCl-brine).

	Diameter [mm]	Length [mm]	Matrix mass [g]	Porosity, ϕ [%]	Yield stress [MPa]
MO10	38.1	70.3	125.58	41.5	10.5
M9	37,0	73.36	121.91	42.55	9.2
M12	36.97	73.77	122.41	42.66	10.5

Table 2.2: Physical properties of outcrop chalk coress used in flooding experiments by Andersen et al. (2018) (MO10) and Korsnes and Madland (2017) (M9 and M12).

Megawati et al. (2015) demonstrated that hydrostatic stress condition gives good repeatability, consequently making results highly comparable. The flooding experiments were performed at (near) isotropic conditions, in triaxial cells (see Andersen et al. (2018) or Korsnes and Madland (2017) for details regarding the *near* isotropic condition). To compare results to (Ekofisk) reservoir conditions, the test temperature was set to 130°C, and 0.7 MPa pore pressure. The flooding rate was set to 0.023 ml/min, i.e. close to 1 PV/day, where 1 PV is the initial pore volume.

The flooding experiment was done in a hydraulically operated triaxial cell, equipped with a heating jacket with an external regulating system, and three high-pressure pumps. The heating jacket enables the test to be performed at elevated temperatures. A linear variable differential transformer (LVDT) was used to measure axial deformation. A back-pressure regulator was installed to control the pore pressure, enabling continuous sampling of the effluent. To analyze the effluent samples a DIONEX ICS-5000 ion chromatograph (IC) was used. The IC uses IonPac CS19 exchanger column and IonPac AS20 exchanger column for cations and anions measurements, respectively. The ion concentration was determined by using external standards (Korsnes and Madland, 2017).

Both Andersen et al. (2018) and Korsnes and Madland (2017) followed similar flooding procedures for the three cores considered in this thesis. After installing the cores in the triaxial cell, the three cores considered followed this procedure:

1. Increase confining pressure to 0.5 MPa and clean core with a minimum of 3 pore volumes (PV) of distilled water (DW).
2. Simultaneously increase confining pressure to 1.2 MPa, and regulate the back pressure regulator such that pore pressure equal 0.7 MPa.
3. Injection rate was set to 0.023 ml/min, i.e. 1 PV/day. This flow rate was kept for the rest of the experiment.
4. Displace DW and saturate with Brine 1 (NaCl-brine, listed in table 2.1) for M9 and M12, and the MgCl₂-brine (listed in table 2.1) for MO10. MO10 was only flooded with the MgCl₂-brine.
5. Increase temperature to 130°C and let equilibrate over night.
6. Perform isotropic loading beyond yield stress and let the core creep compact.

7. For M9 and M12 start flooding with different brines, in the sequence stated in section 2.2, with injection rate of 1 PV/day, while still creep compacting.
8. After the flooding experiments the cores were flooded with 3 PVs of DW, to avoid precipitation of salt during drying.

2.1 Chalk Core Flooding by Andersen et al. (2018)

Andersen et al. (2018) flooded five different chalk core types: Kansas (USA, Niobrara), Mons (Belgium, Harmignies), Liège (Belgium, Hallembaye), Aalborg (Denmark, Rørdal), and Stevns Klint (Denmark, Sigerselv). Herein the MgCl_2 flooded Mons chalk is presented, used, and evaluated. The petrophysical properties of the MO10 core are presented in table 2.1, and the results in the following sections.

Key Observations

- Magnesite was identified in increasing amounts in the slice 1 to 3, and minor amounts in slice 4 to 7.

2.2 Chalk Core Flooding by Korsnes and Madland (2017)

The petrophysical properties of the M9 and M12 Mons chalk cores are presented in table 2.2, and the flooding brines are presented in table 2.1. The M9 core was flooded with brine 1, 3, 1, and 5, whilst M12 was flooded with brine 1, 2, 1, 4, 6, 7, 8, 9, 10, and 9. Both in the respective order.

Key Observations

- No steady-state retention of SO_4^{2-} was observed in M12.
- Injection of Mg^{2+} as the only reactive component, the produced Ca^{2+} correspond with retained Mg^{2+} (brines 4 and 6 in M12).
- Flooding Ca^{2+} and SO_4^{2-} simultaneously, equal amounts of both specie was retained (brine 5 M9). Shortly after both injected components reached injected concentrations, both dropped and the core was clogged.
- Using Sr^{2+} as only reactive component injected, 2/3 were retained, and the sum of produced Ca^{2+} and Mg^{2+} corresponded with the amount of retained Sr^{2+} .
- Injection of Ba^{2+} where Ca^{2+} , Mg^{2+} and Sr^{2+} were produced (brine 9, sequence 8), approximately 1/3 Ba^{2+} was retained.
- Injection of Ba^{2+} where Ca^{2+} was produced (brine 9, sequence 10), approximately 1/6 Ba^{2+} was retained, and corresponding amounts of Ca^{2+} were produced.

- Simultaneous injection of Sr^{2+} and Ba^{2+} with equal concentration, Sr^{2+} retained, whilst Ba^{2+} was produced at near injected concentration (brine 3 in M9).
- Flooding with brine 10 in M12, the effluents became very complex (see figure 2.3). The Ca^{2+} effluent, the injected divalent ion, increased gradually, never reaching a steady-state plateau. Ba^{2+} was back produced at an initial high concentration which gradually decreased to zero. Mg^{2+} effluent increased to a peak, almost mid sequence, and dropped again. Sr^{2+} effluent increased until it reached a plateau at the approximate same time as Ba^{2+} reaches zero, and Mg^{2+} peak.

2.3 Dataset From Experimental Results

In this section, the effluent concentrations are presented. To visualize what ions that are retained and gained/produced in each sequence, both the influent and effluent concentrations are plotted. Dotted lines plot the injected concentrations, and symbols plot the ion chromatograph (IC) measured effluents.

Since the concentrations of both Na^+ and Cl^- are relatively high compared to the other ions used, these are not presented. This is in accordance with how Andersen et al. (2018) and Korsnes and Madland (2017) present their results.

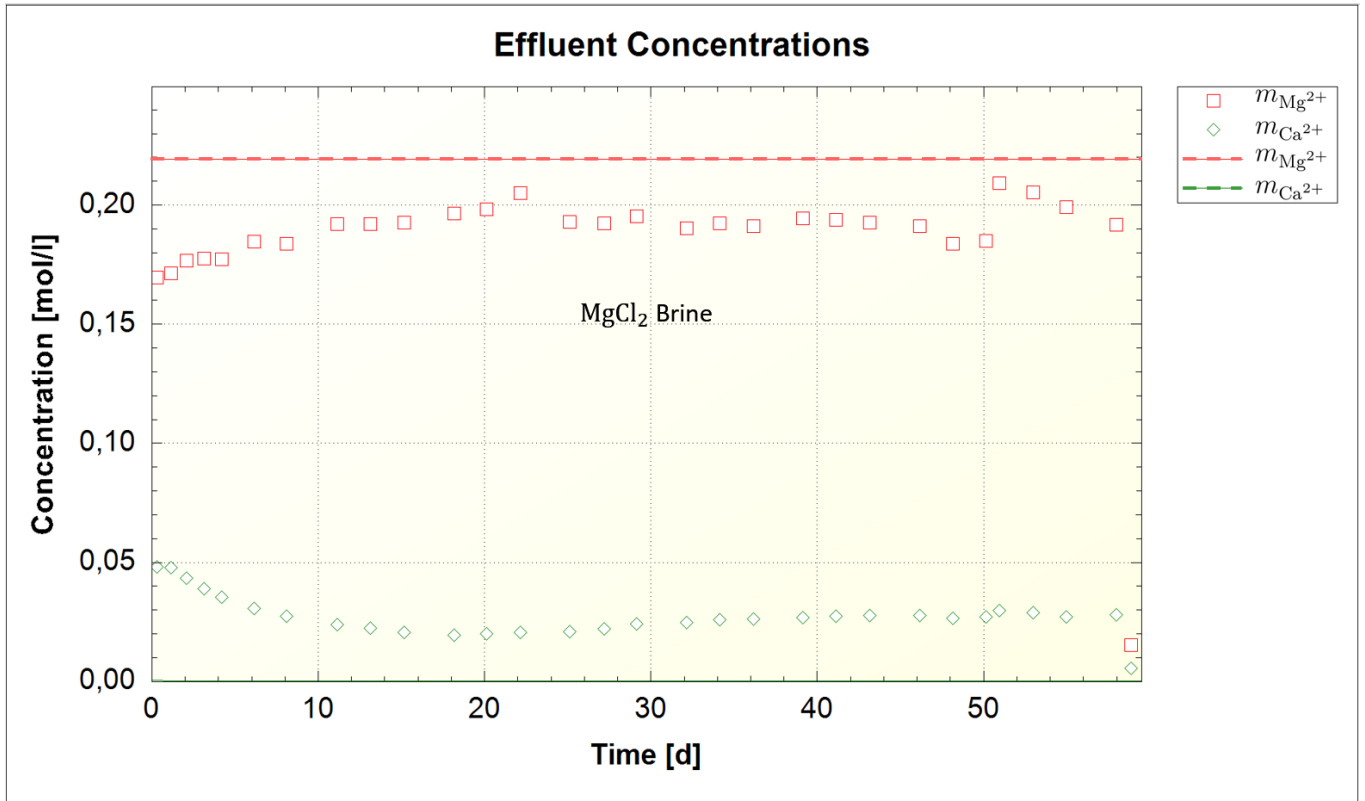


Figure 2.1: Injected and effluent concentrations of divalent ions from the MO10 core (Andersen et al., 2018). The data points are IC measured effluents, and the stapled lines demonstrate the injected concentration.

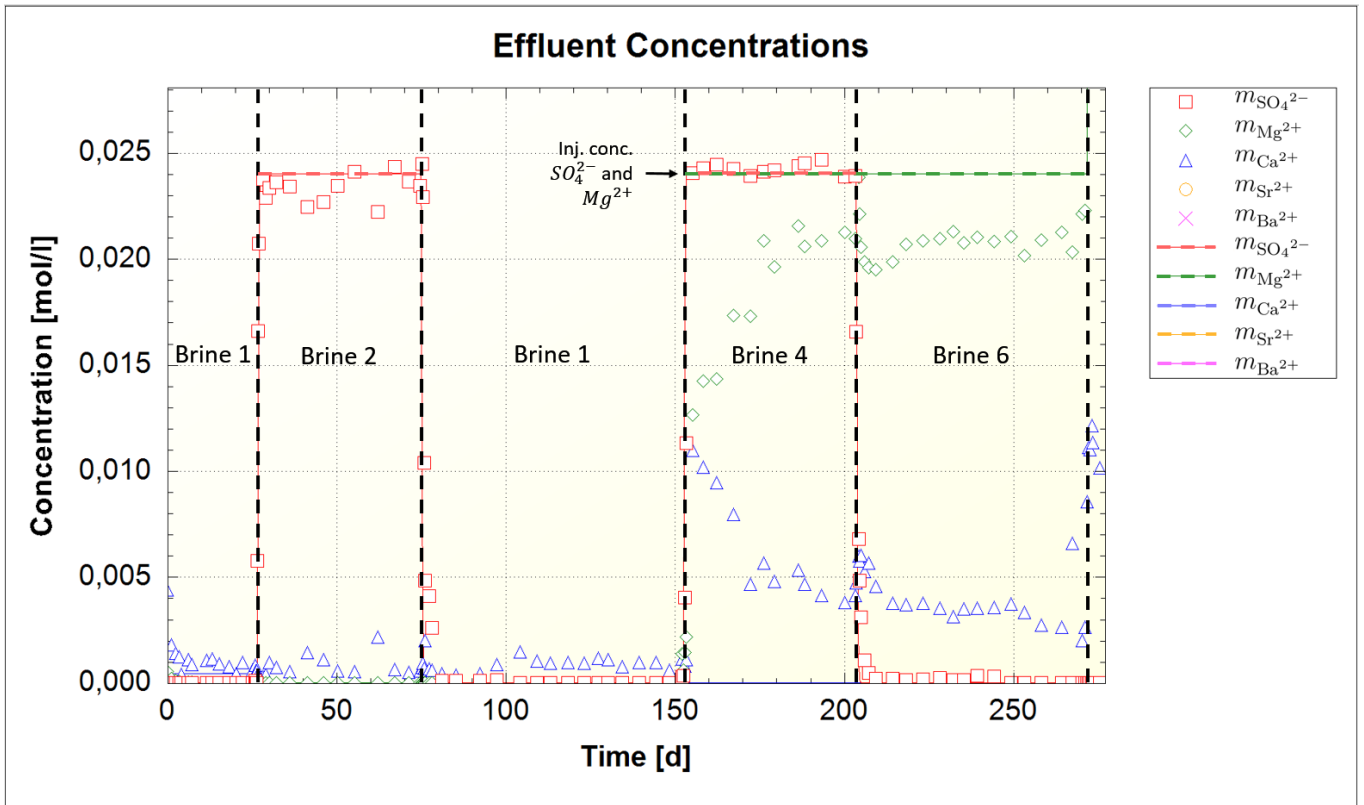


Figure 2.2: Injected and effluent concentrations of divalent ions from the M12 core, from the first 5 flooding sequences (Korsnes and Madland, 2017). The data points are IC measured effluents, and the stapled lines demonstrate the injected concentration.

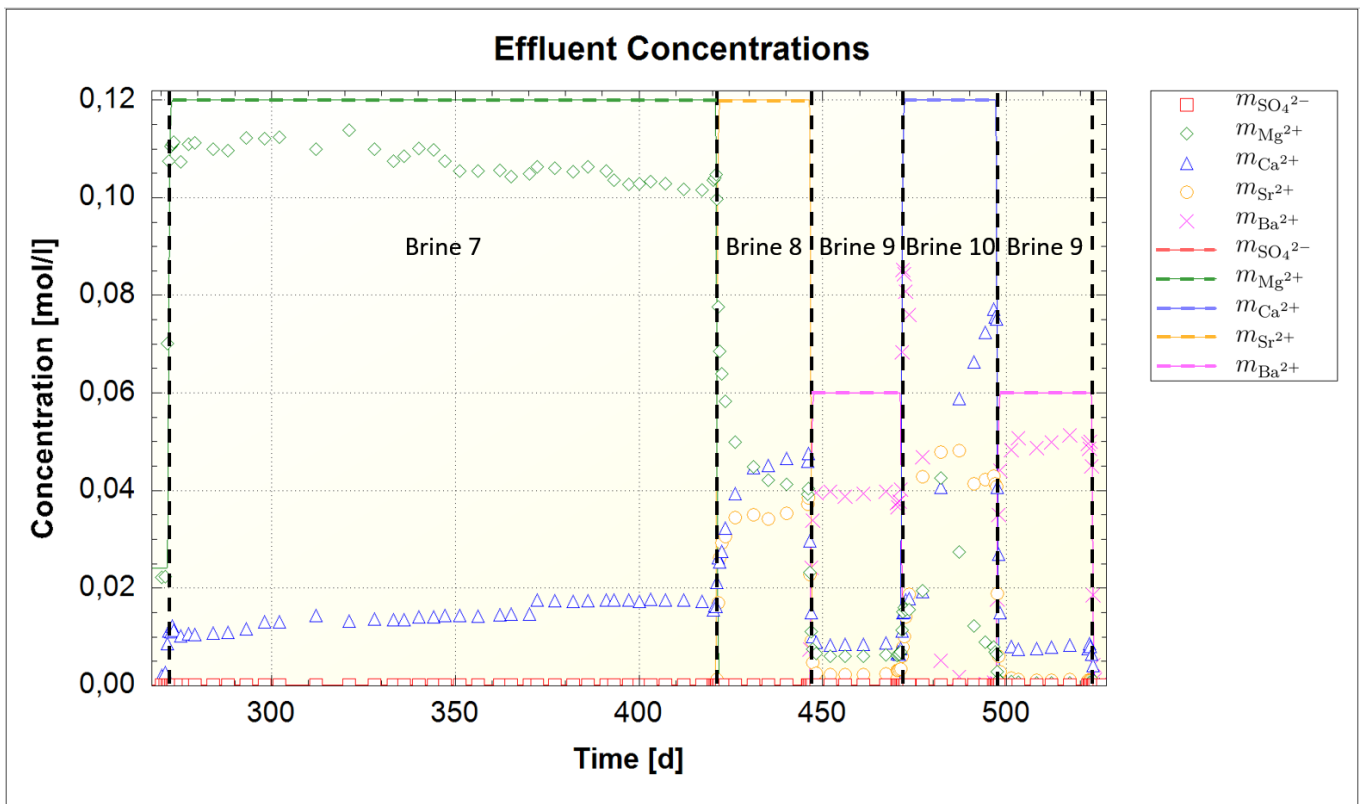


Figure 2.3: Injected and effluent concentrations of divalent ions from the M12 core, from the 5 last flooding sequences (Korsnes and Madland, 2017). The data points are IC measured effluents, and the stapled lines demonstrate the injected concentration.

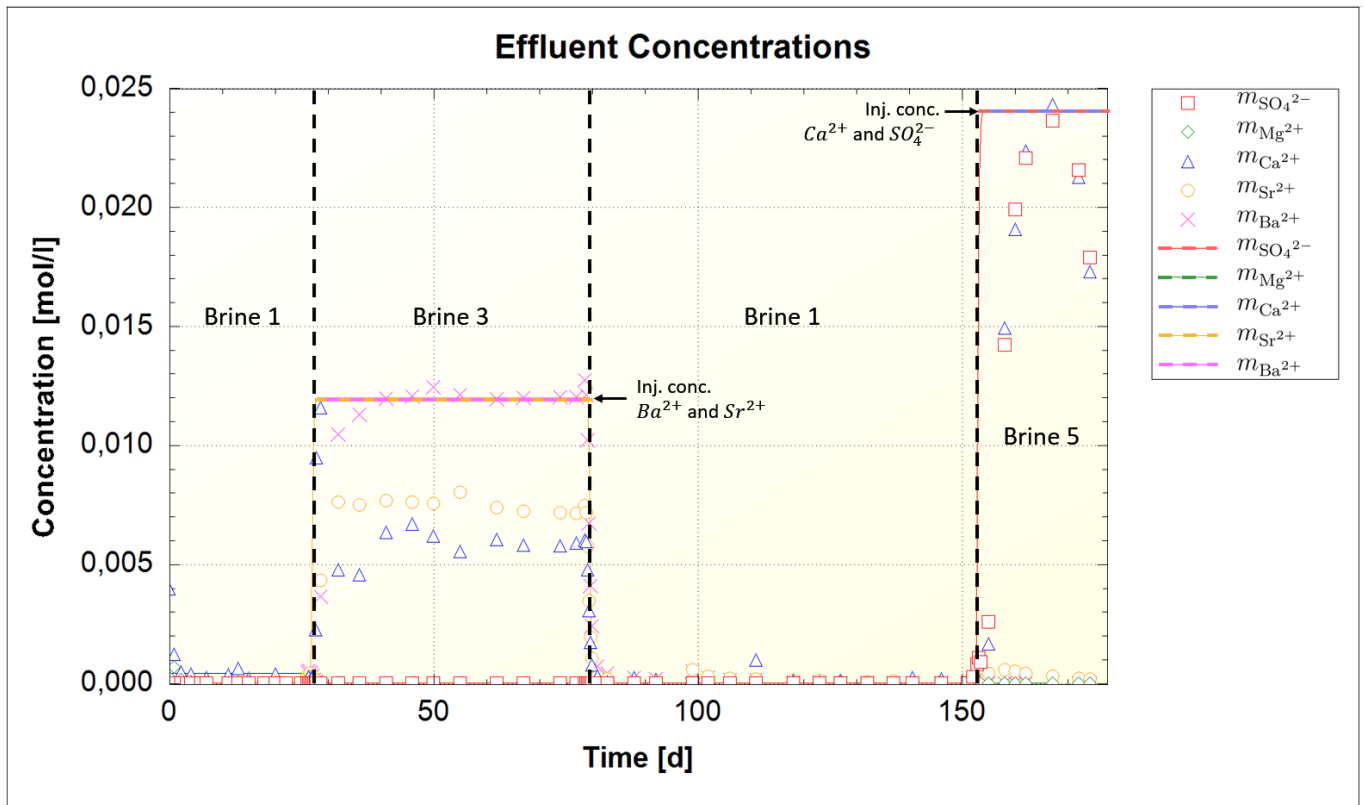


Figure 2.4: Injected and effluent concentrations of divalent ions from the M9 core (Korsnes and Madland, 2017). The data points are IC measured effluents, and the stapled lines demonstrate the injected concentration.

2.4 Core Analysis After Flooding

After the cores were flooded they were cut into slices of equal length. The slices were analyzed to quantify and confirm geochemical alterations. The slices were enumerated as illustrated in figure 2.5.

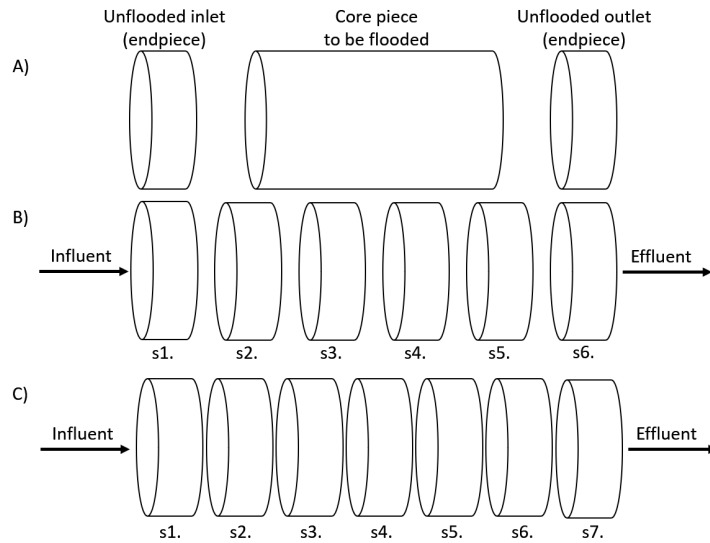


Figure 2.5: Figure inspired by Andersen et al. (2018) and Minde (2018).

A) Cylindrical samples were cut into 3 pieces, unflooded end pieces were used to measure reference properties, assumed to be representative for unflooded material, the center piece was used in flooding procedures.

B) After flooding M9 and M12 were cut into 6 slices, and enumerated as illustrated.

C) After flooding MO10 was cut into 7 slices, and enumerated as illustrated.

2.4.1 Whole-rock Geochemical Analysis

The geochemical analysis of the MO10 core was performed as a part of the work of Andersen et al. (2018), and the data presented in table 2.3 are retrieved from its supplementary material, whilst the geochemical analysis of M9 and M12 was performed to support this study.

Representative samples of each slice were milled and sent to Bureau Veritas Minerals' Acme laboratory in Vancouver, Canada, for a whole-rock geochemical analysis. The Inductively Coupled Plasma Mass Spectrometry (ICP-MS) analysis method was used. The ICP-MS analysis gives the relative amount of the elements and oxides, and an overview of their distribution in the slices in accordance with figure 2.5. The main step of the ICP-MS analysis method is given below. For further information, the reader is referred to <https://crustal.usgs.gov/laboratories/icpms/intro.html> and <http://acmelab.com/>.

The samples were milled, mixed with $\text{LiBO}_2/\text{Li}_2\text{B}_4\text{O}_7$, fused and colled before it was dissolved in American Chemical Society grade nitric acid. Hence, the samples are separated by inductively coupled plasma (ICP), and detected by the mass spectrometer (MS) (Wolf, 2005; Andersen et al., 2018; Minde, 2018).

		MgO	CaO	Ba	Sr	TOT/C	TOT/S
		[wt%]	[wt%]	[ppm]	[ppm]	[wt%]	[wt%]
MO10 MgCl ₂ -flooded	Unflooded end piece	0.27	55.08	21	871	12.27	b.d.l.
	s1.	1.31	53.56	17	981	11.92	b.d.l.
	s2.	2.26	52.87	15	965	12.14	b.d.l.
	s3.	2.51	54.01	14	934	12.59	b.d.l.
	s4.	1.64	53.42	13	940	12.33	b.d.l.
	s5.	1.08	54.55	13	914	12.34	b.d.l.
	s6.	0.84	54.43	12	890	12.18	b.d.l.
	s7.	0.79	57.92	12	915	12.04	b.d.l.

Table 2.3: Distribution of most relevant elements from ICP-MS analysis on cores from Andersen et al. (2018). Slice enumerating in accordance with figure 2.5 C), and 'Unflooded end piece' accounts for both inlet and outlet end pieces. 'TOT/C' and 'TOT/S' are abbreviations for total carbon and sulphide, respectively. 'b.d.l.' means below detection level.

		MgO	CaO	Ba	Sr	TOT/C	TOT/S
		[wt%]	[wt%]	[ppm]	[ppm]	[wt%]	[wt%]
M12	Unflooded inlet	0.26	55.24	20	843.9	12.33	<0.02
	s1.	1.78	36.81	>50000	>50000	10.95	<0.02
	s2.	0.59	54.54	440	1759	12.39	<0.02
	s3.	0.69	54.76	297	1367	12.39	<0.02
	s4.	0.76	54.82	208	952	12.42	<0.02
	s5.	0.77	54.77	205	853	12.31	<0.02
	s6.	0.78	54.65	244	897	12.33	<0.02
	Unflooded outlet	0.27	55.07	23	785	12.39	0.02
M9	Unflooded inlet	0.24	55.04	28	878.2	12.36	<0.02
	s1.	0.28	52.18	8857	34921	11.81	0.62
	s2.	0.25	55.10	242	1241	12.39	0.02
	s3.	0.24	54.98	237	1026	12.45	0.02
	s4.	0.26	55.21	234	968	12.30	<0.02
	s5.	0.25	55.15	200	915	12.36	0.02
	s6.	0.25	55.05	202	939	12.39	0.03
	Unflooded outlet	0.26	55.01	25	790	12.33	<0.02

Table 2.4: Distribution of most relevant elements from ICP-MS analysis performed on cores from Korsnes and Madland (2017). Slice enumerating in accordance with figure 2.5 B). 'TOT/C' and 'TOT/S' are abbreviations for total carbon and sulphide, respectively.

2.4.2 Electron Microscopy Analysis

The theoretical background of electron microscopy analysis method which is shortly presented here, is heavily inspired by the doctoral thesis of Mona W. Minde (2018). The reader is referred to Minde (2018) for further detail beyond what is described below.

Electron microscopy uses an electron beam, with a wavelength shorter than optical light, to image the sample, giving higher resolution. Scanning electron microscopy (SEM) enables an analysis of composition and texture down to nanometre scale (Minde, 2018).

The sample has to be conductive to ensure a steady flux of electrons, therefore the chalk samples are coated with palladium. During the electron bombarding of the sample with electrons, various energy signals are reflected and produced. Some of these energies are secondary electrons (SE), backscattered electrons (BSE), and characteristic x-rays. SE are electrons that are excited or emitted from the atom when primary electrons (the bombarding electrons) hit the mineral's surface. SE will vary as a function of topography and partially vary as a function of the composition, meaning SE images the surface. BSE are reflected primary electrons. The amount of BSE depends on the atomic number, i.e. the number of protons in the atom core. Therefore, it enables grey-scale images related to the average atomic number, which allows for visually separating different mineralogies and compositions. The characteristic x-rays are produced as inner-shell electrons are excited by primary electrons, and outer-shell electrons emit energy (x-rays) to replace the excited electrons. These x-rays are detected by an EDAX energy dispersive x-ray spectroscopy (EDS) system, which gives a compositional analysis, both qualitative and semi-quantitative.

Mona W. Minde performed a SEM analysis on parts from the inlet of the M9 and M12 cores. Results from this work were used to validate and support mineral selection, and understand mineral distribution. The SEM-image and EDS-spectrum are shown in appendix A.

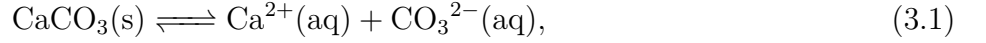
3 | Theory

The theoretical background used to evaluate the experimental data and implement the reaction kinetics are presented in this chapter. Herein the following topics are discussed: the general chemistry related to saturation of carbonates, exemplified using calcite (CaCO_3), followed by the fundamentals of transportation equations, and finally how these aspects are evaluated with PHREEQC.

3.1 Chemistry

3.1.1 Chemical Equilibrium

In an aqueous system, the mineral saturation state can be determined by considering the ratio law of mass action (LMA) and its solubility product. Considering the equilibrium of solid calcite (CaCO_3) in water:



where (*s*) and (*aq*) indicate that the specie is in solid or aqueous phase, respectively. From the LMA of calcite the ion activity product (IAP) is defined as:

$$IAP_{cal} = \frac{a_{\text{Ca}^{2+}(aq)} \cdot a_{\text{CO}_3^{2-}(aq)}}{a_{\text{CaCO}_3(s)}} = a_{\text{Ca}^{2+}(aq)} \cdot a_{\text{CO}_3^{2-}(aq)}, \quad (3.2)$$

where subscript *cal* denotes calcite, and a_i denotes the activity of specie *i*. The activity of a specie can be considered as a measure of its effective concentration, or as an indication of how the specie would behave in a diluted solution. The activity of solids are defined as 1 (Morse and Mackenzie, 1990; Appelo and Postma, 2005), whilst the activity of aqueous species can be determined by several different methods depending on the ionic strength of the solution, such as Truesdell-Jones equation:

$$\log \gamma_i = -\frac{A' Z_i^2 \sqrt{I}}{1 + B a'_i \sqrt{I}} + b_i I, \quad (3.3)$$

where γ denote the activity coefficient, A' and B are temperature dependent coefficient, Z_i is the valence number of ion *i*, a'_i and b_i are parameters specifically fitted to ion *i* (Morse and Mackenzie, 1990; Appelo and Postma, 2005), and I is the ionic strength. Thus, the activity of a component is the product of its concentration (m_i) expressed as molarity (*mol/litre*), and its activity coefficient (γ_i). The ionic strength describes the number of electrical charges in a solution, and it emphasizes on the charge of the ions (Morse and Mackenzie, 1990; Atkins and de Paula, 2002):

$$I = \frac{1}{2} \sum_i (m_i \cdot Z_i^2). \quad (3.4)$$

To determine the saturation state of calcite, the ratio of ion activity product, IAP_{cal} , and its equilibrium constants, K_{cal} , known as the saturation ratio (Ω) are evaluated:

$$\Omega_{cal} = \frac{IAP_{cal}}{K_{cal}}. \quad (3.5)$$

Another way of expressing the saturation state is the saturation index, SI :

$$SI_{cal} = \log \Omega_{cal} = \log \left(\frac{IAP_{cal}}{K_{cal}} \right). \quad (3.6)$$

Ω or SI are often used to define reaction rates, e.g. precipitation or dissolution reactions have a higher reaction rate towards equilibrium depending on the difference in Ω or SI relative to the equilibrium value. The saturation state of a components in under-saturated, saturated, and super-saturated is defined as $\Omega < 1$, $\Omega = 1$, and $\Omega > 1$, respectively. Using equation (3.6), the SI is less than, equal to, and greater than zero, in an under-saturated, saturated, and super-saturated system, respectively.

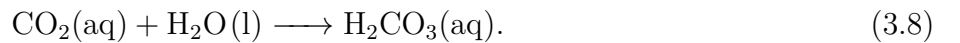
When calcite mineral reaches dynamic equilibrium with a solution, the addition or removal of the ions will cause precipitation or more dissolution of calcite, respectively. This is referred to as Le Châtelier's principle, which states: *"If a system at equilibrium is disturbed by a change in concentration, pressure, or temperature, the system will, if possible, shift to partially counteract the change .."* (Masterton and Hurley, 2004, p.334). Note that the addition of more solid material, more calcite in this example, to a system in equilibrium, will not cause more dissolution or precipitation, because solid calcite activity is assumed to be 1 and independent of concentration, as discussed above.

3.1.2 The Carbonic Acid System

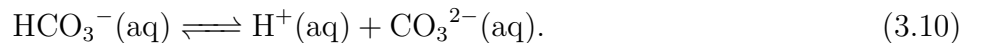
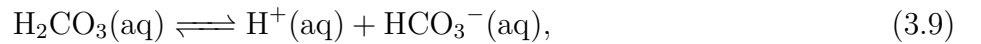
The carbonic acid system is an important aspect of the geochemistry of carbonates (Morse and Mackenzie, 1990). Considering a simplified system with de-ionized water in contact with atmospheric CO_2 , gaseous $\text{CO}_2(\text{g})$ will dissolve into an aqueous phase and affect the pH, by forming carbonic acid:



and subsequently form carbonic acid:



The carbonic acid has two protons to dissociate stepwise, forming bicarbonate (HCO_3^-) and carbonate (CO_3^{2-}):



The dissolved carbonate concentration is pH dependent, and by relating it to self-protonation of water, a set of equilibrium equations can be used to describe the carbonic acid system:

$$K_w = [\text{H}^+][\text{OH}^-], \quad (3.11)$$

$$K_H = \frac{[\text{CO}_2(\text{aq})]}{P_{\text{CO}_2}}, \quad (3.12)$$

$$K_0 = \frac{[\text{H}_2\text{CO}_3(\text{aq})]}{[\text{CO}_2(\text{aq})]}, \quad (3.13)$$

$$K_1 = \frac{[\text{HCO}_3^-(\text{aq})][\text{H}^+(\text{aq})]}{[\text{H}_2\text{CO}_3(\text{aq})]}, \quad (3.14)$$

$$K_2 = \frac{[\text{CO}_3^{2-}(\text{aq})][\text{H}^+(\text{aq})]}{[\text{HCO}_3^-(\text{aq})]}, \quad (3.15)$$

where P_{CO_2} is the activity of gaseous CO_2 , defined as the partial pressure of CO_2 in the gas phase, and the K 's denote the equilibrium constants. In air $P_{\text{CO}_2} = 10^{-3.5}$ atmospheric pressure (Martínez and Uribe, 1995; Appelo and Postma, 2005; Andersen et al., 2018) at ambient temperature. The P_{CO_2} is later used to carbonate the injection brines, consequently including the carbonic acid system to the brines before simulated to be injected in the cores.

Figure 3.1 demonstrates the using equations (3.11) - (3.15) to compute the relative carbonate distribution as a function of pH, in an idealized system at ambient temperature.

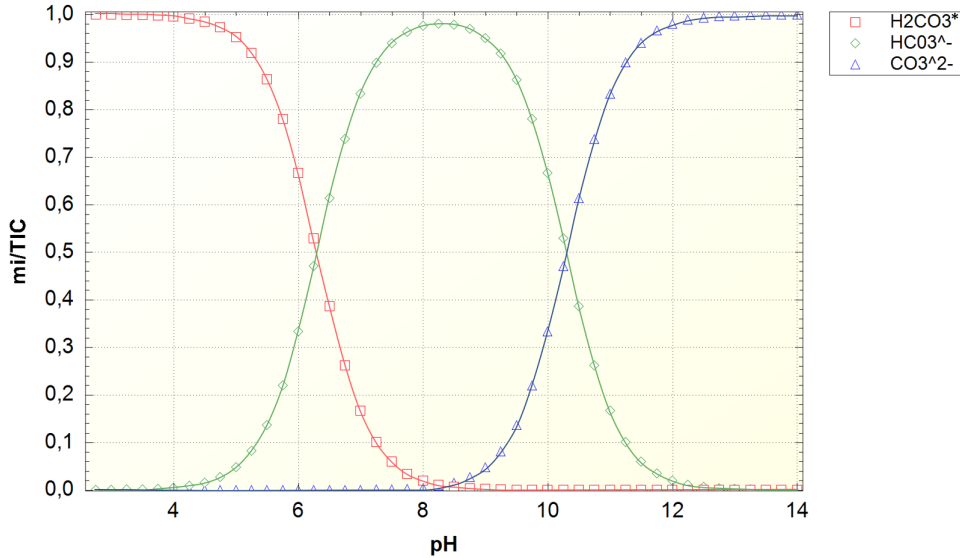


Figure 3.1: The carbonate phase plotted against pH in a simplified system, at ambient temperature.

Where TIC denotes total inorganic carbon, and it is quantified by the sum of H_2CO_3^* , HCO_3^- , and CO_3^{2-} . Illustrated in figure 3.1, the concentration of CO_3^{2-} increases with pH, thus at lower pH carbonate minerals are more soluble (Erdemoğlu and Canbazoglu, 1998; Appelo and Postma, 2005). Note that at standard conditions (sc), $\text{CO}_2(\text{aq})$ is 600 times more abundant than H_2CO_3 (Appelo and Postma, 2005)[p.179], but to illustrate the distribution of carbonate in figure 3.1, H_2CO_3^* does by convention account for both $\text{H}_2\text{CO}_3(\text{aq})$ and $\text{CO}_2(\text{aq})$.

3.1.3 Charge Balance

The charge balance in an aqueous system determined by:

$$\Delta_{charge} = \sum_i Z_i \cdot m_i, \quad (3.16)$$

where Δ_{charge} is the charge difference or imbalance in the solution, which should be close to zero, Z_i and m_i are the valence and concentration of component i , respectively. The sign of the valence is used in the charge balance equation. To exemplify this, consider de-ionized water in equilibrium with atmospheric CO_2 , where the charge balance becomes:

$$\begin{aligned} \Delta_{charge} &= (+1) \cdot m_{\text{H}^+} + (-1) \cdot m_{\text{OH}^-} + (-2) \cdot m_{\text{CO}_3^{2-}} + (+1) \cdot m_{\text{HCO}_3^-} + (0) \cdot m_{\text{H}_2\text{CO}_3^0} \\ &= m_{\text{H}^+} - m_{\text{OH}^-} - 2 \cdot m_{\text{CO}_3^{2-}} + m_{\text{HCO}_3^-}, \end{aligned}$$

By rewriting the charge balance in terms of known concentrations and equilibrium constants, using equations (3.11) - (3.15), the charge balances can be used to determine m_{H^+} , i.e. the pH, by using an iterative method, such as the Newton-Raphson method. For further details of this procedure, the reader is referred to the literature, e.g. Volcke et al. (2005).

3.1.4 Mineral Dissolution and Precipitation

As a mineral dissolve or precipitate, the concentration of its constituents changes in the solution. These changes are expressed by the general rate equation proposed by Lasaga (1998):

$$\dot{r} = \pm k SA |1 - \Omega^p|^q, \quad (3.17)$$

where \dot{r} denote dissolution or precipitation for a mineral, for $\dot{r} < 0$ and $\dot{r} > 0$, respectively, k is the rate constant, SA is the reactive surface area, Ω the saturation ratio, and p and q are empiric exponent parameters.

To determine the reaction rate the transition state theory (TST) can be used, as it provides a less complicated way to determine reaction rate coefficients. The foundation of the TST is that there exists an active-complex-state between chemical reactants and products. This intermediate state is characterized by the activation energy, which is the highest energy along with the transition from reactants to products (Laidler and King, 1983; Mavroudakos et al., 2019). For further details on TST the reader is referred to the literature, e.g. Laidler and King (1983) and Mavroudakos et al. (2019).

The Arrhenius equation interprets the temperature effect on the reaction rates:

$$k(T) = A e^{-\frac{E_a}{RT}}, \quad (3.18)$$

where $k(T)$ is the rate constant at a specified temperature, A is the Arrhenius pre-exponential factor, E_a is the apparent activation energy, R is the gas constant, and T is the absolute temperature. Both the pre-exponential factor and the activation energy are treated as temperature independent (Laidler,

1984). For reactions where the reaction rate k_1 is known at a given temperature T_1 , the reaction rate at T_2 can be determined using the integrated van't Hoff equation:

$$k_{T_2} = k_{T_1} e^{\frac{-E_a}{R} \left(\frac{1}{T_2} - \frac{1}{T_1} \right)}. \quad (3.19)$$

The pH dependency is accounted for by either using one rate constant over a distinct pH range, based on linear regression or using two or more rate constants which account for additional mechanisms that either inhibit or catalyze the reaction rate. The rate constant k in equation (3.17) is determined at a temperature T , and taking catalysts and inhibitors into account using:

$$k = k_{T=25^\circ C} e^{-\frac{E_a}{R} \left(\frac{1}{T} - \frac{1}{298.15} \right)} + \sum_i k_{T=25^\circ C}^i e^{-\frac{E_a^i}{R} \left(\frac{1}{T} - \frac{1}{298.15} \right)} \prod_j a_{i,j}^{n_{i,j}}, \quad (3.20)$$

where $k_{T=25^\circ C}$ is the intrinsic kinetic constant at 25°C, subscript i refers to additional mechanisms, and $a_{i,j}$ is the activity of component j which inhibit or catalyze the mechanism to the power n .

Mineral precipitation regimes depend on saturation. Appelo and Postma (2005) illustrated the different regimes schematically by considering a mineral AB consisting of the ionic components A and B :

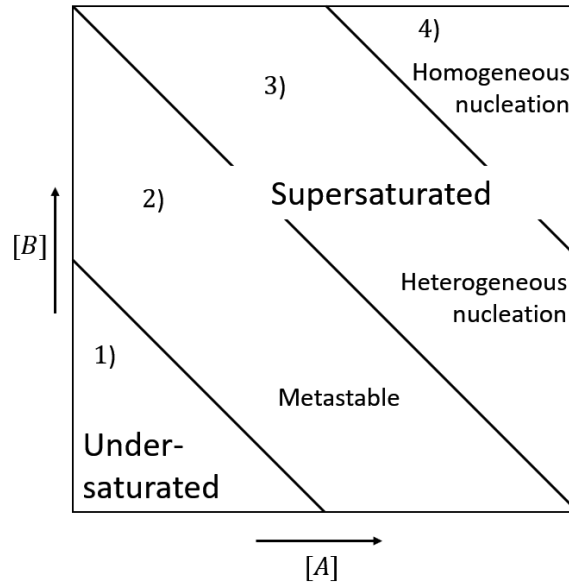


Figure 3.2: Regimes of crystal growth of mineral AB , where $[A]$ and $[B]$ are the activity of the constituents. In region 1) $SI < 0$, while $SI > 0$ in regions 2) - 4). Figure inspired by Appelo and Postma (2005)[p.168].

In region 1) the mineral is under-saturated, and mineral dissolution is likely to occur. The line separating region 1) and 2) represent the solubility product. In region 2) the mineral is supersaturated, existing minerals may grow, but no nucleation will occur. In region 3) nucleation of mineral AB may occur on other mineral surfaces or impurities, and further mineral growth, known as heterogeneous nucleation. In region 4) the brine is sufficiently high for homogeneous nucleation, where many small secondary minerals are formed spontaneously in the liquid phase (Oxtoby, 1992; Lasaga, 1998; Palandri and Kharaka, 2004; Appelo and Postma, 2005).

3.2 Transport Equations

3.2.1 Advection

Advection is referred to as flow or transfer of fluid. It is one of the primary mechanisms contributing to transport solutes and components, and the driving force is referred to as the gradient of the hydraulic head, i.e. pressure difference and buoyancy effects (Appelo and Postma, 2005; Sævik, 2011; Rumynin, 2012).

3.2.2 Diffusion

The main principle of diffusion can be considered as random motion of a component in a system with no bulk transport, due to uneven concentrations. It is defined as a process where components, e.g. molecules, ions, or particles, move from regions with higher concentration to regions with a lower concentration, towards a more evenly component distribution. Fick's 1st law relates flux proportionally to the component concentration gradient:

$$J_i \propto \frac{\partial c_i}{\partial x}, \quad (3.21)$$

where J is the flux and $\frac{\partial c_i}{\partial x}$ is the concentration gradient of component i as a change in position. By introducing a proportional coefficient to equation (3.21):

$$J_i = -D_m \frac{\partial c_i}{\partial x}, \quad (3.22)$$

where D_m is the proportional coefficient, i.e. the diffusion coefficient.

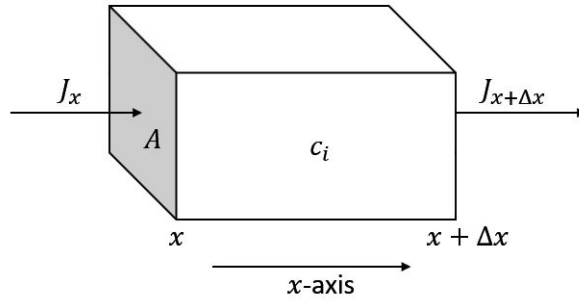


Figure 3.3: Linearised 1D reservoir.

Assuming that there is a concentration gradient along x , causing flux J_x and $J_{x+\Delta x}$. Change in concentration over time, i.e. change in mols over time, is expressed by:

$$(c_{i,t+\Delta t} - c_{i,t}) \cdot A \cdot \Delta x = J_x \cdot A \cdot \Delta t - J_{x+\Delta x} \cdot A \cdot \Delta t, \quad (3.23)$$

where

$$\begin{aligned}
J_x &= -D_m \frac{\partial c_i}{\partial x}, \\
J_{x+\Delta x} &= J_x + \frac{\partial J}{\partial x} \Delta x \\
&= -D_m \frac{\partial c_i}{\partial x} - D_m \frac{\partial^2 c_i}{\partial x^2} \Delta x.
\end{aligned}$$

By substitution J_x and $J_{x+\Delta x}$ into equation (3.23), and reducing the equation with a factor of $A \cdot \Delta x \cdot \Delta t$, this results in:

$$\frac{(c_{i,t+\Delta t} - c_{i,t})}{\Delta t} = D_m \frac{\partial^2 c_i}{\partial x^2}. \quad (3.24)$$

Let $\Delta t \rightarrow 0$ and $\Delta x \rightarrow 0$, and eq. (3.24) becomes Fick's 2nd law:

$$\frac{\partial c_i}{\partial t} = D_m \frac{\partial^2 c_i}{\partial x^2}. \quad (3.25)$$

The solution of equation (3.25) describes how the concentration of components i spreads by diffusion.

The diffusion coefficient D_m assumes that components can move without restrictions, i.e. straight line. In porous media, the components must *navigate* through the pore volume, consequently an effective diffusion coefficient D_e is introduced:

$$D_e = \frac{D_m}{\theta^2}, \quad (3.26)$$

where θ is known as tortuosity and takes account for the pore geometry. Note that $\theta \geq 1$, therefore the diffusion coefficient in porous media is lower than in a cup of water.

3.2.3 Dispersion

Dispersion is the random distribution of components during advection flow. The effect of dispersion is enhanced by advection, since flow distributes the component concentration according to pore size distribution. It is expressed by the hydrodynamic dispersion coefficient D_L . The subscript L indicates longitudinal dispersion, and is the type considered in 1-dimensional (1D) modeling.

During advection, e.g. core flood experiments, Fick's laws are expressed using D_L , where D_L is the hydrodynamic dispersion coefficient, which accounts for diffusion and advective contribution:

$$D_L = D^{diffusion} + D^{advection}. \quad (3.27)$$

The advection contribution often dominates the hydrodynamic dispersion coefficient (Appelo and Postma, 2005; Rumynin, 2012), where the advective contribution is estimated by:

$$D^{advection} = \alpha_L \cdot v, \quad (3.28)$$

where α_L is the dispersivity and v is the pore water flow velocity.

3.2.4 Initial State

The initial rock matrix composition of the chalk cores are assumed to be of pure calcite (see discussion in chapter 2). Consequently, the initial mineral concentration is defined as:

$$m_{cal}(x, t = 0) = m_{cal}^0, \quad (3.29)$$

$$m_j = 0, \quad (3.30)$$

where j denote the minerals considered: anhydrite (CaSO_4), calcite (CaCO_3), celestite (SrSO_4), magnesite (MgCO_3), strontianite (SrCO_3), and witherite (BaCO_3). Further, is the initial brine composition within the cores, defined in chapter 2, equal to:

$$m_i(x, t = 0) = m_i^0, \quad (3.31)$$

where i denote the components Cl^- , Na^+ , SO_4^{2-} , Mg^{2+} , Ca^{2+} , Sr^{2+} , Ba^{2+} .

3.2.5 Boundary Conditions

It is assumed that the brine composition at the inlet is constant for each flooding sequence. That is:

$$m_i(\text{inlet}, t_k \leq t < t_{k+1}) = m_i^{\text{inj}}, \quad (3.32)$$

where i denote the injected components Cl^- , Na^+ , SO_4^{2-} , Mg^{2+} , Ca^{2+} , Sr^{2+} , Ba^{2+} , and k is the sequence number. The outlet boundary is considered an extension of the core, i.e. a flux boundary.

3.2.6 Advection-Dispersion-Reaction Equation

The general dissolution-precipitation reaction rate given in equation (3.17) is further developed by Palandri and Kharaka (2004) and Appelo and Parkhurst (2013). In equation (3.33) a reduction factor, $RF_i < 1$, introduced by Andersen et al. (2018), accounts for the less available surface area for mineral j :

$$\dot{r}_j = -RF_j \left(\frac{A_0}{V} \right) k_j \text{sign}(SI_j) |1 - \Omega_j^{p_j}|^{q_j}, \quad (3.33)$$

where j denotes the minerals considered: anhydrite (CaSO_4), calcite (CaCO_3), celestite (SrSO_4), magnesite (MgCO_3), strontianite (SrCO_3), and witherite (BaCO_3). Moreover, RF is the reduction factor, which accounts for the less available area Andersen et al. (2018), where $\left(\frac{A_0}{V} \right)$ is the initial surface area adjusted to the volume of the solution, k_i is the rate constant as defined in equation (3.20), and p and q is parameters specified for mineral and/or temperature retrieved from literature, p is often related to the mineral growth mechanism and can be predicted from transition state theory (Palandri and Kharaka, 2004; Bose et al., 2008; Saldi et al., 2009).

The system is described by the following partial differential advection-dispersion-reaction equations:

$$\partial_t m_{\text{Cl}^-} = -\partial_x (v m_{\text{Cl}^-}) + \partial_x (D_L \partial_x m_{\text{Cl}^-}), \quad (3.34)$$

$$\partial_t m_{\text{Na}^+} = -\partial_x (v m_{\text{Na}^+}) + \partial_x (D_L \partial_x m_{\text{Na}^+}), \quad (3.35)$$

$$\partial_t m_{\text{SO}_4^{2-}} = -\partial_x (v m_{\text{SO}_4^{2-}}) + \partial_x (D_L \partial_x m_{\text{SO}_4^{2-}}) + \dot{r}_{\text{SO}_4^{2-}}, \quad (3.36)$$

$$\partial_t m_{\text{Mg}^{2+}} = -\partial_x (v m_{\text{Mg}^{2+}}) + \partial_x (D_L \partial_x m_{\text{Mg}^{2+}}) + \dot{r}_{\text{Mg}^{2+}}, \quad (3.37)$$

$$\partial_t m_{\text{Ca}^{2+}} = -\partial_x (v m_{\text{Ca}^{2+}}) + \partial_x (D_L \partial_x m_{\text{Ca}^{2+}}) + \dot{r}_{\text{Ca}^{2+}}, \quad (3.38)$$

$$\partial_t m_{\text{Sr}^{2+}} = -\partial_x (v m_{\text{Sr}^{2+}}) + \partial_x (D_L \partial_x m_{\text{Sr}^{2+}}) + \dot{r}_{\text{Sr}^{2+}}, \quad (3.39)$$

$$\partial_t m_{\text{Ba}^{2+}} = -\partial_x (v m_{\text{Ba}^{2+}}) + \partial_x (D_L \partial_x m_{\text{Ba}^{2+}}) + \dot{r}_{\text{Ba}^{2+}}, \quad (3.40)$$

where v is the solute/brine flow velocity, D_L is the hydrodynamic dispersion coefficient, and \dot{r} denote the source terms. Further, the source terms for each component is the sum of the reaction rate equations for the minerals composed of the component. Due to stoichiometry, the source terms are defined:

$$\dot{r}_{\text{SO}_4^{2-}} = -\dot{r}_{anh} - \dot{r}_{cel}, \quad (3.41)$$

$$\dot{r}_{\text{Mg}^{2+}} = -\dot{r}_{mag}, \quad (3.42)$$

$$\dot{r}_{\text{Ca}^{2+}} = -\dot{r}_{anh} - \dot{r}_{cal}, \quad (3.43)$$

$$\dot{r}_{\text{Sr}^{2+}} = -\dot{r}_{cel} - \dot{r}_{str}, \quad (3.44)$$

$$\dot{r}_{\text{Ba}^{2+}} = -\dot{r}_{wit}, \quad (3.45)$$

where subscripts *anh*, *cal*, *cel*, *mag*, *str*, and *wit*, denote anhydrite, calcite, celestite, magnesite, strontianite, and witherite, respectively.

As a dynamic equilibrium, referred to as steady-state, is achieved, meaning that at any point in the system $\partial_t m_i = 0$, equations (3.34) - (3.40) defining the system are rewritten:

$$\partial_x (v m_{\text{Cl}^-}) = 0, \quad (3.46)$$

$$\partial_x (v m_{\text{Na}^+}) = 0, \quad (3.47)$$

$$\partial_x (v m_{\text{SO}_4^{2-}}) = \dot{r}_{\text{SO}_4^{2-}}, \quad (3.48)$$

$$\partial_x (v m_{\text{Mg}^{2+}}) = \dot{r}_{\text{Mg}^{2+}}, \quad (3.49)$$

$$\partial_x (v m_{\text{Ca}^{2+}}) = \dot{r}_{\text{Ca}^{2+}}, \quad (3.50)$$

$$\partial_x (v m_{\text{Sr}^{2+}}) = \dot{r}_{\text{Sr}^{2+}}, \quad (3.51)$$

$$\partial_x (v m_{\text{Ba}^{2+}}) = \dot{r}_{\text{Ba}^{2+}}. \quad (3.52)$$

3.3 PHREEQC

The theory for the PHREEQC software is retrieved from Appelo and Parkhurst (2013), Appelo and Postma (2005), and Parkhurst and Appelo (1999).

The PHREEQC version 3 program is capable of simulating several equilibrium reactions, such as dissolution-precipitation reactions, ion exchange, and surface complexes. It is based on equilibrium chemistry between aqueous, gaseous and solid phases, exchangers, and sorption surfaces (Appelo and Parkhurst, 2013, p.25). The database used for the simulations is the Lawrence Livermore National Laboratory (LLNL) database. It is one of the available databases in the PHREEQC package, and it is the most complete and internally consistent database available, providing data to perform calculations of more complexes (Appelo and Postma, 2005; Appelo and Parkhurst, 2013; Hiorth et al., 2013).

For the model used in this work, the ion compositions of the brines are specified, and the pH is set to be adjusted to correct the charge balance. This means that the concentration of H^+ is adjusted to reduce the charge balance, Δ_{charge} in equation (3.16).

The Newton-Raphson method is used to compute the equilibrium in PHREEQC. All mass-action equations are derived to mol and charge balance equations. These equations are addressed to a series of functions, which describe the system. By adjusting the master unknowns, the Newton-Raphson method is used to compute the system describing function equal to zero. The master unknowns form the Jacobian matrix, which forms a set of linear equations.

3.3.1 Transport Calculations

In reactive transport simulations in PHREEQC, advective, diffusive and reactive calculations are performed. For each time step advection, diffusion and reactive calculations are performed, in that order (Appelo and Parkhurst, 2013). The numerical Newton-Raphson method is used to solve the set of non-linear advection-dispersion-reaction equations.

To capture concentration changes, the rates must be integrated over time. PHREEQC solves systems of stiff sets of equations, i.e. a set of equations where implicit methods perform better than explicit methods (Heiter and Lebedz, 2012), using a Runge-Kutta method. An error estimate is calculated by a lower order Runge-Kutta method and compared with the user-defined tolerance.

Transport simulations in PHREEQC include three types of boundary conditions: closed, constant, and flux. Herein, *constant* and *flux* boundary conditions are used at the inlet and outlet, respectively. *Constant* means that there is only advective transportation of the components across the boundary, and *flux* means that both advection and dispersion control the transport of the components.

4 | Methodology

In this chapter a general description of the methodology used to develop the 1D ADR model is presented.

4.1 Static Model

- Define brine compositions used in experiments (listed in table 2.1).
- Equilibrate brines with atmospheric CO_2 .
- Mix sequenced brines in accordance with flooding procedure stated in chapter 2.
- Equilibrate brines and mixtures of sequenced brines with solid calcite (CaCO_3), individually, at 130°C and 7 atm.
- Analyze saturation states for each mineral using literature, experimental data from Andersen et al. (2018), Korsnes and Madland (2017), and SEM-analysis, to determine what minerals that are likely to explain the effluent concentrations and mineral distribution from geochemical analysis.

4.2 Dynamic Model

- Define initial system.
- Use results from static model to define composition of the injected brines - need to use static model to include the carbon content in each brine.
- Tune dispersion coefficient to match effluent concentration of a tracer, using Cl^- as tracer.
- Implement reaction kinetic parameters from literature for each mineral.
- Adjust the tuning parameters RF_i and S_i and to match steady-state effluent concentrations and element distribution from geochemical analysis.

5 | Modeling Methodology

5.1 Static Model

To determine which minerals to include in the dynamic model, a static model was developed. The static model is made in PHREEQC version 3.4. The 11 different brines used in flooding experiments in Andersen et al. (2018) and Korsnes and Madland (2017), listed in table 2.1, were defined.

Discussed in section 3.1.2, the solubility of calcite is affected by the brine pH, which is affected by atmospheric CO₂. Consequently, the first equilibrium the pre-defined aqueous phase meets is with atmospheric CO₂. The partial pressure of CO₂ is approximately 10^{-3.5} atmospheric pressure (atm) (Martínez and Uribe, 1995; Appelo and Postma, 2005; Andersen et al., 2018). This first equilibrium occurs at standard conditions (sc), i.e. at 25°C and atmospheric pressure (1 atm).

The next step is to mix the brines, both individually and as a mix of sequenced brines, with solid calcite (CaCO₃). Since the experiments were performed at (Ekofisk) reservoir conditions, this step is performed at 130°C. The pressure need to be sufficiently high to prevent the water from boiling out at elevated temperatures. Consequently, reaction pressure was set to 7 atm, i.e. equal the pore pressure used in the experimental work.

As calcite is dissolved into the brine, the ion composition changes, resulting in changes of some mineral saturation. As discussed in section 3.3, the LLNL-database is used, thus many minerals are evaluated by PHREEQC (Appelo and Parkhurst, 2013). The model outputs are atmospheric CO₂ equilibrated brine compositions and a list of mineral saturation indexes (*SI*) for each brine and mixes of sequenced brines, tabulated in table 6.1.

5.2 Dynamic Model

When a brine with reactive components is transported through a porous carbonate media, several factors are affecting how the components propagate. The component propagation is controlled by mechanisms such as advective and dispersive transportation, retarded or accelerated by reactions such as precipitation or dissolution, adsorption or desorption.

5.2.1 Defining the Initial System

The amount of minerals, brine ions, and surface ions are given in mol per litre pore volume, denoted by concentrations C_i (Andersen et al., 2018). Andersen et al. (2018) flooded five different outcrop chalk types, with various purity. Discussed in chapter 2, the Mons chalk is a clean calcium carbonate chalk. Consequently, the conversion from initial calcite mass to initial calcite concentrations are

computed using:

$$C_{calcite} = \frac{\rho_{calcite}}{MW_{calcite}} \frac{(1 - \phi)}{\phi}, \quad (5.1)$$

where MW_i is mineral molar weight, ρ_{cal} is calcite density, and ϕ is the initial porosity of the sample. The reader is referred to Andersen et al. (2018) for further details on the general conversion equation. Further, the $\left(\frac{A_0}{V}\right)$ is calculated for each core using the specific surface area (SSA) from Megawati et al. (2015), the core porosity and calcite density in equation:

$$\left(\frac{A_0}{V}\right) = SSA \cdot \frac{V_{matrix}}{1 \text{ litre PV}} \cdot \rho_{cal} = SSA \cdot \frac{1 \text{ litre}}{\phi} \cdot \rho_{cal}, \quad (5.2)$$

where $SSA = 1.81 \text{ m}^2/\text{g}$ (Megawati et al., 2015). The initial reactive surface area per litre pore volume for each core are summarized in table 5.1 Using parameters listed in tables 2.2 and 5.3, the initial concentration of calcite for each core was calculated, and values are presented in table 5.1.

Core	Initial C_i [mol/kg water]	$\left(\frac{A_0}{V}\right)$
MO10	38.2	11765
M9	36.6	11480
M12	36.4	11455

Table 5.1: Initial calcite concentration and reactive surface area per litre pore volume for each core, calculated using equation (5.1) and (5.2).

The MO10 core was initially saturated with DW, whilst M9 and M12 were saturated with brine 1, i.e. a NaCl brine. The flooding experiments were conducted at 130°C, with pore pressure of 0.7 MPa on Mons Belgium chalk cores. Hence, the reaction temperature and pressure were set to 130°C and 0.7 MPa, and the initial brine compositions were DW for MO10, and brine 1 equilibrated with calcite for M9 and M12.

5.2.2 Minerals Included in Model

Based on experimental findings, literature and static simulations, as discussed in section 6.1, the 6 minerals listed below are included in the 1D transport model:

Mineral	Dissolution reaction		
Anhydrite	$\text{CaSO}_4(\text{s})$	\rightleftharpoons	$\text{Ca}^{2+}(\text{aq}) + \text{SO}_4^{2-}(\text{aq})$
Calcite	$\text{CaCO}_3(\text{s})$	\rightleftharpoons	$\text{Ca}^{2+}(\text{aq}) + \text{CO}_3^{2-}(\text{aq})$
Celestite	$\text{SrSO}_4(\text{s})$	\rightleftharpoons	$\text{Sr}^{2+}(\text{aq}) + \text{SO}_4^{2-}(\text{aq})$
Magnesite	$\text{MgCO}_3(\text{s})$	\rightleftharpoons	$\text{Mg}^{2+}(\text{aq}) + \text{CO}_3^{2-}(\text{aq})$
Strontianite	$\text{SrCO}_3(\text{s})$	\rightleftharpoons	$\text{Sr}^{2+}(\text{aq}) + \text{CO}_3^{2-}(\text{aq})$
Witherite	$\text{BaCO}_3(\text{s})$	\rightleftharpoons	$\text{Ba}^{2+}(\text{aq}) + \text{CO}_3^{2-}(\text{aq})$

Table 5.2: Dissolution reaction of included minerals.

Mineral i	$\log K_{eq,i}$ at 130°C	ρ_i [g/cm ³]	MW_i [g/mol]
Anhydrite	-5.86 [d]	2.98 ^[a]	135.15 ^[c]
Calcite	0.39 [d]	2.71 ^[a,b]	100.09 ^[a,b]
Celestite	-6.69 ^[d]	3.96-3.98 ^[a]	183.68 ^[c]
Magnesite	0.04 [d]	2.96 ^[b] , 2.98-3.02 ^[a]	84.32 ^[a,b]
Strontianite	-0.93 [d]	3.70 ^[b] , 3.74-3.78 ^[a]	147.63 ^[a,b]
Witherite	-2.59 [d]	4.29 ^[a] , 4.43 ^[b]	197.35 ^[a,b]

[a] retrived from Mindat.org (2019)

[b] retrived from table 2.1 in Morse and Mackenzie (1990)

[c] retrived from Kim et al. (2019)

[d] calculated with PHREEQC

Table 5.3: Properties of the minerals used in dynamic model. K_{eq} is the equilibrium constant, ρ the mineral density, MW the molecular weight.

5.2.3 Dispersion

The dispersion coefficient has to be valid for all flooding sequences. Therefore, the effluent concentration of a tracer specie has to be evaluated when the injection brine is changed. The Cl^- ion serves as a tracer (Evje et al., 2009; Madland et al., 2011), since influent and effluent concentrations are equal, i.e. no Cl^- retained. This is supported by the results from effluent measurements, and as stated by Korsnes and Madland (2017): "*Sodium and chloride concentrations are not presented in the results section, but the trend for all injections is that these two ions come out close to its original concentration for all brines used in this study*".

The M12 chalk is chosen to determine the total dispersion. To define this, the dispersivity, i.e. α in equation (3.28), is defined to zero. The M12 core was flooded with 8 different brines, giving 7 sequential Cl^- injected (see table 2.1). To evaluate the transitions of Cl^- concentrations, the concentration is normalized:

$$\bar{c} = \frac{c - c_0}{c_{inj} - c_0}, \quad (5.3)$$

where \bar{c} is the normalized and dimensionless concentration, c is the measured effluent, c_0 is the previous concentration, and c_{inj} is the injected concentration.

5.2.4 Kinetic Reaction Rates

The kinetic rate equations for the chosen minerals are based on the general dissolution-precipitation rate equation (3.33). The kinetic parameters, i.e. the specific rate constants, k , and their potential dependency on catalysts and inhibitors, expressed by the activity of the catalyst or inhibitor, are retrieved from the literature.

$$k_T = k_{T=25^\circ\text{C}} e^{-\frac{E_a}{R} \left(\frac{1}{T} - \frac{1}{298.15} \right)} + \sum_i k_{T=25^\circ\text{C}}^i e^{-\frac{E_a^i}{R} \left(\frac{1}{T} - \frac{1}{298.15} \right)} \prod_j a_{i,j}^{n_{i,j}}, \quad (3.20)$$

The kinetic rate parameters of the chosen minerals are variously investigated, resulting in variations of dissolution-precipitation kinetic rate equations for the different minerals, as shown below.

Carbonates

The pH-stat method is used to study and define the dissolution-precipitation kinetics of calcite, magnesite, and witherite (Plummer et al., 1978; Busenberg and Plummer, 1986; Chou et al., 1989). Three regions with independent and simultaneous reactions depending on different activities and rate kinetic constants were identified when considering far from equilibrium dissolution. In the following Me^{2+} denotes Ba^{2+} , Ca^{2+} , Mg^{2+} , and Sr^{2+} :

1. In the low pH region, the rate depends on the activity of H^+ , i.e. a_{H^+} , in accordance with:

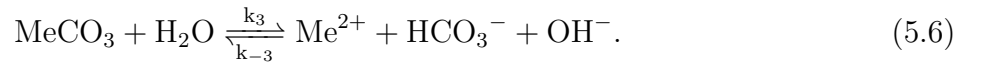


2. In the moderate pH-range, the rate depends linearly on the bulk concentration of CO_2 , related to:



where H_2CO_3^* denotes H_2CO_3 and $\text{CO}_2(\text{aq})$, as discussed in subsection 3.1.2.

3. In the alkaline pH region, the rate constant does not depend on the activity of components in the aqueous phase, related to the hydrolysis reaction:



Chou et al. (1989) emphasized that the reduction in dissolution rate at high pH demonstrates that precipitation plays a significant role when pH is greater than 8. Therefore, near equilibrium reaction mechanisms were studied, and precipitation kinetic parameters were quantified at alkaline conditions by Plummer et al. (1978), Busenberg and Plummer (1986), and Chou et al. (1989). It was concluded that precipitation is dominated by the backward reaction of reaction equation (5.6), see Plummer et al. (1978) and Chou et al. (1989) for discussion.

Even though the dissolution and precipitation reaction kinetics were studied this thoroughly in the late '70s and '80s, the available reaction kinetic data for these carbonates are either not defined, sparsely shared, or too difficult to define. Hence, the reaction kinetic parameters used herein are of various quality. Furthermore, very few precipitation rate constants are determined, due to the challenge of controlling what minerals that precipitate during an experiment (Palandri and Kharaka, 2004). Palandri and Kharaka (2004) combined the precipitation and dissolution kinetic rate constants by microscopic reversibility, to compute the kinetic reaction rate constants, which are assumed to account for both dissolution and precipitation.

Palandri and Kharaka (2004) performed an analysis of the reaction kinetics for calcite based on the work of Plummer et al. (1978) and Talman et al. (1990). Plummer et al. (1978) performed dissolution experiments of calcite in the range of 5°C to 60°C, using pH-stat and free-drift methods,

whilst Talman et al. (1990) studied calcite dissolution between 100°C and 210°C. Based on these experimental results, Palandri and Kharaka (2004) defined the reaction kinetics of calcite dissolution, in accordance with the reaction rate equation (3.33). Thus, the reaction rate for calcite is determined by:

$$\dot{r}_{cal} = -RF_{cal} \left(\frac{A_0}{V} \right) k_{cal,T} \text{sign}(SI_{cal}) |1 - \Omega_{cal}^p|^q, \quad (5.7)$$

where subscript *cal* denotes calcite, and the reaction rate kinetic constant is defined by:

$$k_{cal,T} = k_{cal,T=25^\circ C}^{acid} e^{-\frac{E_{a,acid}}{R} \left(\frac{1}{T} - \frac{1}{298.15} \right)} a_{H^+} + k_{cal,T=25^\circ C}^{neu} e^{-\frac{E_{a,neu}}{R} \left(\frac{1}{T} - \frac{1}{298.15} \right)} \\ + k_{cal,T=25^\circ C}^{base} e^{-\frac{E_{a,base}}{R} \left(\frac{1}{T} - \frac{1}{298.15} \right)} a_{H^+}, \quad (5.8)$$

where the superscripts *acid*, *neu*, and *base* denote that the parameters are mechanisms in acidic, pH neutral, and alkaline conditions. The reaction kinetic rate constants at ambient temperature for the acidic, neutral, and alkaline mechanisms are $10^{-0.3}$, $10^{-5.81}$, and $10^{-3.48} \text{ mol}/m^2s$, and their respective activation energies equal 14.4, 23.5, and 35.4 kJ/mol .

Chou et al. (1989) studied the kinetics and mechanisms of carbonate dissolution at ambient temperature, while varying pH. Pokrovsky and Schott (1999) studied the steady-state dissolution of magnesite at ambient temperature, with various pH. These data were used to parameterize the reaction rate equation (3.33). Saldi et al. (2009) investigated the growth rate of magnesite with pH in the range of 8 ± 0.5 , and demonstrated that at 100°C magnesite has a spiral growth mechanism. Consequently, the *q* parameter is set to 2 (Zieba and Nancollas, 1994; Bose et al., 2008; Saldi et al., 2009). This gives the reaction rate equation:

$$\dot{r}_{mag} = -RF_{mag} \left(\frac{A_0}{V} \right) k_{mag,T} \text{sign}(SI_{mag}) |1 - \Omega_{mag}^p|^q, \quad (5.9)$$

where the subscript *mag* denotes magnesite. The reaction rate constant was defined similarl to calcite. Discussed in Palandri and Kharaka (2004), the activation energy for calcite is applied for magnesite, due absence of available data. The magnesite reaction rate constant is calculated using:

$$k_{mag,T} = k_{mag,T=25^\circ C}^{acid} e^{-\frac{E_{a,acid}}{R} \left(\frac{1}{T} - \frac{1}{298.15} \right)} a_{H^+} + k_{mag,T=25^\circ C}^{neu} e^{-\frac{E_{a,neu}}{R} \left(\frac{1}{T} - \frac{1}{298.15} \right)} \\ + k_{mag,T=25^\circ C}^{base} e^{-\frac{E_{a,base}}{R} \left(\frac{1}{T} - \frac{1}{298.15} \right)} a_{H^+}, \quad (5.10)$$

where the parameters are retrieved from Palandri and Kharaka (2004). The kinetic reaction rate constant at ambient temperatures for acidic, neutral, and alkaline conditions were found to be $10^{-6.38}$, $10^{-9.34}$, and $10^{5.22} \text{ mol}/m^2s$, respectively. Further, their activation energies were defined, in the same order, to be 14.4, 23.5, and 62.8 kJ/mol . It is worth noting that Palandri and Kharaka (2004) assume that the activation energies for calcite are applicable to magnesite in acidic and neutral pH range. This assumption was made due to the lack of data. Herein the same assumption is made.

Discussed by Zeppenfeld (2006), the available data for the reaction kinetics of strontianite are very sparse, and the data that does exist are not very consistent. The reaction kinetic rate constant for strontianite is not defined in the literature. Consequently, k_{str} set to 1. This is an arbitrary number that could be replaced by any number, as it is the product of the parameters in the rate equation that define the rate. One of the few things that are determined for strontianite crystal growth is that it seems to have a spiral crystal growth mechanism (Zieba and Nancollas, 1994). Consequently, the p parameter is set to 2 (Zieba and Nancollas, 1994; Bose et al., 2008; Saldi et al., 2009). Nevertheless, the reaction rate equation for strontianite is similar to the two previous carbonates:

$$\dot{r}_{str} = -RF_{str} \left(\frac{A_0}{V} \right) k_{str} \text{sign}(SI_{str}) |1 - \Omega_{str}^p|^q, \quad (5.11)$$

where subscript str denotes strontianite, conversely the reaction rate constant does not depend on any activities of aqueous species. Since the now simple reaction rate constant is chosen, the reaction rate for strontianite is a product of its parameters. Hence, RF_{str} for both mechanisms control the rate to a greater extent, compared to the other minerals. Consequently, it is more correct to consider RF_{str} as a rate factor, than a reduction factor.

Chou et al. (1989) studied the kinetics and mechanisms of carbonates, including witherite (BaCO_3), at ambient temperatures. Based on these experimental data Declercq and Oelkers (2014) fitted the rate model, thus determined its parameters. The rate equation for witherite is:

$$\dot{r}_{wit} = -RF_{wit} \left(\frac{A_0}{V} \right) k_{wit,T} \text{sign}(SI_{wit}) |1 - \Omega_{wit}^p|^q, \quad (5.12)$$

where subscript wit denotes witherite, and the reaction rate constant is determined using Arrhenius equation (equation (3.18)):

$$k_{wit,T} = A_{acid} e^{-\frac{E_{a,acid}}{RT}} (a_{\text{H}^+})^{0.75} + A_{neu} e^{-\frac{E_{a,neu}}{RT}} (a_{\text{H}_2\text{CO}_3^*})^{0.75} + A_{base} e^{-\frac{E_{a,base}}{RT}} (a_{\text{H}_2\text{O}})^{0.75}, \quad (5.13)$$

where the subscripts $acid$, neu , $base$, denotes acidic, neutral, and basic pH environment. The pre-exponential factors, A_{acid} , A_{neu} , and A_{base} , were found to be $8.86 \cdot 10^4 \text{ mol}/\text{m}^2\text{s}$, $10^5 \text{ mol}/\text{m}^2\text{s}$, and $2.2 \cdot 10^{-10} \text{ mol}/\text{m}^2\text{s}$, respectively, the activation energies $E_{a,acid}$, $E_{a,neu}$, and $E_{a,base}$, equal 34, 21, and 16 kJ/mol . The activity of H_2CO_3^* is, as discussed in section 3.1.2, account for both H_2CO_3 and CO_2 .

Sulphates

The reaction kinetic rate equation for anhydrite was investigated by Palandri and Kharaka (2004), who used the experimental results of Dove and Czank (1995). The reaction rate equation for anhydrite is calculated using:

$$\dot{r}_{anh} = -RF_{anh} \left(\frac{A_0}{V} \right) k_{anh,T} \text{sign}(SI_{cel}) |1 - \Omega_{anh}^p|^q, \quad (5.14)$$

where subscript *anh* denote anhydrite, the kinetic reaction rate constant was defined in the neutral pH zone and its dependency of other component activities was not defined. Thus, using the neutral constant $k_{anh,T=25^\circ C}^{neu} = 10^{-3.19} \text{mol}/\text{m}^2\text{s}$, and its activation energy $E_{a,neu} = 14.3 \text{kJ}/\text{mol}$, in van't Hoff's equation, the reaction rate kinetic constants are extrapolated to desired temperatures:

$$k_{anh,T} = k_{anh,T=25^\circ C}^{neu} e^{-\frac{E_{a,neu}}{R} \left(\frac{1}{T} - \frac{1}{298.15} \right)}. \quad (5.15)$$

Marty et al. (2015) investigated both precipitation and dissolution of celestite. In this thesis celestite only precipitates, consequently the precipitation kinetic parameters are used. The reaction rate equation for celestite is:

$$\dot{r}_{cel} = -RF_{cel} \left(\frac{A_0}{V} \right) k_{cel,T} \text{sign}(SI_{cel}) |1 - \Omega_{cel}^p|^q, \quad (5.16)$$

where subscript *cel* denote celestite, and the empirical exponents *p* and *q* were found to be equal 0.5 and 2 by Marty et al. (2015), respectively. The precipitation rate constant $k_{cel,T}$ was defined by Marty et al. (2015) to be:

$$k_{cel,T} = k_{cel,T=25^\circ C}^{acid} e^{-\frac{E_{a,acid}}{R} \left(\frac{1}{T} - \frac{1}{298.15} \right)} a_{\text{H}^+}^{0.1} + k_{cel,T=25^\circ C}^{neu} e^{-\frac{E_{a,neu}}{R} \left(\frac{1}{T} - \frac{1}{298.15} \right)}, \quad (5.17)$$

where the kinetic rate constant at ambient temperatures are $1.4 \cdot 10^{-6} \frac{\text{mol}}{\text{m}^2\text{s}}$ for acidic, and $2.2 \cdot 10^{-8} \frac{\text{mol}}{\text{m}^2\text{s}}$ for neutral conditions, and the activation energies $E_{a,acid}$ and $E_{a,neu}$ found to be $33 \frac{\text{kJ}}{\text{mol}}$ and $34 \frac{\text{kJ}}{\text{mol}}$, respectively. Discussed by Palandri and Kharaka (2004), the acidic mechanism extends to alkaline conditions, therefore the parameters from Marty et al. (2015) are assumed to be valid.

6 | Results and Discussion

This chapter consists of results and discussion regarding the choices made to develop and adjust the 1D advection-dispersion-reaction (ADR) model. The first section considers the choice of which minerals to include. The basis for these discussions are the static simulations and experimental findings from Andersen et al. (2018) and Korsnes and Madland (2017) on MO10, M9, and M12. In addition to the results presented in Andersen et al. (2018) and Korsnes and Madland (2017), the geochemical and SEM-analysis of M9 and M12 have been performed to support this work.

The second section considers discussion regarding the choice of kinetic parameters needed for the dynamic model and how the parameters were adjusted to match the experimental data. In the third section, the chosen tuning parameters are used to simulate the complete flooding experiments of each core. Results from full core flooding simulations are compared with experimental results and discussed. Further, these simulations are used to discuss the assumed substitution-like reaction mechanism.

6.1 Mineral Selection from the Static Model

From the static modeling saturation indexes (SI) for several minerals were analyzed at $130 \pm 5^\circ\text{C}$. As a first cut-off, all minerals with $SI < -1$ were not considered, reducing the list to 16 minerals, listed in table 6.1. The SI 's from the sequentially flooded brines equilibrated with calcite are not tabulated, since no other minerals were indicated from the sequenced brines. The choice of cut-off SI -value is arbitrary. According to theory discussed in subsection 3.1.4 it is reasonable to set the SI cut-off to zero, as precipitation only occur when a mineral is super-saturated. Nevertheless, many of the under-saturated minerals in table 6.1 are associated with chalk and the minerals included (Hänchen et al., 2008; Azimi and Papangelakis, 2011; Madland et al., 2011; Borromeo et al., 2018; Mindat.org, 2019), therefore relevant to discuss. In addition to the 16 minerals passing the first screening, celestite (SrSO_4) is also discussed due to EDS-SEM findings.

It is desired to develop a realistic, but not-too-complex model. Thus, carbonates and sulphates bound with one divalent cation are preferred. To discuss what minerals that can explain the different ion retention and production, experiments of similar character to the experiments conducted by Andersen et al. (2018) and Korsnes and Madland (2017) are evaluated for relevance, and used to support inclusion and exclusion of potential precipitants.

In the following all minerals that passed the first screening or was detected by SEM-imaging, will be evaluated, based on experimental studies and literature. First, the minerals that are included in the dynamic model are discussed, followed by the excluded ones.

Anhydrite, CaSO_4 , was only super-saturated when brine 5, which consist of Ca^{2+} and SO_4^{2-} , was included. This brine was only used to flood in the M9 core, and it was the last brine used. Korsnes and Madland (2017) discussed, when flooding with brine 5: "*The effluent profile shows a retention time lasting for 15 days for both SO_4^{2-} and Ca^{2+} before the ions reached their original concentration. After this peak, both ion concentrations started to drop, and the test was stopped due to clogging*". Madland et al. (2011) proved that anhydrite precipitate during synthetic seawater flooding of Stevns Klint and Liège at 130°C. Therefore, it is reasonable to assume that precipitation of anhydrite clogged the M9 core, hence include it in the model.

Calcite, CaCO_3 , is initially more than 99% of the Mons chalk core (Megawati et al., 2015; Korsnes and Madland, 2017; Andersen et al., 2018) used in the flooding experiments. EDS-SEM analysis indicate the presence of CaCO_3 both as a primary and a secondary mineral, demonstrated in figure A.2. Thus, it is included.

Celestite, SrSO_4 , was not printed in the SI-calculations since non of the brines listen in table 2.1 nor the mixes of sequenced brines in Korsnes and Madland (2017) gave celestite as a potential precipitant. The SEM-images of the M9 core gave findings of a newly formed, rather large and compact mineral, see figure A.1. EDS-SEM analysis of this mineral indicate that it is a SrSO_4 mineral. Shown in figure 2.4, strontium is retained in the M9 core, and barely back produced in later sequences. In later sequence sulphate is injected and (initially) retained. It is reasonable to believe that the retained strontium from the second flooding sequence in core M9, will partially redissolve, due to under-saturation, and react with the injected SO_4^{2-} . This in turn, support celestite to account for these experimental observations. Hence, celestite is included in the model.

Magnesite, MgCO_3 , was proved by XRD-analysis performed by Zimmermann et al. (2015) after a long term MgCl_2 -flooding experiment on Liège chalk, and by Korsnes and Madland (2017) after the flooding experiments of Mons chalk. Egeland et al. (2017) demonstrated that magnesite was formed as a secondary mineral, both from short and long term tests. Discussed by Hänchen et al. (2008), hydromagnesite was de-hydrated into magnesite at elevated temperatures. Furhter, Hänchen et al. (2008) concluded that magnesite was to be the most stable Mg-carbonate under all the tested conditions. Mona W. Minde performed SEM-analysis on slice 5 of the M12 core, without identifying magnesite. It is reasonable to assume that it has precipitated, and dissolved in the following non-Mg flooding sequences. Illustrated in figures 2.2 and 2.3, Mg is retained and later back-produced. Thus, it is included.

Strontianite, SrCO_3 , is associated with experimental results from flooding experiments of carbonate and brines with Sr^{2+} . During flooding, Sr^{2+} was retained with corresponding ammounts of the sum of Ca^{2+} and Mg^{2+} , making it theoretically possible that SrCO_3 will form as CaCO_3 and MgCO_3 is decomposed (Korsnes and Madland, 2017). SEM-analysis of the cores, performed as an addition to this work, indicated that Sr-bearing carbonates were formed, demonstrated in figure A.3. Compar-

ing these with mineral structure from literature, e.g. Mindat.org (2019), indicate that the secondary minerals are shaped as strontianite. Consequently, strontianite is included.

Witherite, BaCO_3 , was indicated with EDS-SEM analysis of the inlet slice of the M12 core, see figure A.4. The SEM-imaging of the Ba-bearing mineral, has structural shape very similar to the witherite crystals identified by Blount (1974). Moreover, the mineral is according to Mindat.org (2019) of a hexagonal structure, with relatively higher molecular weight compared to calcite, thus based on BSE and SE imaging, brighter hexagonal secondary minerals were observed. Furthermore, the loss of Ba^{2+} ions when flooding the cores are evident, illustrated in figure 2.4 and 2.3. Witherite was also highly over-saturated, from the equilibrium (static) model in PHREEQC. Therefore, witherite is included in the model.

The following minerals discussed were not included:

Alstonite, $\text{BaCa}(\text{CO}_3)_2$, is a low-temperature hydrothermal mineral (Mindat.org, 2019). Thus, alstonite is not included in the model.

Aragonite, CaCO_3 , has the same chemical composition as Calcite, but it is more soluble, has a higher formation pressure, and has higher density than calcite (Carlson, 1980; Morse and Mackenzie, 1990). Furthermore, it was not detected by Borromeo et al. (2018) using Raman Spectroscopy on MgCl_2 -flooded Liège Belgium chalk cores at 130°C and injection rate of 1 PV/day. Hence, aragonite is not included in the model.

Artinite, $\text{Mg}_2\text{CO}_3(\text{OH})_2 \cdot 3\text{H}_2\text{O}$, was not detected by Borromeo et al. (2018) using Raman Spectroscopy on MgCl_2 -flooded Liège Belgium chalk cores at 130°C and injection rate of 1 PV/day. Thus, artinite is not included in the model.

Barytocalcite, $\text{BaCa}(\text{CO}_3)_2$, is a polymorph of alstonite. Due to the same argument as for alstonite, barytocalcite is not included in the model.

Bassanite, $\text{CaSO}_4 \cdot 0.5\text{H}_2\text{O}$, was nearly saturated in brine 5 according to the static model, see table 6.1. In an experimental study of replacement of calcite by calcium sulphate by Ruiz-Agudo et al. (2015), a calcite crystal (Iceland spar) was placed in 0.1M sulphuric acid at 22°C and heated to 60°C , 120°C , and 200°C . Ruiz-Agudo et al. (2015) concluded that at low temperatures both bassanite and gypsum were formed, but at temperatures above 120°C both minerals were transformed into Anhydrite. This experiment was conducted at very acidic conditions, i.e. low pH, but the transformation into anhydrite at elevated temperatures is still reasonable to take into account in the evaluation of which minerals to include in the dynamic model. Thus, bassanite is not included in the model.

Brucite, $\text{Mg}(\text{OH})_2$, was not detected by Hänchen et al. (2008) even though it was super-saturated. Further, simulations performed by Wang et al. (2019) indicate that magnesite will precipitate before brucite, thereby reducing Mg^{2+} concentration and activity, keeping brucite under-saturated. Therefore, brucite is excluded from the model.

Dolomite, $\text{CaMg}(\text{CO}_3)_2$, formation is according to Morse and Mackenzie (1990): "... kinetically hindered by its complex and well-ordered structure". Even though results from automated SEM mineral liberation analysis performed by Andersen et al. (2018) indicated formation, the later XRD-analysis of the MgCl_2 flooded chalk cores did not verify the presence of dolomite. In accordance to this citation, XRD-analysis performed by Zimmermann et al. (2015), and SEM-analysis performed by Minde (2018) demonstrated that there were either no dolomite minerals in the flooded cores, or that the amount is below the detection limit. Thus, dolomite is not included in the model.

Gypsum, $\text{CaSO}_4 \cdot 2\text{H}_2\text{O}$, both Zimmermann et al. (2015) and Borromeo et al. (2018) compared pre- and post-flooded SEM-data of MgCl_2 -flooded Liège Belgium chalk, and found that the initially present gypsum was dissolved. Ruiz-Agudo et al. (2015) concluded that at low temperatures and both bassanite and gypsum was formed, but above 120°C both minerals were transformed into Anhydrite. This experiment is conducted at very acidic conditions, i.e. low pH, but the transformation into anhydrite at elevated temperatures are still reasonable to take into account in the evaluation of which minerals to include in the dynamic model. Azimi and Papangelakis (2011) studied the transformation of gypsum to anhydrite. They concluded that at temperatures greater than 100°C , dehydration of gypsum to anhydrite occurred rapidly, and that the dehydration was further accelerated by NaCl. Hence, gypsum is not included in the model.

Huntite, $\text{CaMg}_3(\text{CO}_3)_4$, was super-saturated, thus the static model indicate that it could precipitate. Nevertheless, it was not detected by Borromeo et al. (2018) using Raman Spectroscopy on long (1.5 years) and ultra-long (3 years) MgCl_2 -flooded Liège Belgium chalk (95% pure calcite) cores, at 130°C . Thus, huntite is not included in the model.

Hydromagnesite, $\text{Mg}_5(\text{CO}_3)_4(\text{OH})_2 \cdot 4\text{H}_2\text{O}$, was detected at early stages of the experiment by Hänchen et al. (2008), but at elevated temperatures, e.g. 120°C the newly formed hydromagnesite was transformed into magnesite. Further, hydromagnesite was not detected by Borromeo et al. (2018) using Raman Spectroscopy on MgCl_2 -flooded Liège Belgium chalk cores at 130° and injection rate of 1 PV/day. Thus, hydromagnesite is not included in the model.

Periclase, MgO , is only slightly super-saturated for brine 7, which has high Mg^{2+} concentration (see table 2.1). Furthermore, magnesite, which has been proven to be precipitated (Hänchen et al., 2008; Korsnes and Madland, 2017; Minde, 2018) is more over-saturated and it is more stable Hänchen et al. (2008), i.e. $SI_{\text{magnesite}} > SI_{\text{periclase}}$, thus it is likely that magnesite will precipitate before periclase becomes super-saturated. Consequently, periclase is not included.

Brine	1	2	3	4	5	6	7	8	9	10
Alstonite			-0.52						0.16	
Anhydrite		-1.06		-1.30	0.65					
Aragonite	-0.15	-0.15	-0.15	-0.15	-0.15	-0.15	-0.15	-0.15	-0.15	-0.15
Artinite				1.73		2.31	3.69			
Barytocalcite			-0.68						0.01	
Bassanite		-1.72		-1.96	-0.02					
Brucite				2.34		2.65	3.46			
Calcite	0.00	0.00	0.00	0.00	0.00	0.00	0.00	0.00	0.00	0.00
Dolomite				2.98		3.25	3.82			
Gypsum		-1.77		-2.01	-0.07					
Huntite				4.44		5.25	6.95			
Hydromagnesite				4.54		5.92	9.01			
Magnesite				1.83		2.09	2.66			
Periclase				-0.86		-0.55	0.26			
Strontianite			2.58					3.46		
Witherite			4.26						4.95	

Table 6.1: Mineral saturation indexes, SI , in static equilibrium between brines listed in table 2.1 with pure calcite, CaCO_3 .

6.2 Kinetic Parameters in the Dynamic Model

6.2.1 Dispersion

To choose a valid dispersion coefficient, the method discussed in section 5.2.3 was used. Initially, it was assumed that the time in the provided data set, when injection brines are changed, were correct. The plot of the normalized Cl^- concentration versus time after the switch of injection brine for the M12 core is presented in figure 6.1.

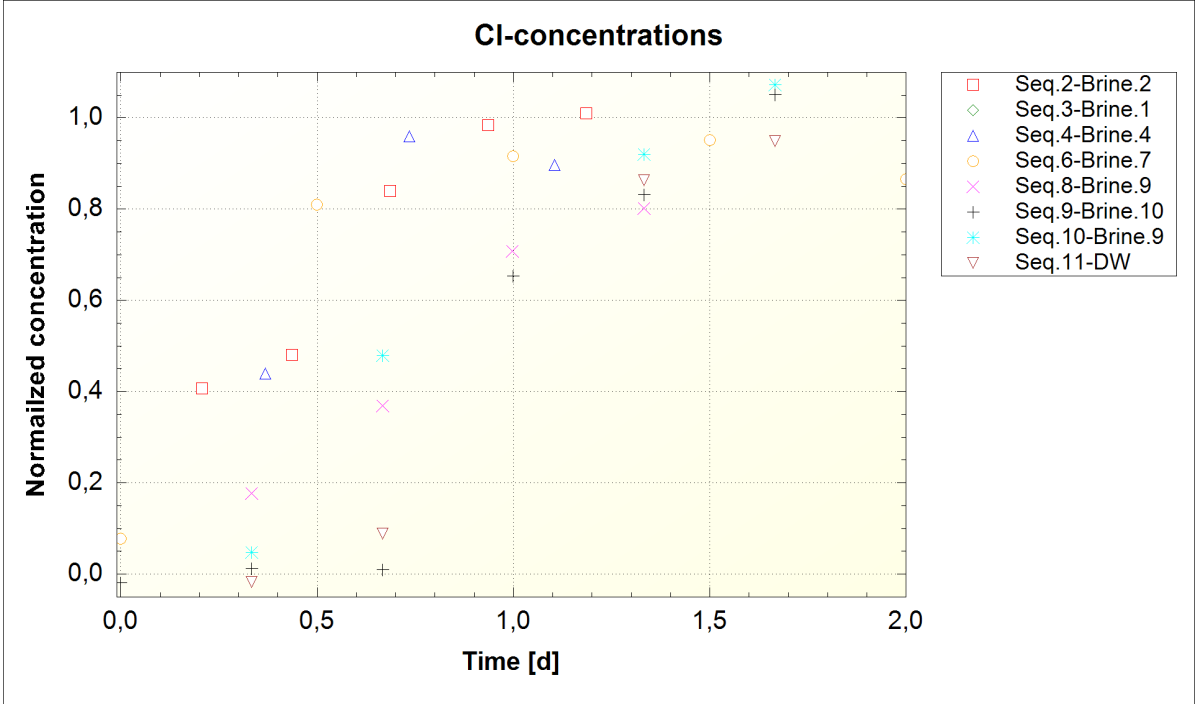


Figure 6.1: Normalized Cl concentrations in accordance with equation (5.3) for brines used when flooding the M12 core. Note that the names of the normalized concentrations are a combination of the flooding sequence and the brine used.

Theoretically, the breakthrough, i.e. $\bar{c} = 0.5$ (using equation (5.3)), should have occurred at approximately 1 day, equal to pore volume (PV) injected. Demonstrated in figure 6.1, all of the brines had a too early breakthrough. Indicating that this assumption may not be valid. The lack of validity may be a result of several reasons. One uncertainty is how much the porosity was reduced when the core was loaded beyond yield at the initial stage, see (Korsnes and Madland, 2017) for further details. To determine the dispersion, the normalized concentrations are manually shifted such that the at $Time = 1\ day$ the normalized concentrations are within 0.5 ± 0.05 , such that the trend of the measured concentrations can be captured. Discussed in subsection 3.2.3 the transportation of a non-reactive component is controlled both by diffusion and advection-driven random distribution, in addition to the advective transportation. Thus, by defining the dispersivity, α_L in equation (3.28), to zero, the diffusion will account for both diffusion and dispersion. In turn, transportation of non-reactive components can be computed considering only diffusion and advection.

To determine what range the diffusion parameter could reasonably be within, diffusion coefficients from literature are used. In the user manual for PHREEQC, the default diffusion coefficient is $3 \cdot 10^{-10} \text{ m}^2/\text{s}$ (Appelo and Parkhurst, 2013). Madland et al. (2011) chose a total dispersion coefficient of $10^{-8} \text{ m}^2/\text{s}$ in their model made to match effluent experimental data, using Cl^- as tracer ion. Goody et al. (2007) demonstrated that the diffusion coefficient had the range of $3.1\text{-}8.7 \cdot 10^{-10} \text{ m}^2/\text{s}$ in chalk with porosity of 32 to 48%, using Cl^- as tracer ion. Witthüser et al. (2006) concluded that the diffusion coefficient in chalk to be $8 \cdot 10^{-10} \text{ m}^2/\text{s}$ for Sr^{2+} and $1.3 \cdot 10^{-9} \text{ m}^2/\text{s}$ for Na^+ . Rumynin (2012) gathered results from experimental data, when considering both dispersion and dispersivity. The typical value of the dispersion coefficient in chalk-marl deposits with a porosity of 35-40% were found to be up to $5 \cdot 10^{-10} \text{ m}^2/\text{s}$ (Rumynin, 2012)[p.13], whilst the dispersivity (α_L) ranged between $10^{-4}\text{-}10^{-2} \text{ m}$ (Rumynin, 2012)[p.15]. In simplified pore structure, Tansey (2016) used a constant molecular diffusion coefficient of $3.6 \cdot 10^{-9} \text{ m}^2/\text{s}$. According to Appelo and Postma (2005) is it sufficient to use a constant diffusion coefficient for simple electrolytes of approximately $10^{-9} \text{ m}^2/\text{s}$. Based on these coefficient values, a good approximation for the diffusion coefficient is around $10^{-10}\text{-}10^{-9} \text{ m}^2/\text{s}$.

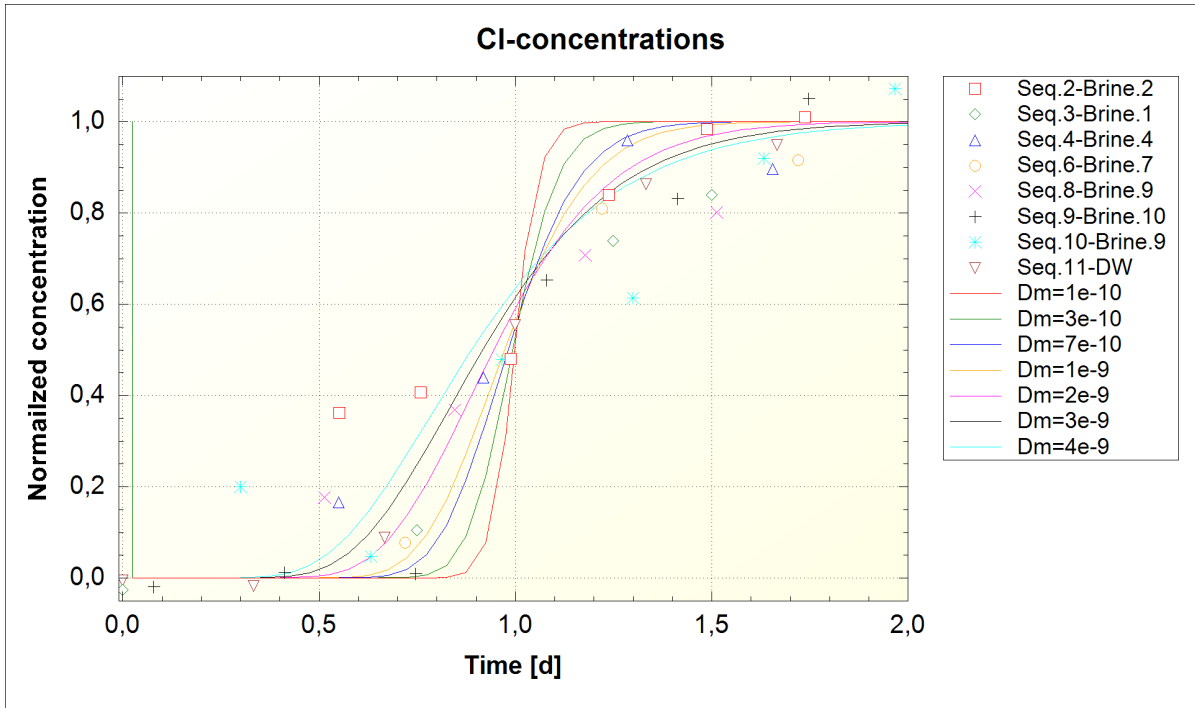


Figure 6.2: Normalized Cl concentrations in accordance with equation (5.3) for brines used when flooding the M12 core. Note that the names of the normalized concentrations are a combination of the flooding sequence and the brine used. Simulations with different dispersion coefficients (D_L).

Demonstrated with figure 6.2, there are several hydrodynamic dispersion coefficients that could be used to explain the dispersion. Since the diffusion coefficient is accounting for both the dispersion and diffusion, values higher than what was suggested in literature was tested. Similar to Andersen et al. (2018), were the dispersivity (α_L) set to zero, causing the dispersion and diffusion to be identical. The dispersion coefficient is set to be $2 \cdot 10^{-9} \text{ m}^2/\text{s}$, i.e. the same as Andersen et al. (2018) used to match experimental data presented in section 2.3. This dispersion coefficient is assumed equal for all components (Parkhurst and Appelo, 1999).

6.2.2 Tuning of Reaction Kinetic Parameters

By using the reaction kinetic parameters retrieved from the literature without any adjustments, the software fails due to too high rates. Consequently, tuning parameters have to be adjusted to reduce the reaction rates. Discussed by Blount (1974), who studied the growth rate of synthetic barium and strontium sulphate and carbonates, the crystal growth rate is much slower in nature, than those observed in the laboratory. This is further coupled to the difference between single-grain mineral growth, which is the basis of many kinetic parameters, and the mineral growth in the porous material. Consequently, the tuning parameters RF , p and q are required to adjust the simulated reaction rates to match effluent concentrations and mineral distribution.

$$\dot{r}_j = -RF_j \left(\frac{A_0}{V} \right) k_j \text{sign}(SI_j) |1 - \Omega_j^{p_j}|^{q_j}, \quad (3.33)$$

where the reduction factor RF affects the net rate, whilst the exponent tuning factors, p and q , control how the rate is affected by the degree of saturation. To determine the rate of dissolution-precipitation reactions, the steady-state rates are evaluated. At steady-state, the reaction rate is constant (steady), and the rate is directly proportional with the final mineral distribution, determined by geochemical analysis. The transient state reactions are beyond the scope of this thesis, thus gradually changing effluents are not matched.

It was evident that the reaction rate parameters from literature had to be reduced. Initially, the matching was done with the assumption that the tuning parameters accounted for both dissolution and precipitation. During the early stages of effluent matching, it was recognized that RF tuning parameters could account for both dissolution and precipitation. Since dissolution and precipitation are two different mechanisms, it is logical that they require different sets of tuning parameters. To avoid making the model too complex the p and q parameters are assumed to be mechanism independent. Subsequently, RF has to be adjusted for each mechanism. Consequently, the model 4 tuning parameters for each mineral: p_j , q_j , RF_j^{dis} and RF_j^{prec} , for each mineral j , where dissolution and precipitation are denoted by *dis* and *prec*. In other reactive simulations considering minerals dissolution and precipitation, the two mechanisms are given different sets of kinetic parameters, depending on different factors, similar to the model by Marty et al. (2015). This may make the model more accurate, consequently giving it better history matching and predictive abilities. Nevertheless, since there are great uncertainties of how dissolution and precipitation occur in transport situations, like reactive flow in porous carbonate material, such precise kinetic material may not give better predictive results.

Discussed in subsection 3.1.4, the super-saturation of a mineral has to go beyond the metastable region to precipitate. Consequently, it is not necessarily sufficient for a mineral to be slightly super-saturated for it to precipitate. Furthermore, it is important to state that dissolution is assumed to occur for all $SI < 0$. To capture this effect of metastable super-saturation p and /or q are adjusted. Moreover, p and q are also adjusted to partially control where in the core, i.e. the depth in the core reaction is occurring.

The first minerals considered are calcite (CaCO_3) and magnesite (MgCO_3). In the MO10 core, Mg^{2+} was the only reactive specie injected. By assuming the selected minerals account for all minerals involved, the effluents and mineral distribution of MO10 are to determine the reaction rates of calcite and magnesite. For the MO10 core both the effluent concentrations of Ca^{2+} and Mg^{2+} , and final mineral distribution are used. Discussed by Andersen et al. (2018), slice 1 to 3 had the highest content of magnesite, and in the 4 later slices the magnesite content was diminishing. Consequently, the model had to compute most of the magnesite precipitate near the inlet.

Palandri and Kharaka (2004) stated that the parameters p and q by default set to 1, if not empirically determined for a mineral. Consequently, p_{cal} , q_{cal} and p_{mag} are set equal to 1. q_{mag} was found to be 2 by Saldi et al. (2009), as stated in subsection 5.2.4. Further, the RF_{cal}^{dis} and RF_{mag}^{prec} from Andersen et al. (2018) were used as the initial guess. It was evident that the perfect matching of effluents and mineral distribution was impossible to achieve. By matching the effluent, the magnesite relative precipitation distribution was spread too evenly through the core. Moreover, by matching relative magnesite distribution, the magnesite precipitation and the corresponding calcite dissolution were too low, that is Ca^{2+} and Mg^{2+} effluents were too low and too high, respectively.

To determine p_{mag} both the magnesite distribution within MO10 and its effluent were considered. Stated above, most of the precipitated magnesite was near the inlet. In fact, slice 3 contained 3 times more magnesite than the outlet slice. By using a $p_{mag} < 1$ the precipitation rate was rather constant through the core, as illustrated in figure 6.3.

Based on the findings of Shiraki and Brantley (1995), the precipitation rate of magnesite increased exponentially as the saturation ratio for magnesite increased beyond 1.72, i.e. $\Omega_{mag} > 1.72$. Consequently, p_{mag} was tested for values greater than 1. This produced better matching and more interesting results. Demonstrated in figure 6.4, the best-fit parameter combination was used to match the relative magnesite precipitation rate through the core.

In figure 6.4 the content of magnesite is presented as a relative amount of magnesite in each slice, where the basis is the magnesite amount in the outlet slice (s7. in figure 2.5 C)). Further, since no transient reaction effects are considered, the steady-state reaction rate for each cell presented relative to the steady-state reaction rate of the last cell in the simulation and compared with the relative magnesite amount. Shown in figure 6.4, the precipitation rate did not capture the gradually increasing amount from s1. to s3., but it computed the relative rate difference between near inlet and outlet similar to the mineral distribution, and it reproduced the *decreasing towards outlet* trend.

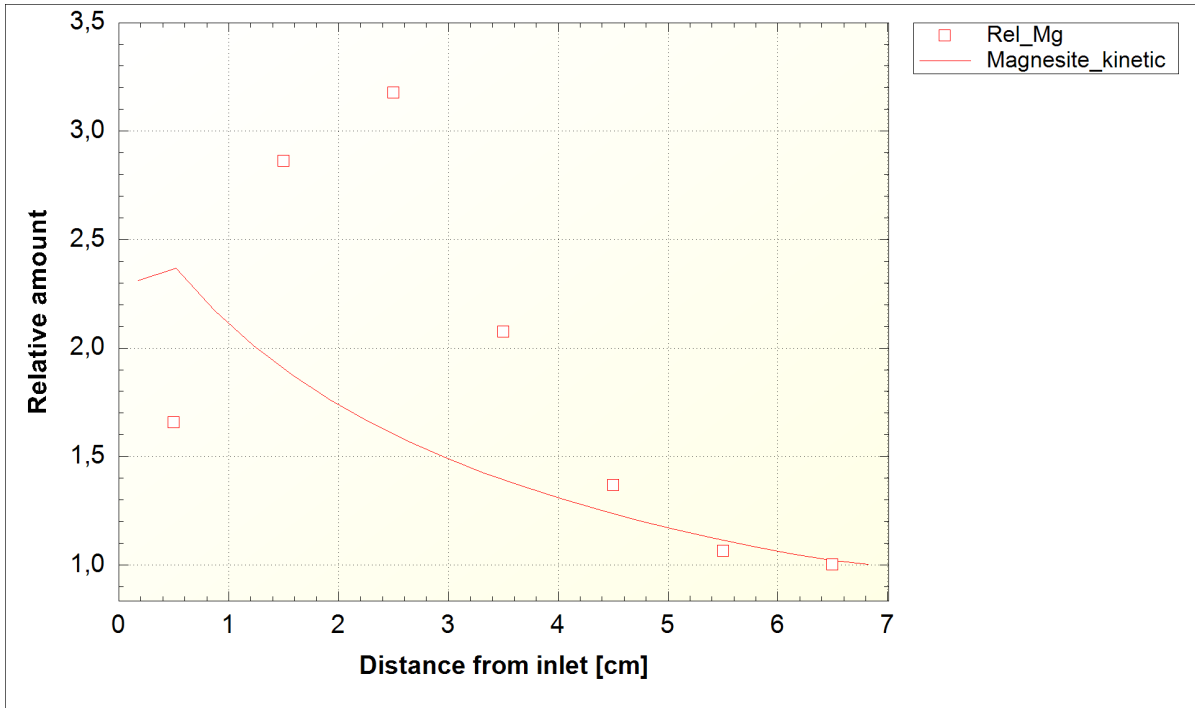


Figure 6.3: Demonstration of the effect of using $p < 1$, while still matching the effluents. In this figure the relative mineral distribution of magnesite (MgCO_3) after MgCl_2 . *Rel_Mg* denote the amount of magnesite in each slice relative to the amount in the outlet slice (s7.), and *Magnesite_kinetic* denote the precipitation reaction rate for magnesite relative to the precipitation rate in the last cell.

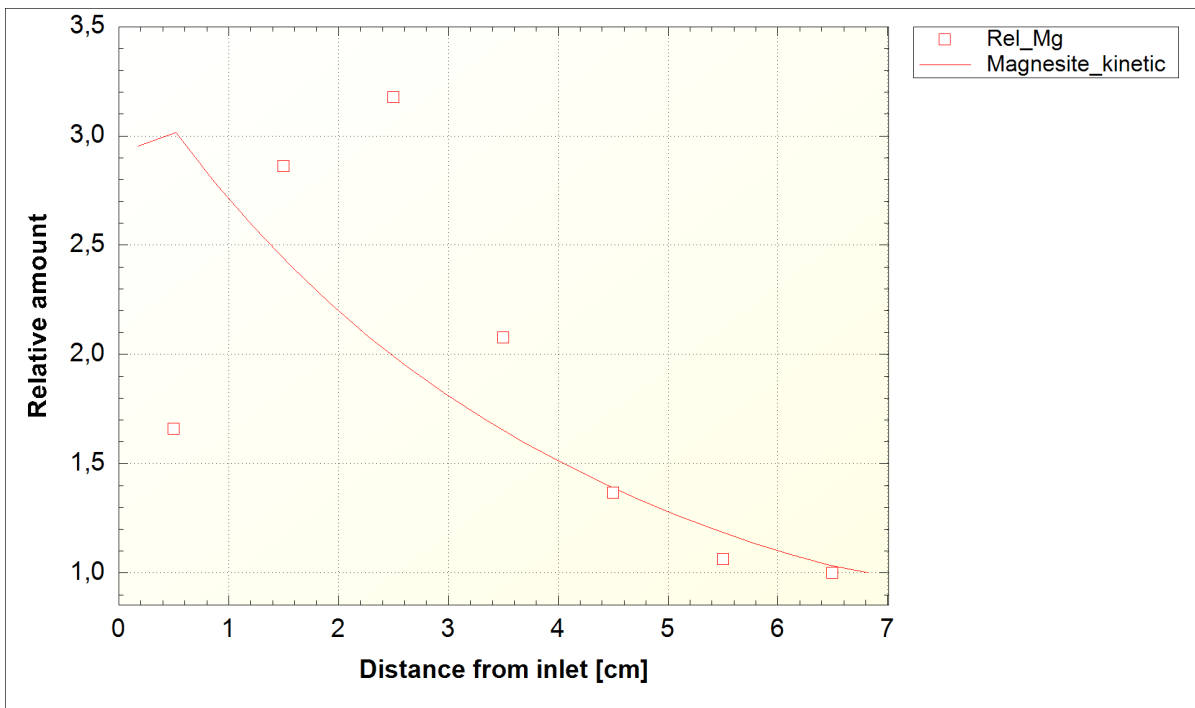


Figure 6.4: Matching the distribution of magnesite (MgCO_3) content relative to the outlet slice, with the simulated relative kinetic precipitation rate of magnesite. Similar to figure 6.3, the *Rel_Mg* denote the amount of magnesite (MgCO_3) in each slice relative to the amount in the outlet slice (s7.), and *Magnesite_kinetic* denote the precipitation reaction rate for magnesite relative to the precipitation rate in the last cell.

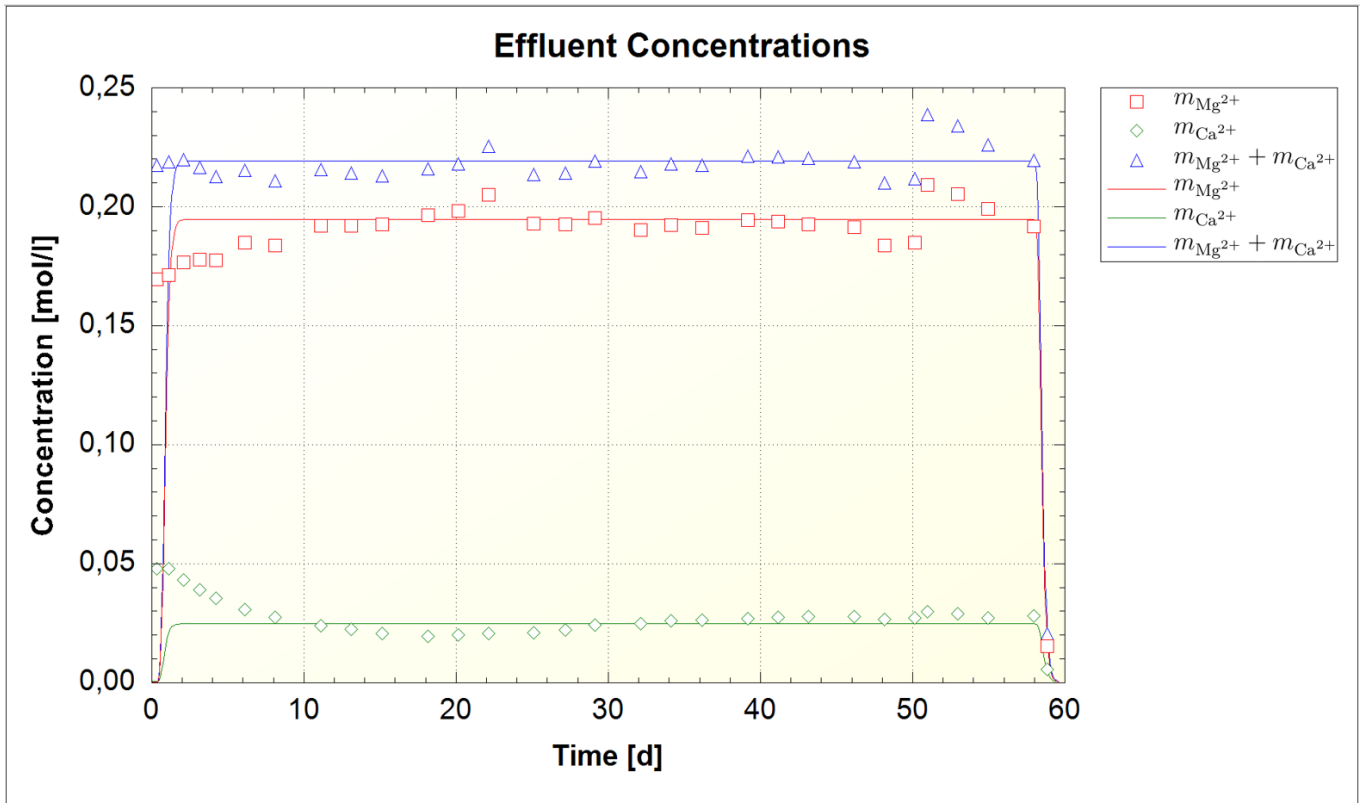


Figure 6.5: Best match of MO10 effluent concentration.

Further, to test these tuning parameters with other brine compositions and experiments, Mg^{2+} injection sequences in M12 were computed with the parameters from the MO10 core. Meaning flooding sequences 4, 5, and 6 of core M12, where brines 4, 6, and 7 (see table 2.1 for composition) were flooded. Illustrated in figure 6.6, during brine 4 injecting, containing SO_4^{2-} , the effluents of Ca^{2+} and Mg^{2+} are gradually decreasing and increasing, respectively. This transient effect is not captured. Due to the transient behaviour of the effluent, these data were not further considered. Flooding with brine 6 gave steady effluent concentrations, and the parameters picked from the MO10-matching gave a good match. Illustrated in the transition from brine 4 to brine 6, the simulated concentration of Ca^{2+} increase and a corresponding decrease in Mg^{2+} occur. The change in dissolution-precipitation is related to the activity reduction of the reactive constituents, such as $a_{\text{Mg}^{2+}}$ and $a_{\text{Ca}^{2+}}$, due to the complex formation in the aqueous phase.

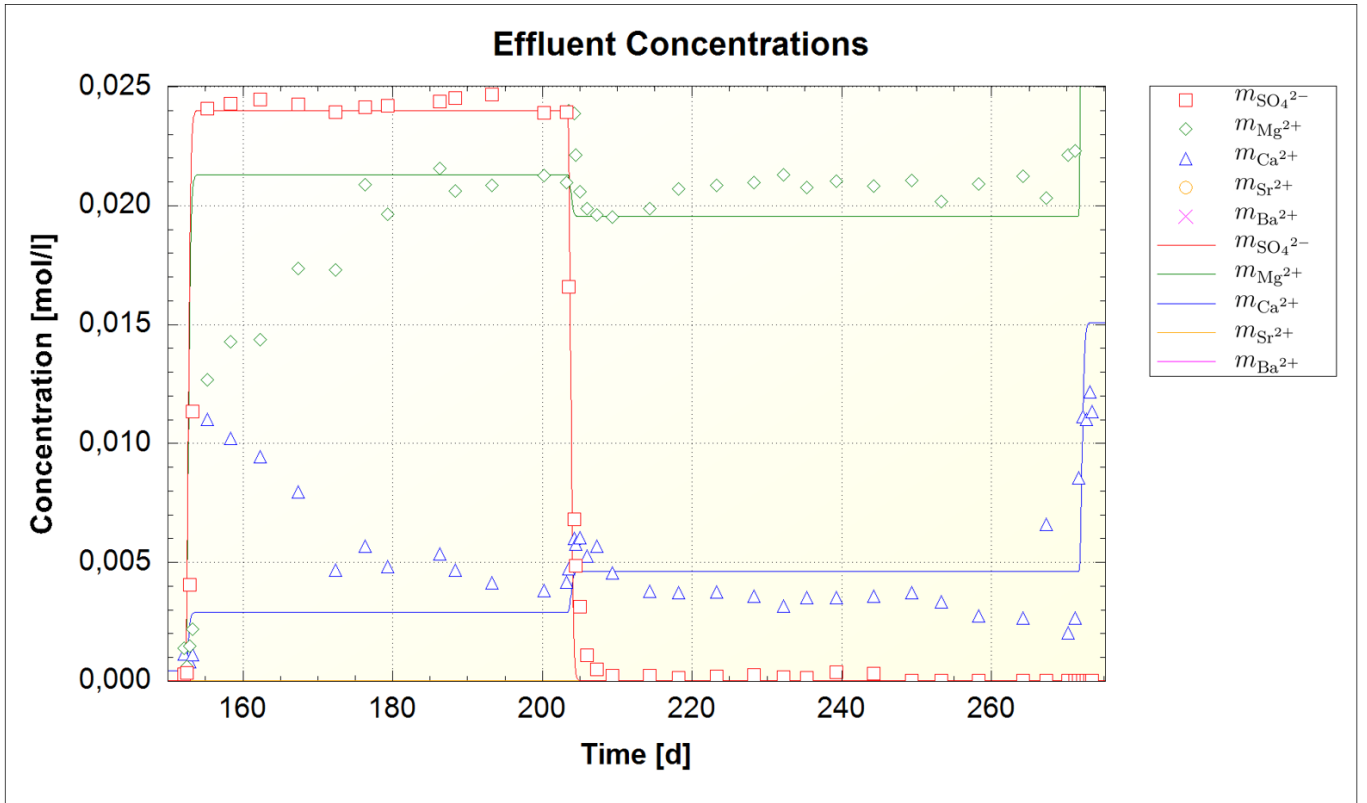


Figure 6.6: Best match of M12 effluent concentration of flooding sequence 4 and 5, using brine 4 and 6, respectively. Tuning parameters picked from MO10 effluent and mineral distribution matching.

In the 6th sequence of M12, brine 7 was injected. The Mg^{2+} concentration in brine 7 was 5 times higher than in the two previous brines, i.e. brines 4 and 6. The parameters from the MO10 MgCl_2 experiment computed good matches with the effluent concentrations. The gradually increasing Ca^{2+} and decreasing Mg^{2+} effluents might be related to several phenomenons. Such as the increased compaction rate during MgCl_2 injection, observed by Korsnes and Madland (2017), which, may cause matrix grain restructuring, consequently revealing new reactive mineral surface area (Pedersen et al., 2016). Another explanation is that the available surface has been observed to increase when outcrop chalk cores are flooded with MgCl_2 brines at elevated temperatures (Andersen et al., 2018). Since deformation of the core and varying available surface area are effects beyond the scope of this thesis, the gradual increase Ca^{2+} and decrease Mg^{2+} effluents, are not considered.

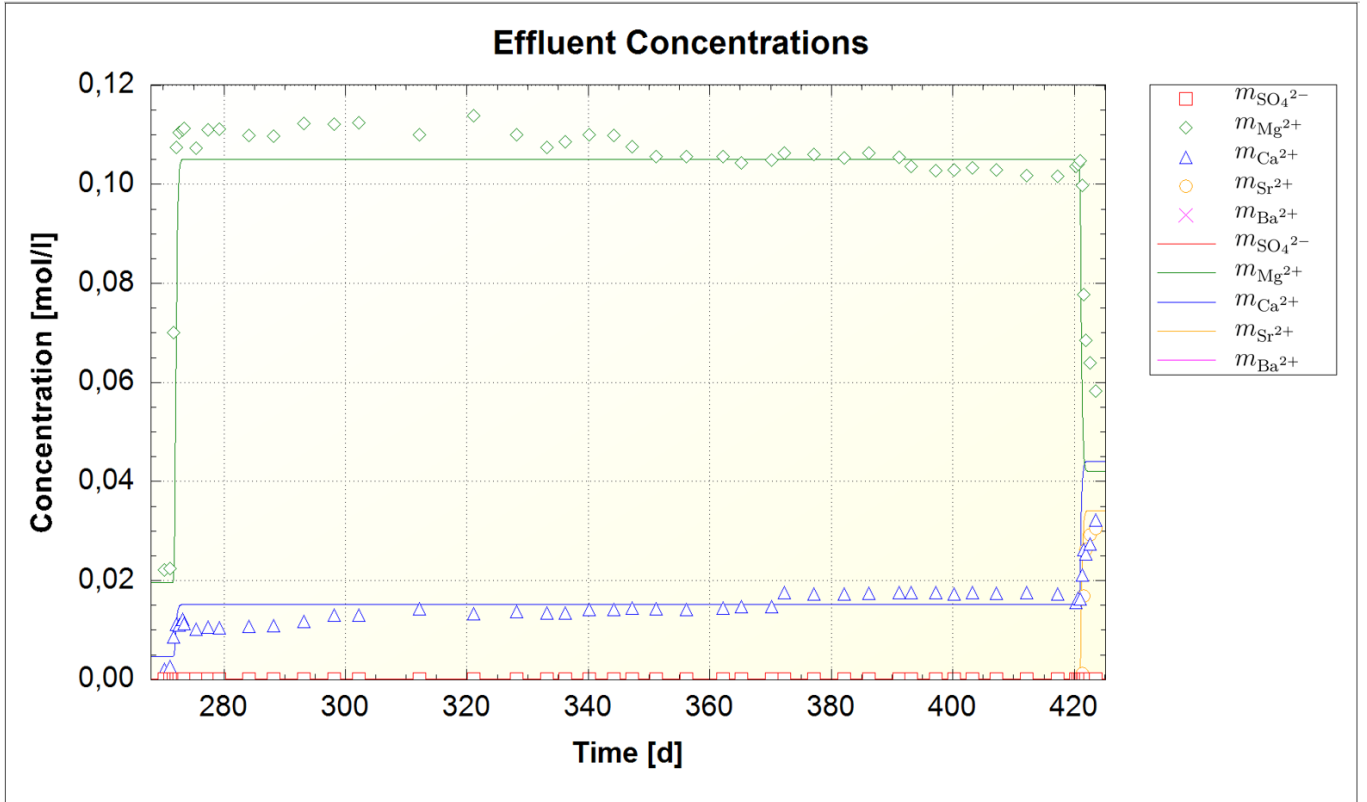


Figure 6.7: Best match of M12 effluent concentration of flooding sequence 6, using brine 7. Tuning parameters picked from MO10 effluent and mineral distribution matching.

The tuning parameter set consisting of $RF_{cal}^{dis} = 2.7 \cdot 10^{-6}$, $RF_{mag}^{prec} = 2.0 \cdot 10^{-5}$, and $p_{mag} = q_{mag} = 2$ gave good match with the $MgCl_2$ brines used in MO10 and M12, as demonstrated in figures 6.5, 6.6, and 6.7. These parameters are assumed to be the best-fit for calcite ($CaCO_3$) dissolution and magnesite ($MgCO_3$) precipitation, therefore valid in the following matching sequences.

Shown in figure 2.4, when M9 is flooded with brine 3, the influent and effluent concentration of Ba^{2+} are almost identical. To get a first approximation for strontianite ($SrCO_3$) precipitation, it is assumed that calcite ($CaCO_3$) will dissolve and strontianite will precipitate. Based on Ba^{2+} effluent, witherite ($BaCO_3$) precipitation is assumed to not occur. This is modelled by temporarily defining witherite precipitation rate to zero. By using these first approximated M9-fitted strontianite parameters, shown in figure 6.8, on the M12 brine 8 sequence, demonstrated in figure 6.9, the strontianite ($SrCO_3$) precipitation rate became too low. It was recognized that by tuning p_{str} in equation (5.11), i.e. the reaction rate for strontianite, the reaction rate term for strontianite might provide a better match for both M9 and M12 strontianite precipitation flooding sequences.

The p parameter, which more directly affects the reaction rate compared to the q parameter, was tested within the range 0.5 to 5. For each p_{str} value tested a RF_{str}^{prec} was determined. Using these parameters in M12 brine 8 flooding sequence, the (not-yet-determined) RF_{mag}^{dis} was adjusted to give the best match with the experimental effluent. RF_{mag}^{dis} was tested over a wide range, both greater and smaller than 1. Nevertheless, the PHREEQC model did not manage to run the simulation with a large enough RF_{mag}^{dis} to match the effluents. The general results using the discussed p_{str}

and corresponding RF_{str}^{prec} , were that Sr^{2+} effluents were too high, i.e. too low precipitation rate for strontianite ($SrCO_3$), thus too low dissolution rate of calcite ($CaCO_3$) and magnesite ($MgCO_3$). Simulations indicate that strontianite precipitation is the limiting reaction rate. Consequently, by increasing calcite and magnesite dissolution rates will not affect rate of strontianite precipitation. Consequently, it was recognized that a RF_{str}^{prec} parameter did not account for both M9 and M12, and therefore a rate factor was determined for each core. To demonstrate this, the effluents from the Sr^{2+} injection sequences for both M9 and M12, using $p_{str} = 2$ with the best-fit RF_{str}^{prec} from the M9 core in both the M9 and M12 Sr^{2+} flooding sequences are shown in figures 6.8 and 6.9.

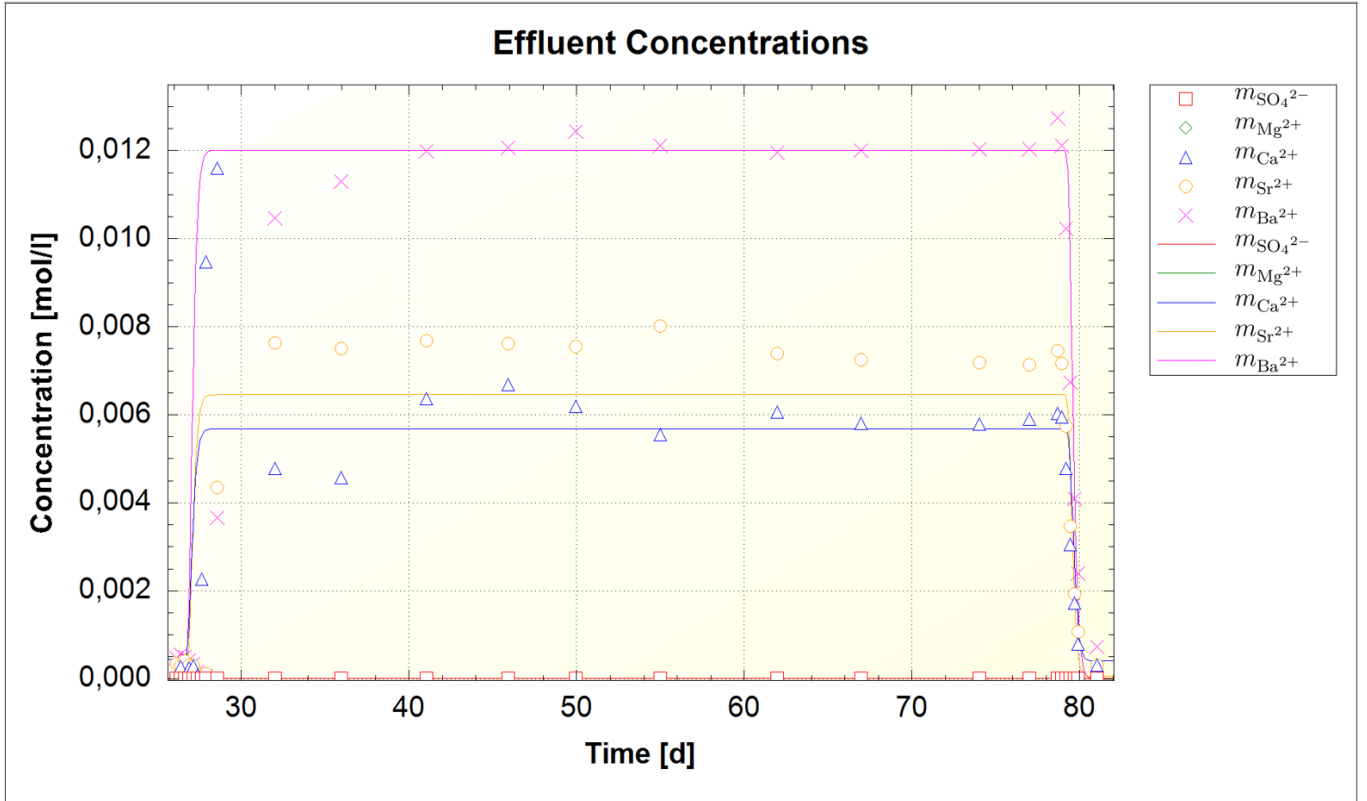


Figure 6.8: Matching of effluent Sr^{2+} concentration in M9 brine 3, with zero witherite ($BaCO_3$) precipitation rate.

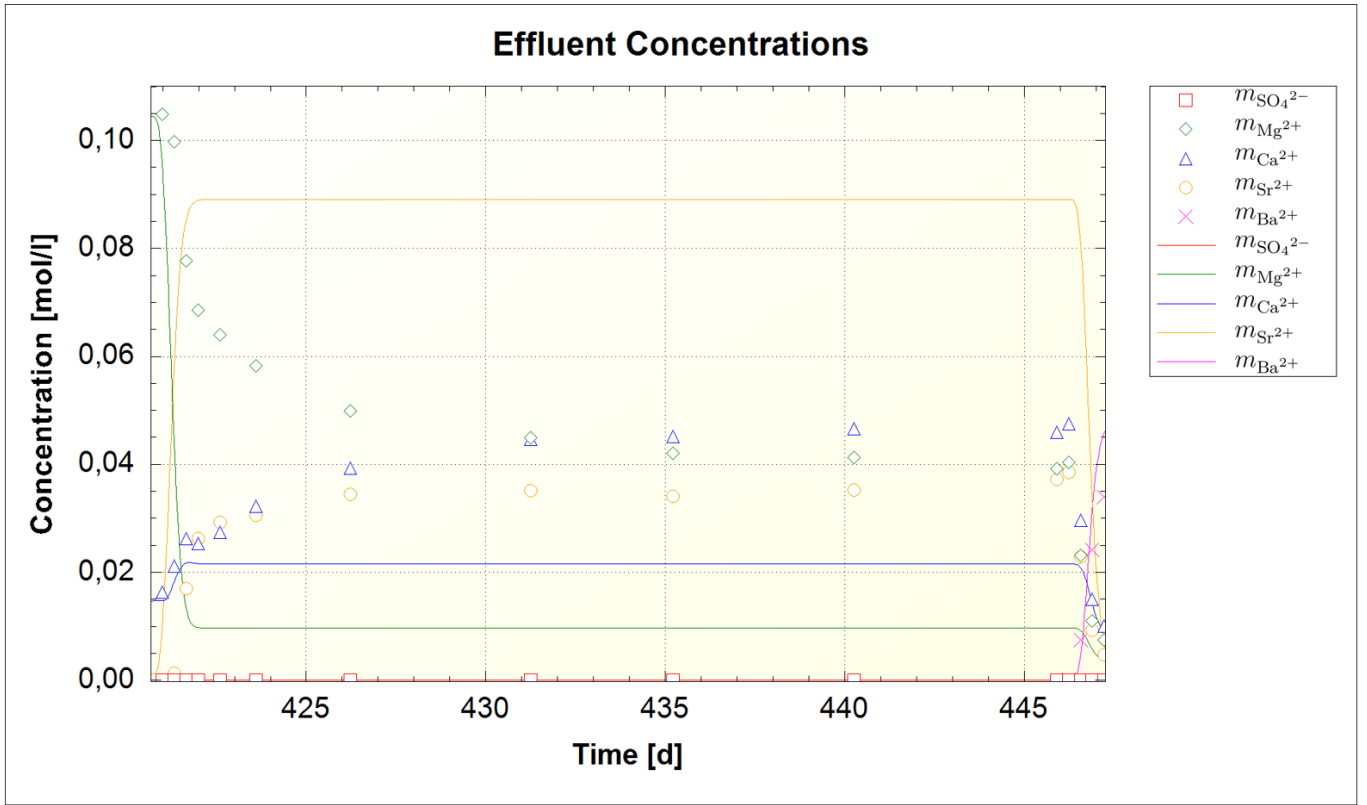


Figure 6.9: The effluent concentrations of M12 from brine 8 sequence, using RF_{str}^{prec} from the M9 matching. Testing RF_{mag}^{dis} over a wide range indicated that precipitation of strontianite (SrCO_3) was the limiting rate.

Discussed earlier, to match Sr^{2+} effluents p_{str} was tuned, but with little success matching both M9 and M12 using the same RF_{str}^{prec} . Therefore, the strontianite parameters p_{str} and q_{str} are set to 2, and 1, respectively, based on findings by Zieba and Nancollas (1994). Furthermore, as discussed in subsection 5.2.4, the reaction rate constant for strontianite was not defined in the literature, unlike the other minerals considered. Consequently, strontianite reaction rate only depends on the constant input parameters and the degree of saturation, whilst the reaction rate of other carbonate minerals are pH dependent.

RF_{str}^{prec} in M12 was tuned to match brine 8, which was the only Sr^{2+} injection sequence in M12. In this sequence, both calcite (CaCO_3) and magnesite (MgCO_3) dissolve, thus matching of magnesite dissolution is required. Dissolution of magnesite occurs in the four last sequences of M12, where three different brines are injected. Thus, its rate has to be adjusted to match all three brines. The first RF_{mag}^{dis} tuning was with strontianite precipitation sequence, followed by witherite (BaCO_3) precipitation, and last the calcite precipitation, i.e. injection of brines 8, 9 and 10. The two latter are discussed related to tuning of witherite and calcite precipitation rates.

During brine 8 injection in M12, calcite (CaCO_3) and magnesite (MgCO_3) dissolve. Consequently, RF_{mag}^{dis} was the only unknown dissolution tuning parameter. The unknown for strontianite (SrCO_3) precipitation in M12 is RF_{str}^{prec} . Consequently, these two reduction factors were adjusted to give the best-fit simulated effluents. First, RF_{str}^{prec} was adjusted to match the Ca^{2+} effluent, followed by

RF_{mag}^{dis} adjustments to match the Mg^{2+} effluent. Thereafter, both RF 's were tuned to match all three effluents. The final matching of this sequence is shown in figure 6.10.

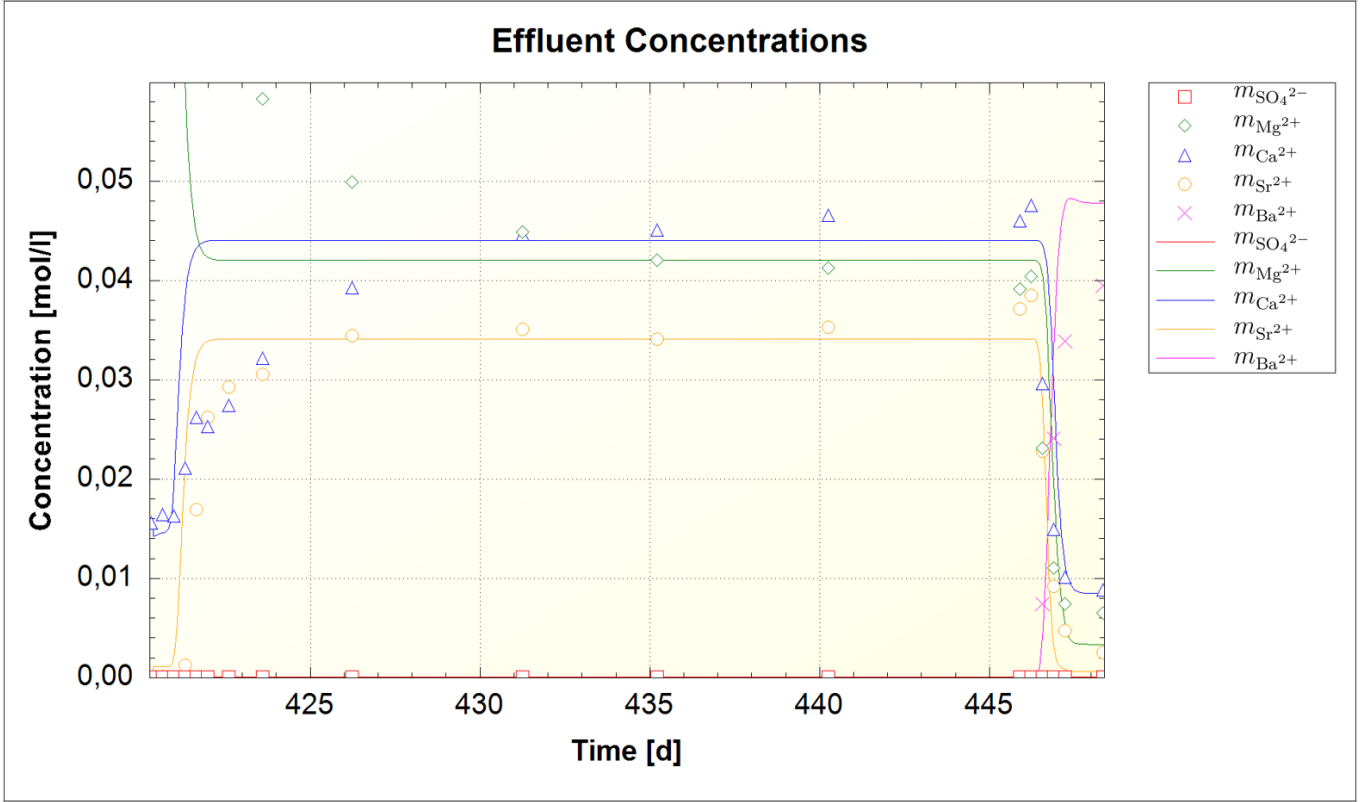


Figure 6.10: Matching of effluents from M12 brine 8 by adjusting RF_{mag}^{dis} and RF_{str}^{prec} .

To determine a more correct RF_{str}^{prec} for core M9, and further tune RF_{mag}^{dis} , the witherite ($BaCO_3$) precipitation rate was needed. In the last reactive flooding sequence of M12, Ba^{2+} was the injected reactive specie. Furthermore, the effluents of Mg^{2+} and Sr^{2+} were very low, and are assumed negligible when determining a first witherite precipitation rate approximation. Therefore the magnesite ($MgCO_3$) and strontianite ($SrCO_3$) dissolution rates are temporarily set to zero. Since the calcite ($CaCO_3$) dissolution rate was determined (see earlier discussion), this rate is assumed to be correct and not further tuned. Consequently, the tuning parameters for witherite are the ones to consider. p_{wit} and q_{wit} are not defined in the literature. Discussed in subsection 5.2.4, these are assumed to be 1 unless they are empirically determined (Palandri and Kharaka, 2004; Bose et al., 2008). Since the parameter tuning is empiric, the p_{wit} is tuned to match the effluent, whilst $q_{wit} = 1$. Similar to the methodology used for tuning of strontianite reaction rate, p_{wit} was tested in the range from 0.5 to 5. For values outside this interval, the rate would become too sensitive to variations in witherite saturation.

The first step of witherite ($BaCO_3$) precipitation parameter tuning was done, as discussed above, by only considering calcite ($CaCO_3$) dissolution. For each p_{wit} a corresponding RF_{wit}^{prec} was found. These sets were tested on the M9 brine 3 sequence and RF_{wit}^{prec} adjusted in the proximity of the M12 sequence 10 tuning value, where the first approximation for strontianite tuning parameters was

used. Using p_{wit} between 0.5 and 1, the witherite precipitation rate was hardly sensitive to changes in influent concentration. This was detected when comparing the simulated effluents from brine 8 in M12 and brine 3 in M9, shown in figures 6.11 and 6.12.

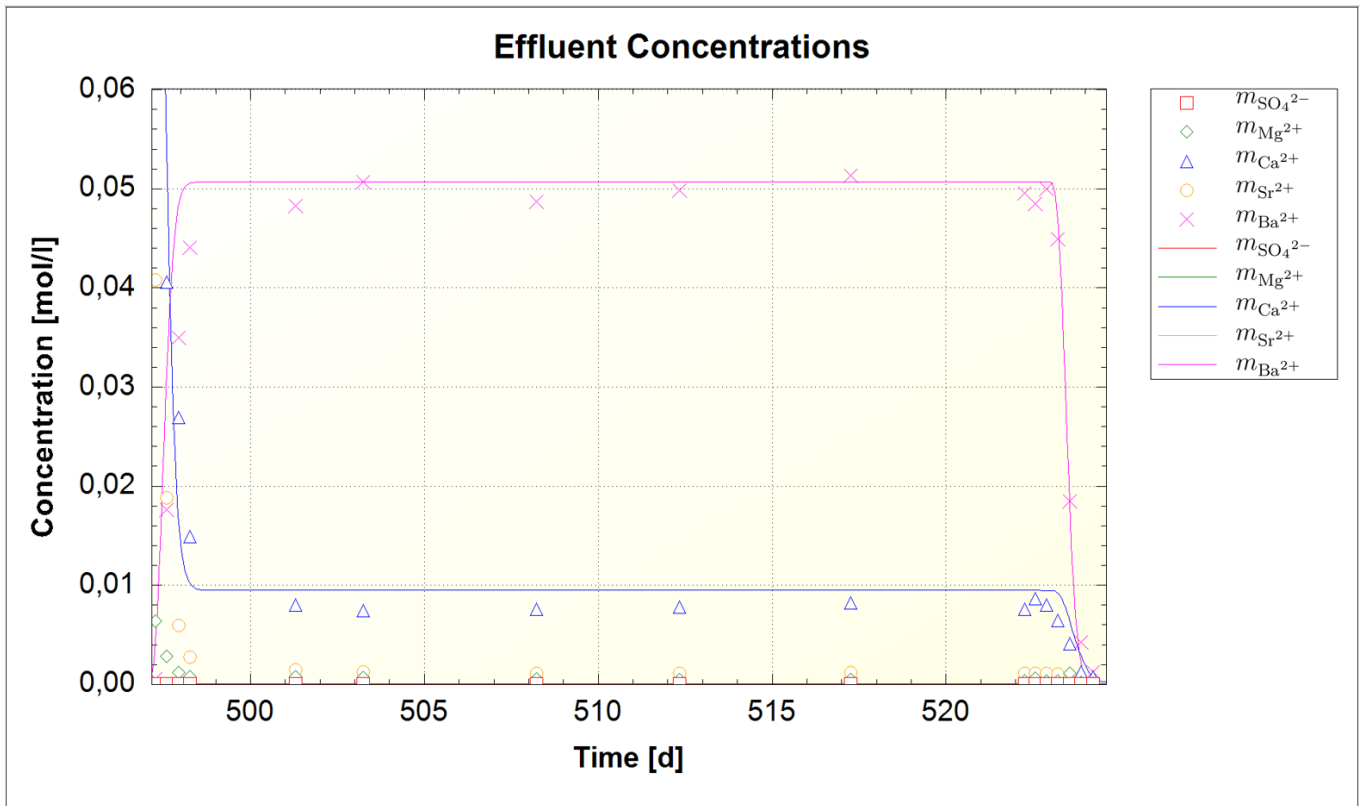


Figure 6.11: Matching the effluents from last injection sequence in M12 using $p_{wit} = 0.5$, demonstrating that by only considering one sequence where a mineral either dissolve or precipitate, the set of tuning parameters that give reasonable results are infinite.

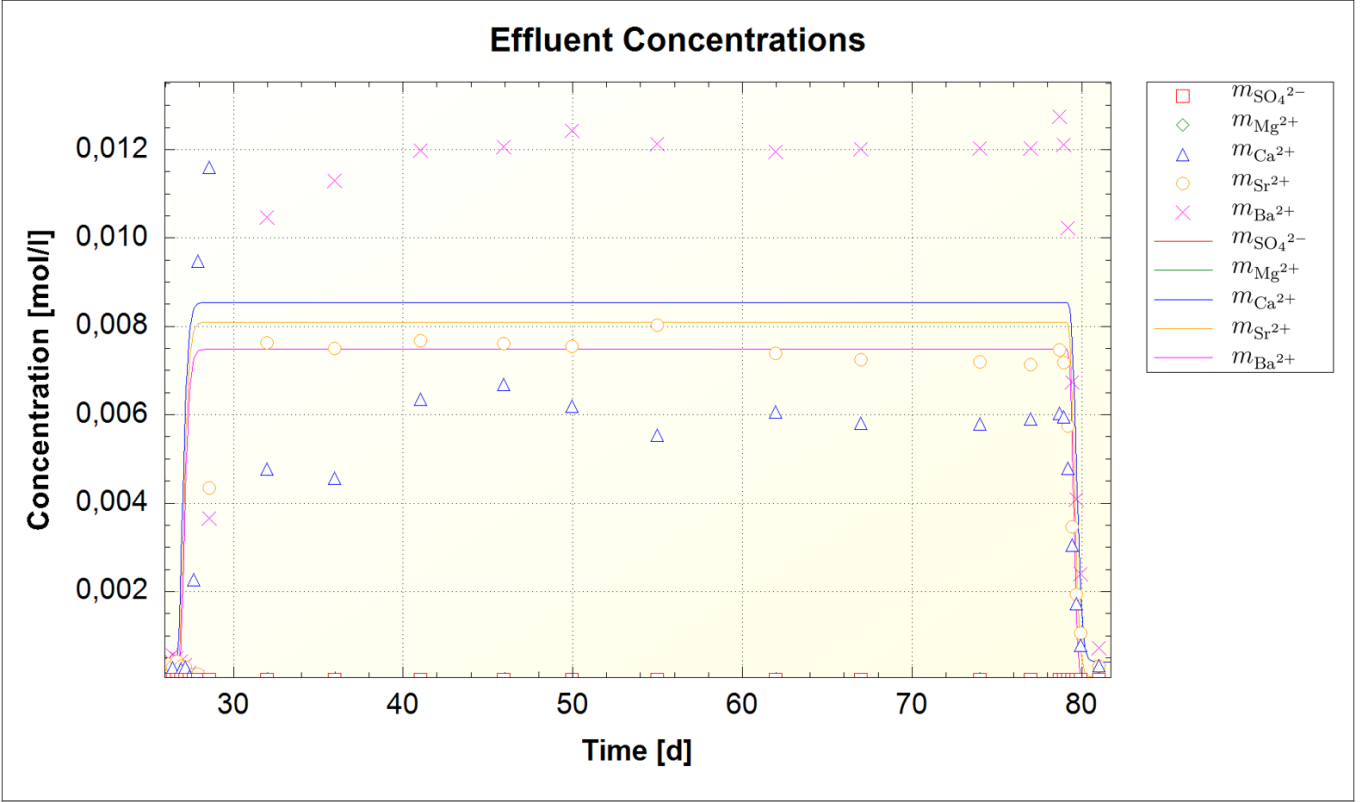


Figure 6.12: Matching M9 effluents using the same tuning parameters for witherite (BaCO_3) as used in figure 6.11, where $p_{wit} = 0.5$, demonstrating that history matching more than one sequence reduce the number tuning parameters sets that give reasonable results.

Moreover, the retention of Ba^{2+} from brine 8 were between $1/3$ and $1/6$ of the injected concentration in M12, compared to no Ba^{2+} retention from brine 3 in M9. Thus, with higher Ba^{2+} concentration, the precipitation rate of witherite (BaCO_3) occur significantly faster, than with lower Ba^{2+} concentration. This is directly related to the degree of witherite super-saturation. To support this, the witherite saturation index (SI_{wit}) from simulations were studied, to evaluate witherite super-saturation. It was seen that in M9 SI_{wit} ranged from 3.1 to 3.5, whilst in M12 it ranged from 3.6 to 4.0. Since the reaction rate equation depends on the saturation ratio (Ω), which is 10 to the power of SI (see equation (3.6)), it is evident that the magnitude of SI_{wit} strongly affects the precipitation rate. To capture the sensitivity of witherite precipitation rate, further tuning was done with $p_{wit} > 1$. Using $p_{wit} = 2$ and adjusting the RF_{wit}^{prec} to match effluents of each core gave too different values. By applying the M12 adjusted RF_{wit}^{prec} in the M9 simulation, the witherite precipitation rate was too high, resulting in too low Ba^{2+} effluent concentration. Further, matching with $p_{wit} = 3$, the M12 adjusted RF_{wit}^{prec} gave a better match with M9 Ba^{2+} effluent. By including the effects of strontianite (SrCO_3) precipitation, the strontianite precipitation rate was taking into consideration. By tuning Rf_{str}^{prec} to better fit the effluent it was recognized that the best-fit for M9 effluents was found using $Rf_{str}^{prec} = 1.0 \cdot 10^{-11}$, $p_{wit} = 3$ and $RF_{wit}^{prec} = 3.0 \cdot 10^{-21}$, shown in figure 6.13.

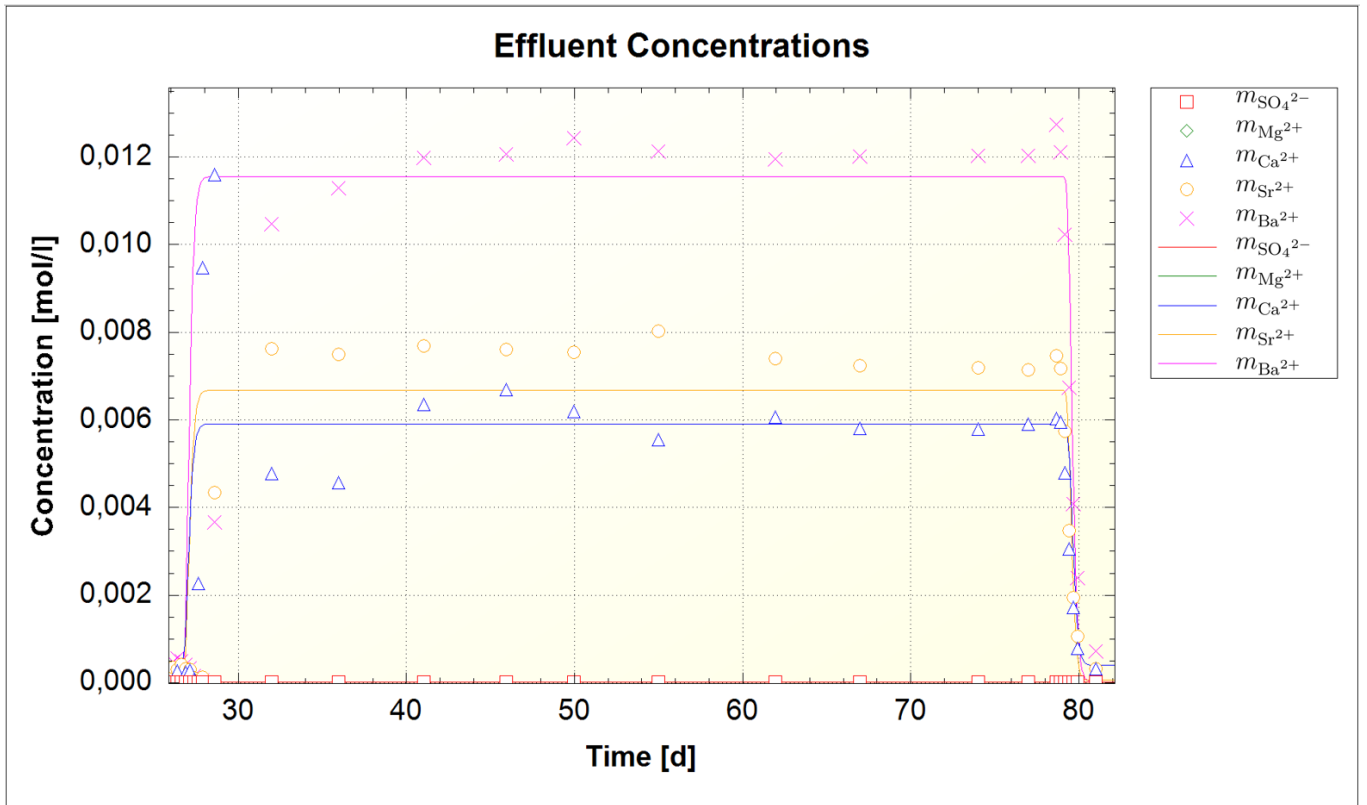


Figure 6.13: M9 matching brine 3, using final tuning parameters for calcite (CaCO_3), strontianite (SrCO_3) and witherite (BaCO_3).

Next, dissolution reaction rates for magnesite (MgCO_3) were now turned back on to investigate how witherite (BaCO_3) parameters fitted effluents from sequence 8 in M12 (demonstrated in figure 6.10), and the three other carbonates dissolved. The magnesite (MgCO_3) precipitation parameters determined from M12 brine 8, shown in figure 6.10, produced suitable effluents.

During brine 10 injection, calcite (CaCO_3) was super-saturated, whilst the three other carbonates (magnesite (MgCO_3), strontianite (SrCO_3) and witherite (BaCO_3)) were under-saturated. Consequently, this sequences require the precipitation parameters for calcite, and dissolution parameters for magnesite, strontianite and witherite. All p and q parameters were defined before this matching sequence, leaving the RF 's for adjustments. In M12, dissolution of both magnesite and strontianite occur in other sequences, whilst calcite precipitation and witherite dissolution only occur in this injection sequence. Consequently, the RF_{mag}^{dis} and RF_{str}^{dis} are first adjusted in the proximity of the matched values for the other relevant sequences, followed by less constricted tuning of RF_{cal}^{prec} and RF_{wit}^{dis} .

The dissolution of magnesite is restricted by the Mg^{2+} matching of M12 sequence 9, shown in figure 6.10. The dissolution rate of strontianite is strongly related to the formation of celestite in M9, thus it is desired to have a sufficiently high strontianite dissolution. This relation is discussed below. The chosen parameters are used to generate the simulated effluents in figure 6.14. The Ba^{2+} does not reach a stable rate, nor was the back-production captured by the model. The Sr^{2+} effluent reaches a stable plateau after approximately 10 days (~ 480 days), but the model was not able

to simulate strontianite (SrCO_3) dissolution with a sufficiently high rate. Nevertheless, the best-fit dissolution reduction factor for strontianite and witherite were $7.0 \cdot 10^{-15}$ and $3.0 \cdot 10^{-21}$, respectively. The best-fit reduction factor for magnesite (MgCO_3) was found to be $2.0 \cdot 10^{-8}$, considering this sequences and the sequences where brine 8 and 9 were injected, demonstrated in figures 6.10 and 6.15.

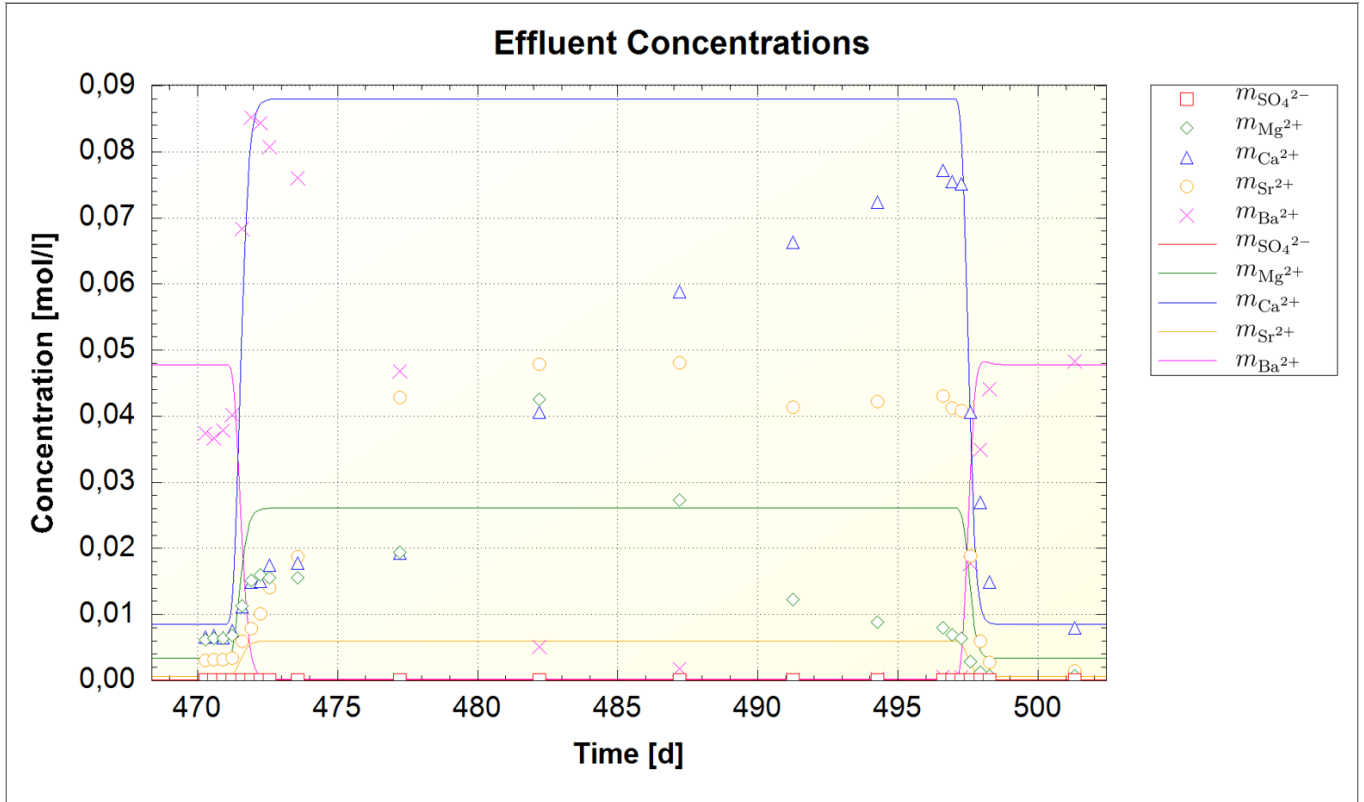


Figure 6.14: M12 matching brine 10, using final tuning parameters for calcite (CaCO_3), magnesite (MgCO_3), strontianite (SrCO_3) and witherite (BaCO_3).

Using the chosen best-fit parameters for precipitation of witherite (BaCO_3), and dissolution of calcite (CaCO_3), magnesite (MgCO_3) and strontianite (SrCO_3), simulation of brine 9 injection sequences, i.e. sequences 8 and 10, are shown in figures 6.15 and 6.16, respectively. It is evident that these figures do not give a perfect match, but it is desired to make a general model, based on a general set of tuning parameters.

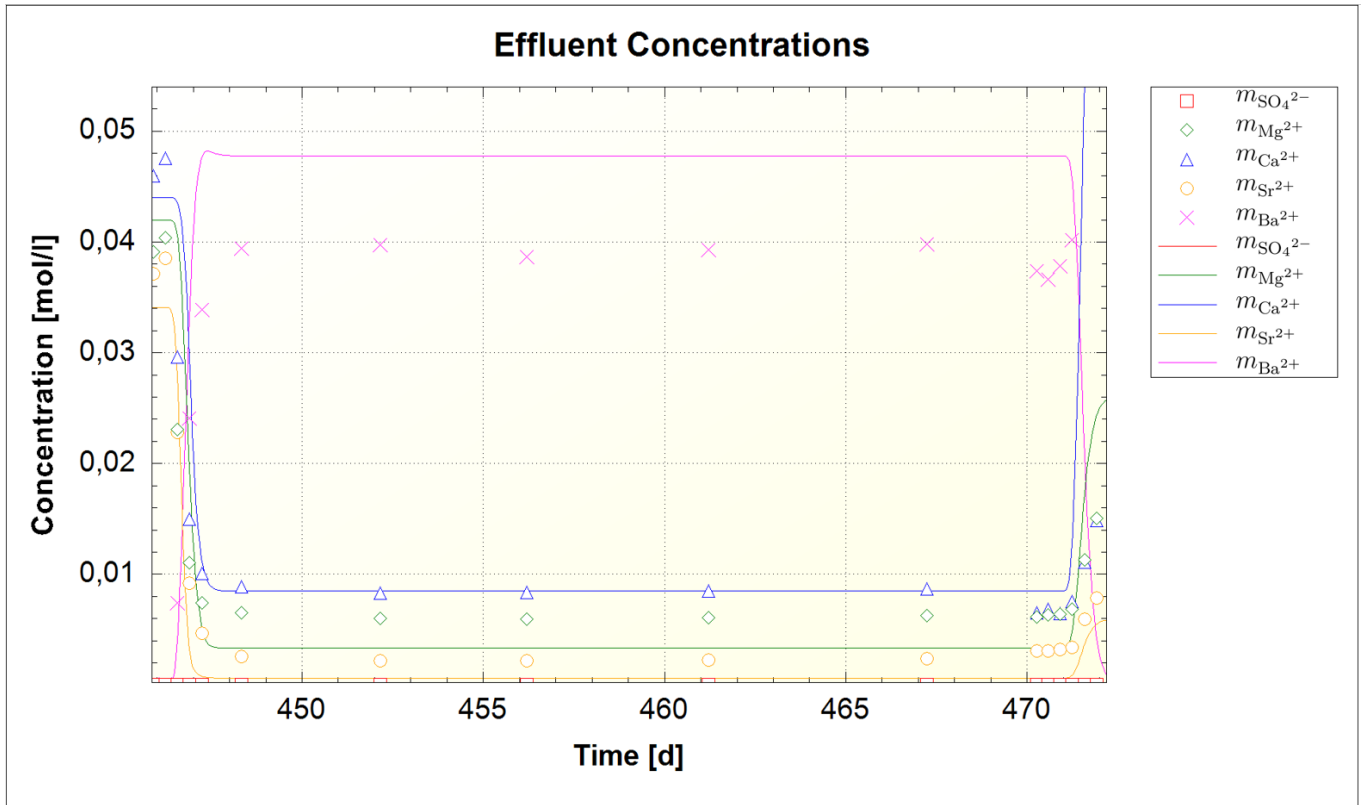


Figure 6.15: M12 matching brine 9 sequence 8, using final tuning parameters for calcite (CaCO_3), magnesite (MgCO_3), strontianite (SrCO_3) and witherite (BaCO_3).

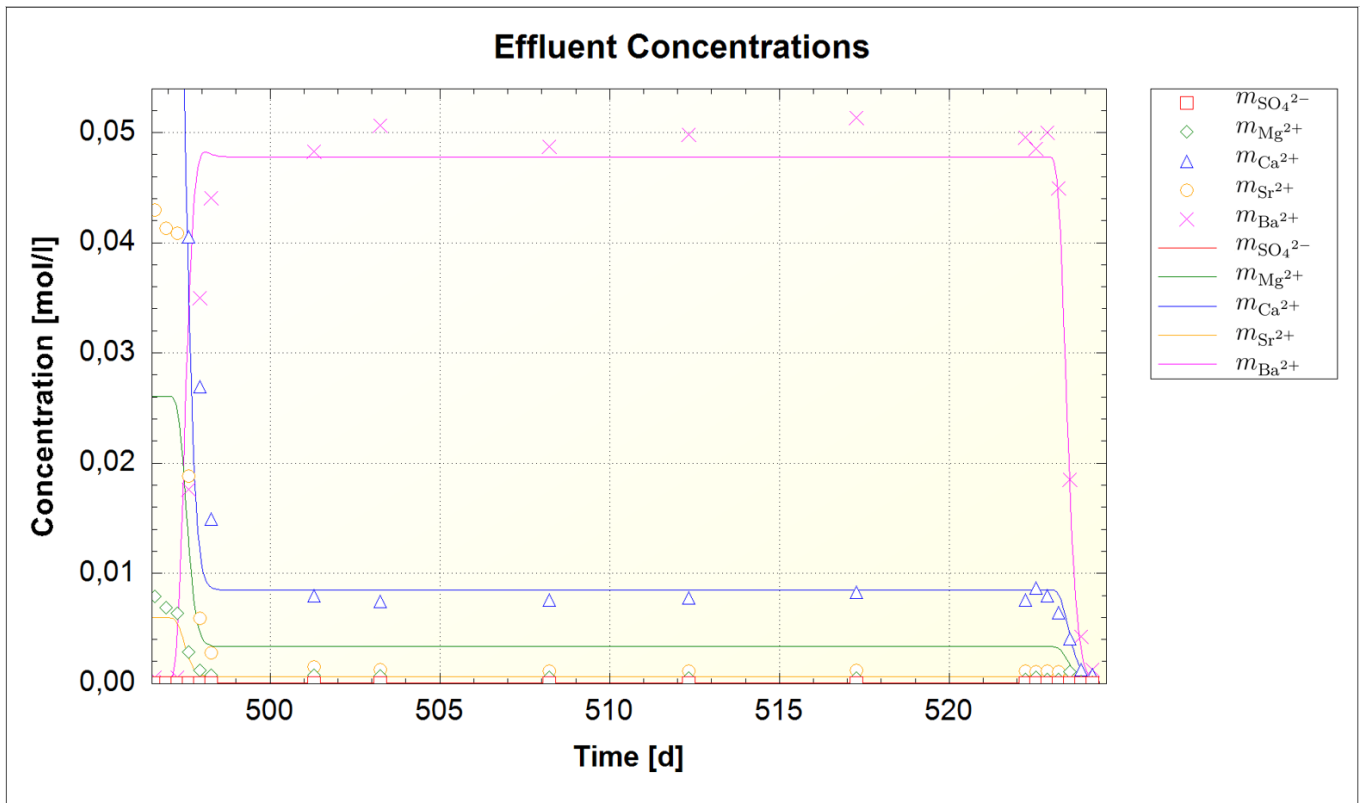
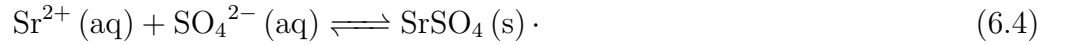
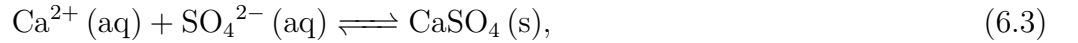
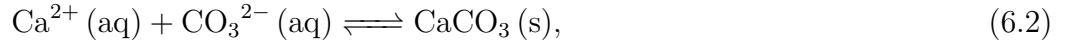
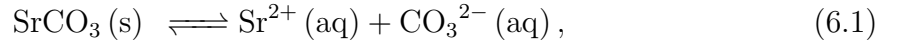


Figure 6.16: M12 matching brine 9 sequence 10, using final tuning parameters for calcite (CaCO_3), magnesite (MgCO_3), strontianite (SrCO_3) and witherite (BaCO_3).

In the last sequence of M9, brine 5 was injected. During this injection sequence, the core was clogged due to permeability reduction caused by the formation of secondary minerals. Demonstrated with the saturation indexes in table 6.1, anhydrite (CaSO_4) become super-saturated, thus tuning of its precipitation parameters have to be performed in this sequence. SEM analysis indicated a Sr-bearing sulphate, shown in figure A.1. In this study, this strontium sulphate is assumed to be explained by celestite (SrSO_4). Based on the assumption that the Mons chalk is of 99 *wt%* pure calcite (CaCO_3), formation of celestite (SrSO_4) could only occur due to dissolution of a secondary strontium bearing carbonate, formed during the brine 3 injection. The challenge with matching these sulphate reaction rates is that there is only one sequence to consider, where the additional effect of permeability reduction forced the experiment to end.

The complex interplay of the ions considered in this sequence are assumed to participate in the following dissolution-precipitation reactions:



It was only one sequence, the last sequence in M9, where precipitation of sulphates could occur, according to simulations. Consequently, only the sulphates net precipitation rate are considered. Discussed in the beginning of this subsection. Henceforth, RF_{anh}^{prec} and RF_{cel}^{prec} are the only adjustable precipitation tuning parameters for sulphate precipitation. To do this the exponents p and q , are retrieved from the literature. Marty et al. (2015) defined $p_{cel} = 0.5$ and $q_{cel} = 2$. Discussed in subsection 6.2.2, are the exponents by default set to 1, unless they are empirically defined (Palandri and Kharaka, 2004; Bose et al., 2008). Consequently, the anhydrite exponents are set to 1. Thus, making RF_{anh}^{prec} and RF_{cel}^{prec} the adjustable sulphate precipitation tuning parameters. Calcite precipitation is also likely to occur during this sequence. Which in turn allow for tuning of RF_{cal}^{prec} in addition to the sulphate RF's.

The rather complex interplay of these ions and minerals are difficult to interpret, e.g. how the precipitation rate of one mineral affects the other reaction rates. A first indication of the effect was done considering Le Châtelier's principle, as discussed in subsection 3.1.1. Based on the chemical reaction equations (6.1) - (6.4), will the following occur: Precipitation of *anhydrite* (CaSO_4) lower both Ca^{2+} and SO_4^{2-} effluents. Thus, reducing both SI_{cal} and SI_{cel} . Precipitation of *calcite* will reduce the Ca^{2+} concentration, and in turn cause dissolution of other carbonates, such as strontianite (SrCO_3) and witherite (BaCO_3), henceforth increase Sr^{2+} and Ba^{2+} concentrations. In turn reducing SI_{anh} , and increasing SI_{cel} . Precipitation of *celestite* (SrSO_4) require dissolution of strontianite (SrCO_3), consequently increasing CO_3^{2-} . Moreover, SO_4^{2-} concentrations are reduced. Therefore increasing SI_{cal} and reducing SI_{anh} .

To evaluate the degree of super-saturation, and how precipitation of calcite (CaCO_3) affects the effluents, precipitation rate of both sulphates were set to zero, and the calcite (CaCO_3) precipitation parameters from brine 10 in M12 were used (see figure 6.14). Simulation indicates that anhydrite (CaSO_4) was more over-saturated than celestite, through the whole core, and calcite (CaCO_3) precipitation causing a gap between SO_4^{2-} and Ca^{2+} effluents, as expected, where SO_4^{2-} was higher than Ca^{2+} . Next, to get a first approximation of RF_{cel}^{prec} , the anhydrite (CaSO_4) precipitation rate remained zero, whilst celestite (SrSO_4) precipitation was tuned. RF_{cel}^{prec} was tested up to 10^3 , without being able to close the *gap* between Ca^{2+} and SO_4^{2-} . Consequently, indicated that celestite precipitation rate is controlled by its saturation state, rather than RF_{cel}^{prec} . Thereafter, the anhydrite (CaSO_4) precipitation rate was turned on, and RF_{anh}^{prec} and RF_{cel}^{prec} were adjusted. Due to the components of anhydrite, its contribution in this sequence might, as discussed earlier, reduce the calcite (CaCO_3) precipitation rate, thus closing the $\text{Ca}^{2+} - \text{SO}_4^{2-}$ gap. SI_{cel} might become negative, as a response to precipitation of SO_4^{2-} . The calcite (CaCO_3) precipitation rate was increased to investigate if the response was as expected. The $\text{Ca}^{2+} - \text{SO}_4^{2-}$ did increase, but the increased strontianite (SrCO_3) dissolution did not increase the celestite (SrSO_4) precipitation rate sufficiently.

After several attempts to match the effluents, the $\text{Ca}^{2+} - \text{SO}_4^{2-}$ gap was not closed by tuning of RF_{anh}^{prec} , RF_{cal}^{prec} and RF_{cel}^{prec} , nor was the Sr^{2+} effluent matched. Consequently, the chosen RF_{cal}^{prec} was taken for the brine 10 M12 sequence. Further, RF_{cel}^{prec} and RF_{anh}^{prec} were not defined. To demonstrate how poorly the matching was for this sequence one of the several test simulations performed are shown in figure 6.17, where $RF_{anh}^{prec} = 10^{-9}$, $RF_{cal}^{prec} = 6.0 \cdot 10^{-5}$ and $RF_{cel}^{prec} = 1$ were used.

Seen in figure 6.17, the produced Sr^{2+} concentration equal the difference of produced SO_4^{2-} and Ca^{2+} . This is a results of the substitution-like assumption which is defined in the steady-state partial differential equations defining the system, i.e. equations (3.46) - (3.52).

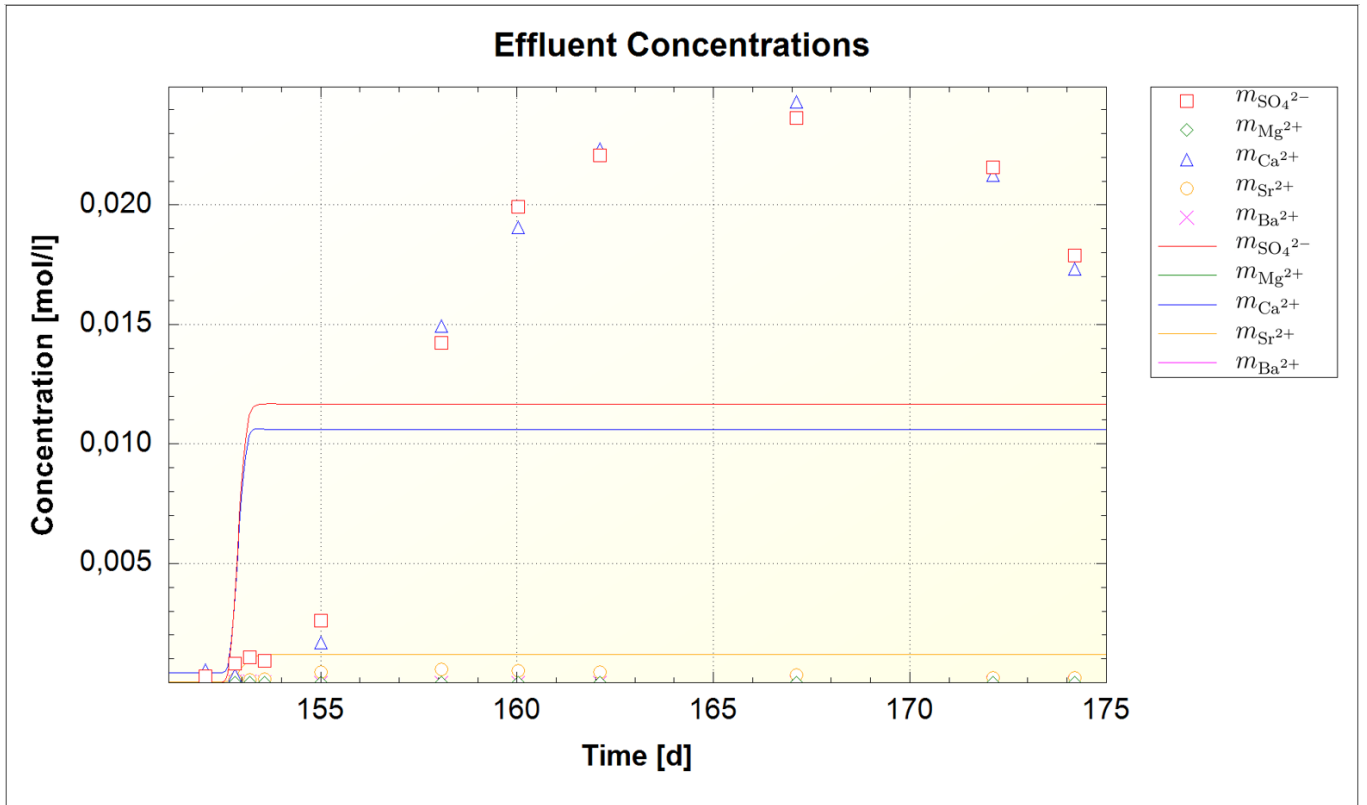


Figure 6.17: Demonstrating one of the several simulations used to capture the geochemical alteration from brine 5 flooding of M9, which did not give a great match.

	Anhydrite	Calcite	Celestite	Magnesite	Strontianite	Witherite
p	1	1	0.5	2	2	3
q	1	1	2	2	1	1
RF^{dis}	ND	$2.7 \cdot 10^{-6}$	ND	$2.0 \cdot 10^{-8}$	$1.0 \cdot 10^{-11}$ * $7.0 \cdot 10^{-15}$ **	$3.0 \cdot 10^{-21}$
RF^{prec}	ND	$6.0 \cdot 10^{-5}$	ND	$8.0 \cdot 10^{-3}$	$5.0 \cdot 10^{-10}$	$5.0 \cdot 10^{-8}$

* M9 tuning parameter

** M12 tuning parameter

ND means not defined

Table 6.2: Tuning parameters summarized.

When only considering one sequence where a mineral either dissolve or precipitate, there are infinitely many sets of parameters that will make the model match experimental results. Consequently, to tune the parameters to give better history matching and be more predictive, multiple experiments with various injected concentrations are required. Demonstrated with figures 6.11 and 6.16, different sets of witherite tuning parameters give a decent match considering one Ba^{2+} concentration, but when the Ba^{2+} is changed and the effluent behaves differently, the effect of the parameters become more evident. Demonstrated in figures 6.11 and 6.12, the simulated behaviour of witherite precipitation is strongly dependent of its degree of saturation.

6.3 Full Experiment Simulations

The defined tuning parameters, summarized in table 6.2, were used to run full flooding experiment simulations for each core. Similar to the experimental presentation of the effluent concentrations in figures 2.1 - 2.4, the final simulations are presented in figures 6.18 - 6.21. In the final presentation, the sum of all measured divalent cations and sum of all simulated divalent cations, denoted by $\sum m_{Me^{2+}}$ and presented as marked points and a curve, respectively, are added. Moreover, the final simulated distribution of the relevant components are compared with the geochemical analysis distribution (presented in tables 2.3 and 2.4) in figures 6.22 - 6.30, and discussed in subsection 6.3.1.

To not have too much information in the final simulation plots, the injected concentrations are not printed in the plots. The injected concentrations can be read from the re-presentation of table 2.1 below and in figure captions.

Brine	1	2	3	4	5	6	7	8	9	10	MgCl ₂
Ions [<i>mol/L</i>]											
Cl ⁻	0.657	0.585	0.633	0.561	0.561	0.561	0.465	0.465	0.525	0.465	0.438
Na ⁺	0.657	0.633	0.585	0.561	0.561	0.513	0.225	0.225	0.405	0.225	
SO ₄ ²⁻		0.024		0.024	0.024						
Mg ²⁺				0.024		0.024	0.120				0.219
Ca ²⁺					0.024					0.120	
Sr ²⁺			0.012					0.120			
Ba ²⁺			0.012						0.060		
Flooding sequence in..											
MO10											1
M9	1,3		2		4						
M12	1,3	2		4		5	6	7	8,10	9	

Table 6.3: Composition of brines used in experiments by Korsnes and Madland (2017) (Brine 1-10), and Andersen et al. (2018) (MgCl-brine).

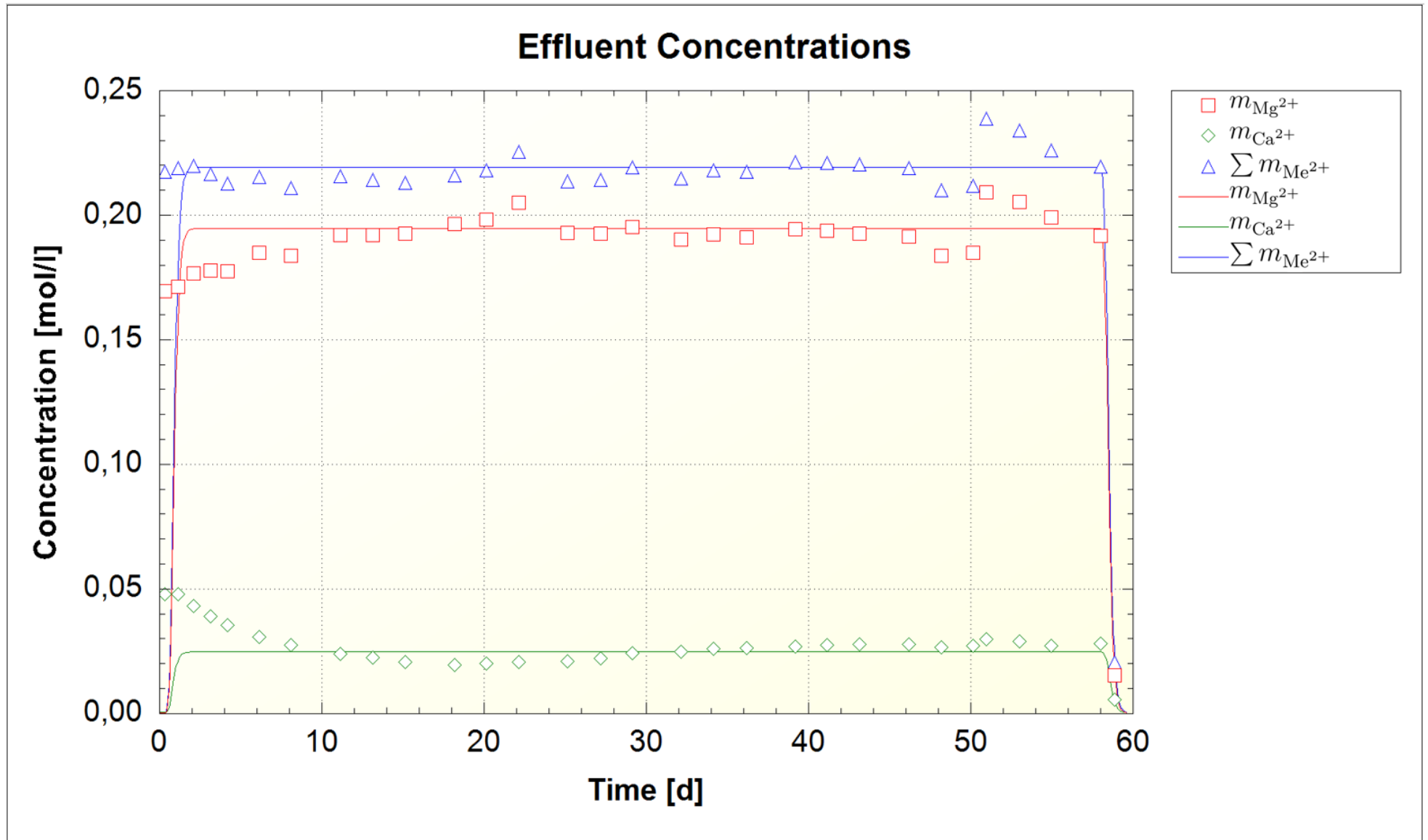


Figure 6.18: Final simulated results in the MO10 core. The tuning parameters used are listed in table 6.2. The IC measured effluents are presented as data points, whilst the lines represent the simulated effluent. $\sum m_{\text{Me}^{2+}}$ symbolise the sum of all divalent cations, for both measured with IC and simulated. Results indicate substitution-like dissolution-precipitation reactions of calcite (CaCO_3) and magnesite (MgCO_3) in this core. Mg^{2+} was injected at 0.219 mol/litre.

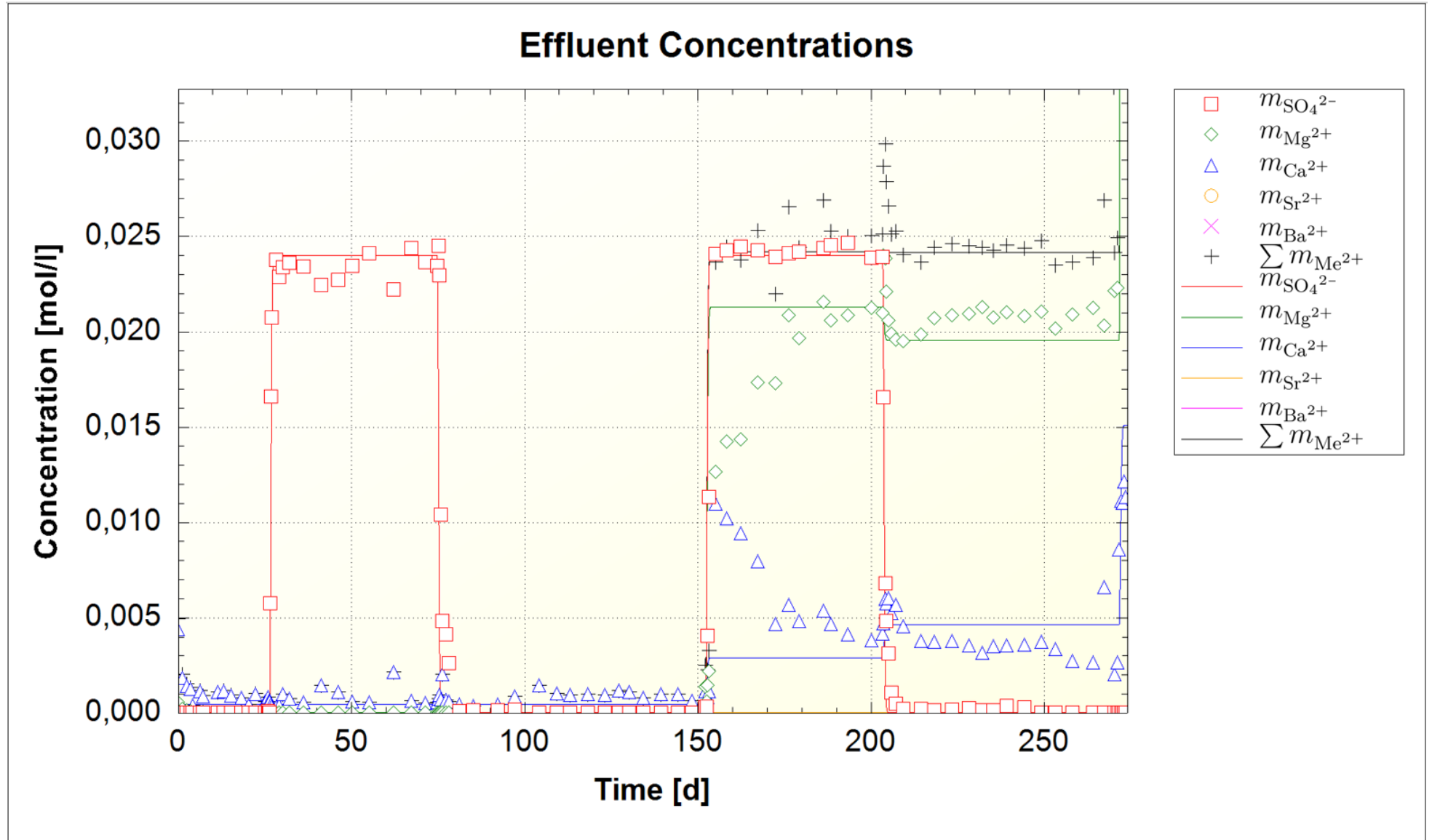


Figure 6.19: Final simulated results in the 5 first sequences of the M12 core. The tuning parameters used are listed in table 6.2. The IC measured effluents are presented as data points, whilst the lines represent the simulated effluent. $\sum m_{\text{Me}^{2+}}$ symbolise the sum of all divalent cations, for both measured with IC and simulated. During the three first injection sequences, no precipitation occurred, where brine 1 and 2 were injected. From 150 to 200 days brine 4 was injected, where $m_{\text{Mg}^{2+}} = m_{\text{SO}_4^{2-}} = 0.024 \text{ mol/litre}$. From 200 to 270 days brine 6, with $m_{\text{Mg}^{2+}} = 0.024 \text{ mol/litre}$, was injected.

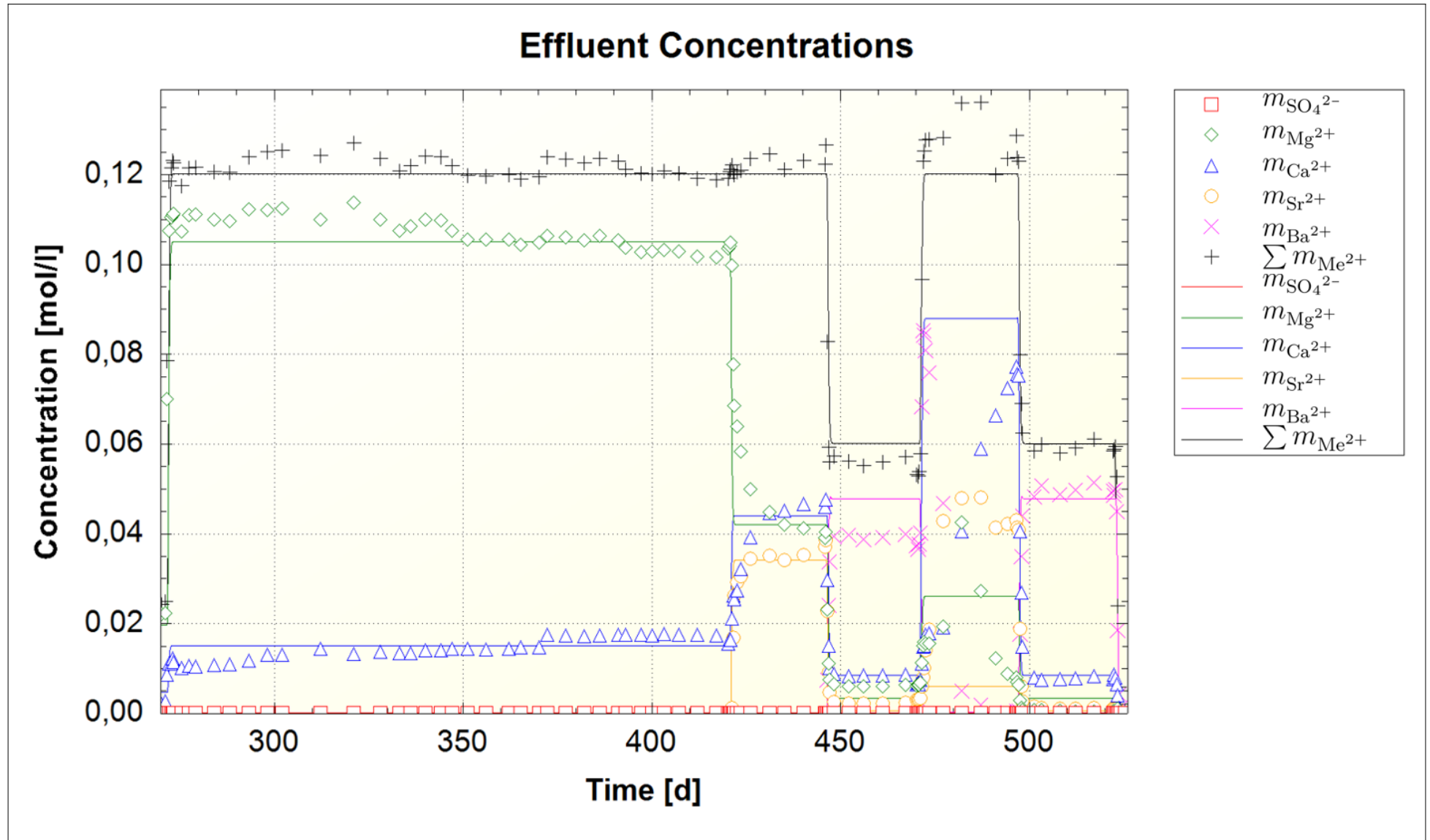


Figure 6.20: Final simulated results in the last 5 sequences of the M12 core. The tuning parameters used are listed in table 6.2. The IC measured effluents are presented as data points, whilst the lines represent the simulated effluent. $\sum m_{\text{Me}^{2+}}$ symbolise the sum of all divalent cations, for both measured with IC and simulated. From 270 to 420 days the injected brine 7 had $m_{\text{Mg}^{2+}} = 0.120 \text{ mol/litre}$. From 420 to 445 day brine 8 with $m_{\text{Sr}^{2+}} = 0.120 \text{ mol/litre}$. During the period 445 to 470 days, and 496 to 522 day, brine 9 with $m_{\text{Ba}^{2+}} = 0.060 \text{ mol/litre}$ was injected. From 470 to 496 days brine 10 with $m_{\text{Ca}^{2+}} = 0.120 \text{ mol/litre}$ was injected.

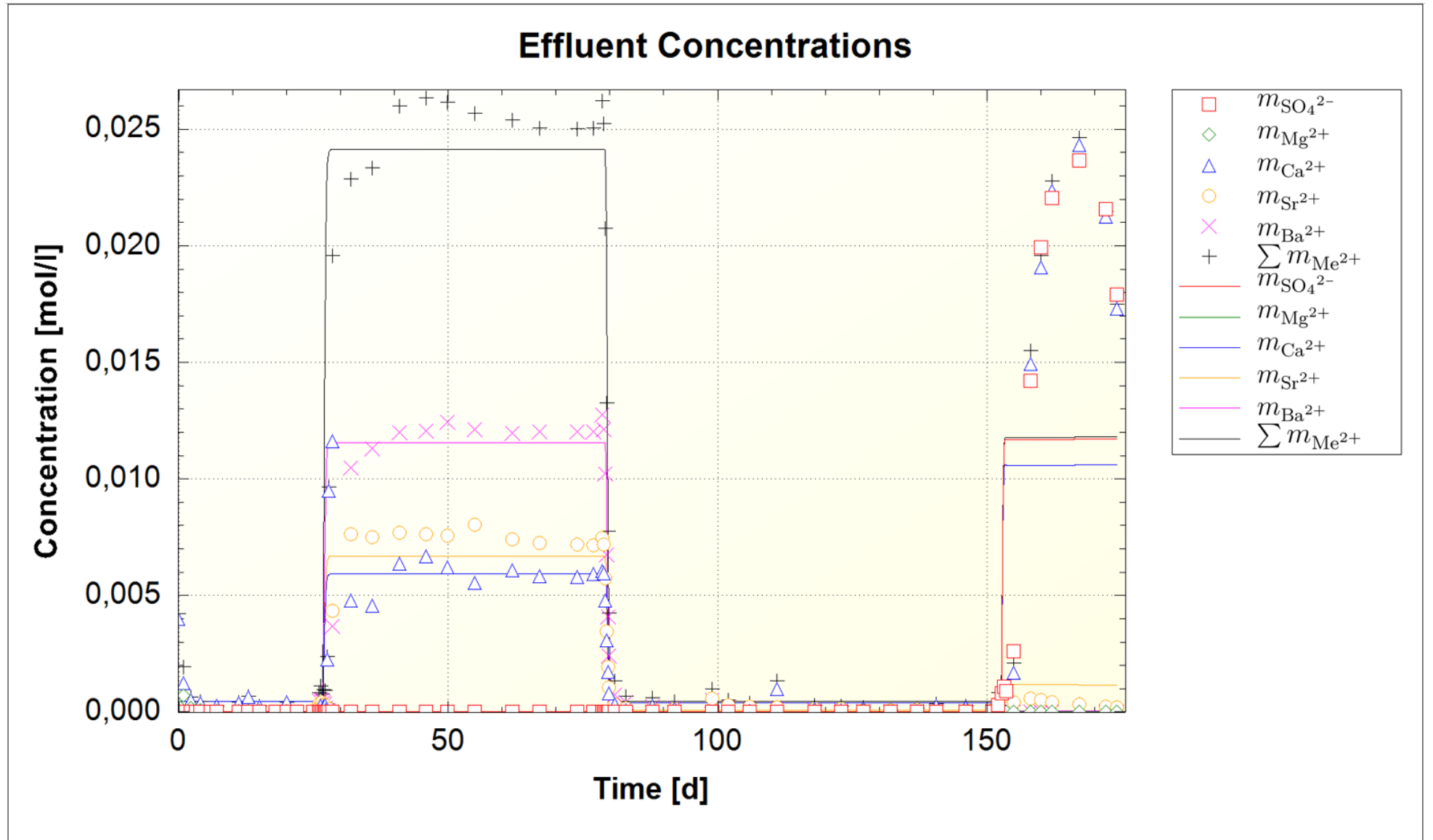


Figure 6.21: Final simulated results in the M9 core. The tuning parameters used are listed in table 6.2. The IC measured effluents are presented as data points, whilst the lines represent the simulated effluent. $\sum m_{\text{Me}^{2+}}$ symbolise the sum of all divalent cations, for both measured with IC and simulated. From the beginning to 26 days, and 78 to 152 days, brine 1 was injected. From 26 to 78 days brine 3, where $m_{\text{Sr}^{2+}} = m_{\text{Ba}^{2+}} = 0.012 \text{ mol/litre}$, was injected. From 152 days until the core clogged, brine 5 was injected. The concentrations in brine 5 were $m_{\text{Ca}^{2+}} = m_{\text{SO}_4^{2-}} = 0.024 \text{ mol/litre}$.

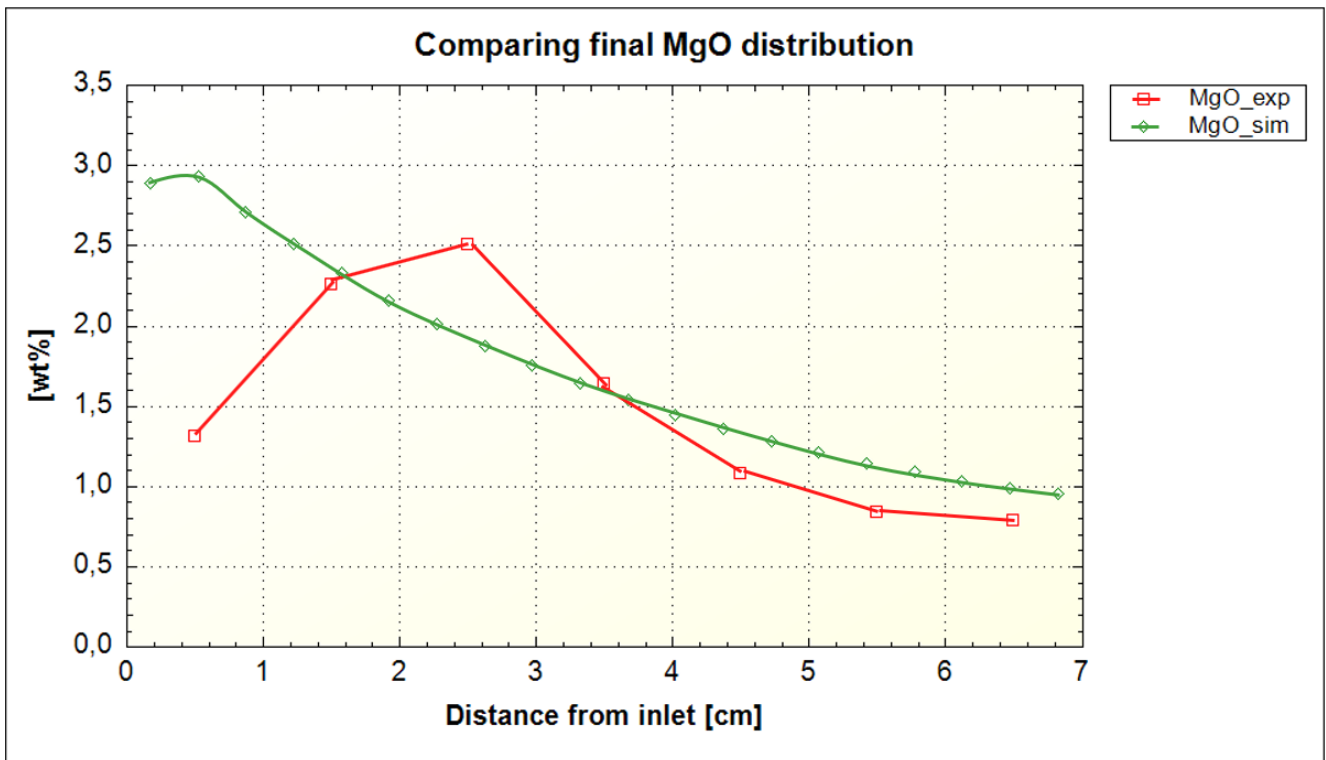


Figure 6.22: Comparing the final distribution of MgO from geochemical analysis (*MgO_exp*) and simulation (*MgO_sim*) of MO10. Simulation does not capture the gradual increasing MgO content in the three first slices. Simulation indicate a higher total content of MgO compared to geochemical analysis.

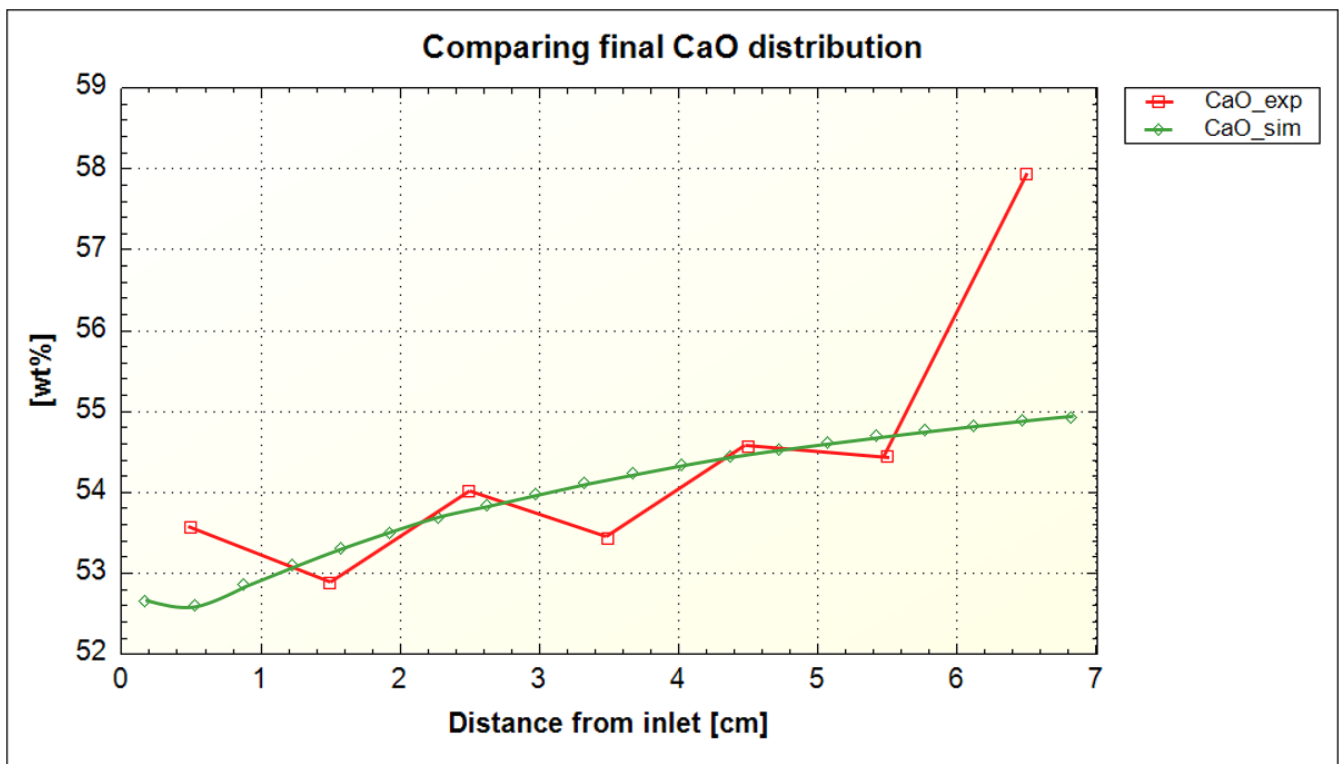


Figure 6.23: Comparing the final distribution of CaO from geochemical analysis (*CaO_exp*) and simulation (*CaO_sim*) of MO10. Since the MO10 core is assumed to initially consist of pure calcite (CaCO_3) the model compute a good dissolution rate and distribution of calcite, resulting in a good CaO match in the 6 first slices.

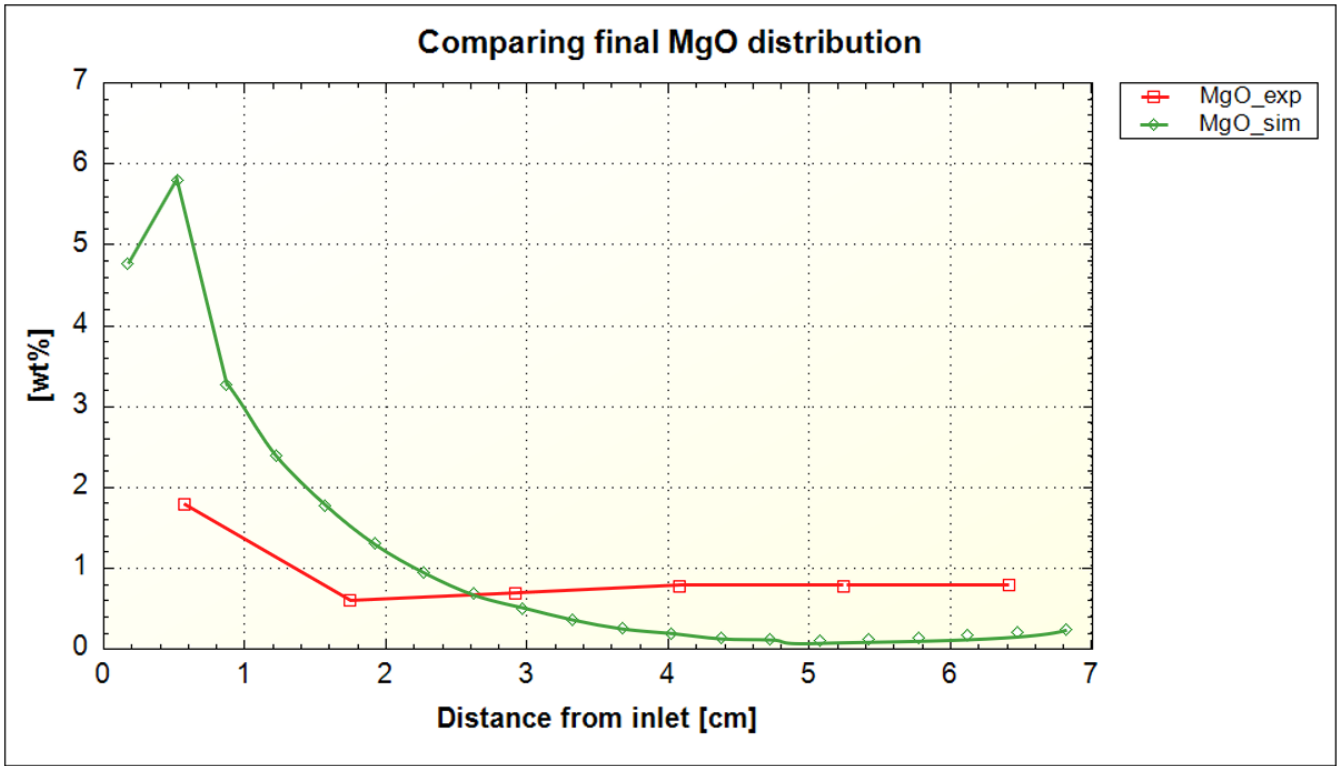


Figure 6.24: Comparing the final distribution of MgO from geochemical analysis (MgO_{exp}) and simulation (MgO_{sim}) of M12. The experimental distribution of MgO was more evenly distributed than the simulated. The difference might be a result of the poorly matched strontianite ($SrCO_3$) precipitation behaviour, demonstrated in figure 6.27.

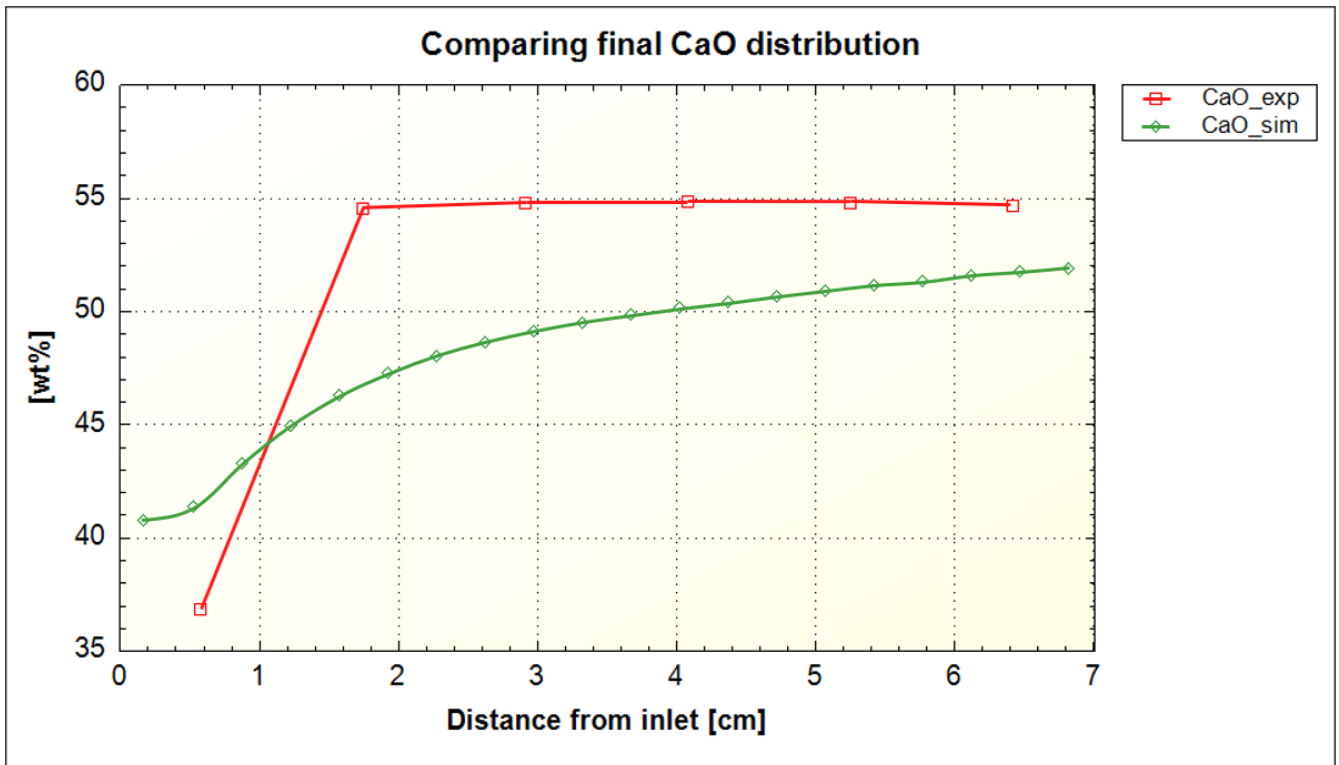


Figure 6.25: Comparing the final distribution of CaO from geochemical analysis (CaO_{exp}) and simulation (CaO_{sim}) of M12. The CaO distribution trend is well captured by the model. The deviation might be related to the poor strontianite matching, seen in figure 6.27.

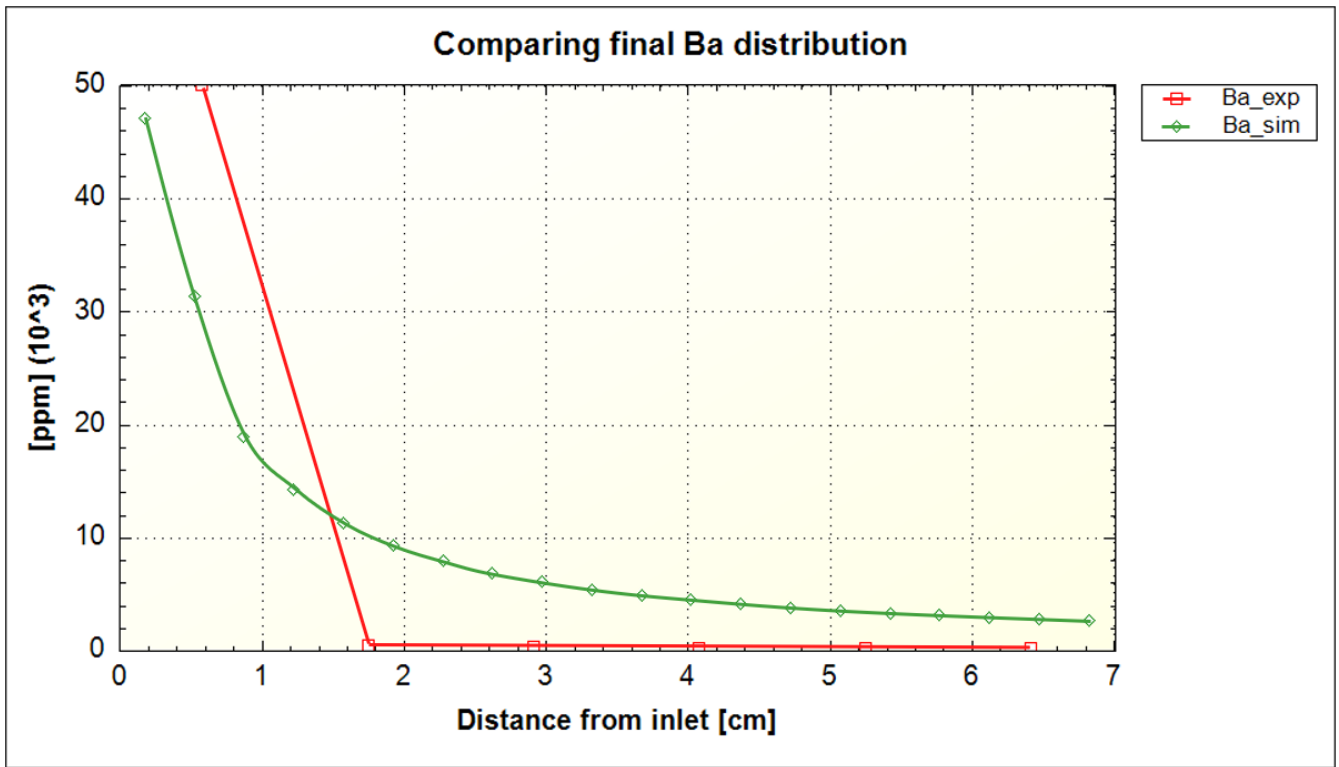


Figure 6.26: Comparing the final distribution of Ba from geochemical analysis (Ba_{exp}) and simulation (Ba_{sim}) of M12. The distribution trend is captured, but the potentially extreme inlet concentration and close to zero in the latter slices are not reproduced by the simulation. The actual inlet Ba^{2+} concentration might be higher, but is placed at 50 000 ppm. See discussion in subsection 6.3.1 for further details.

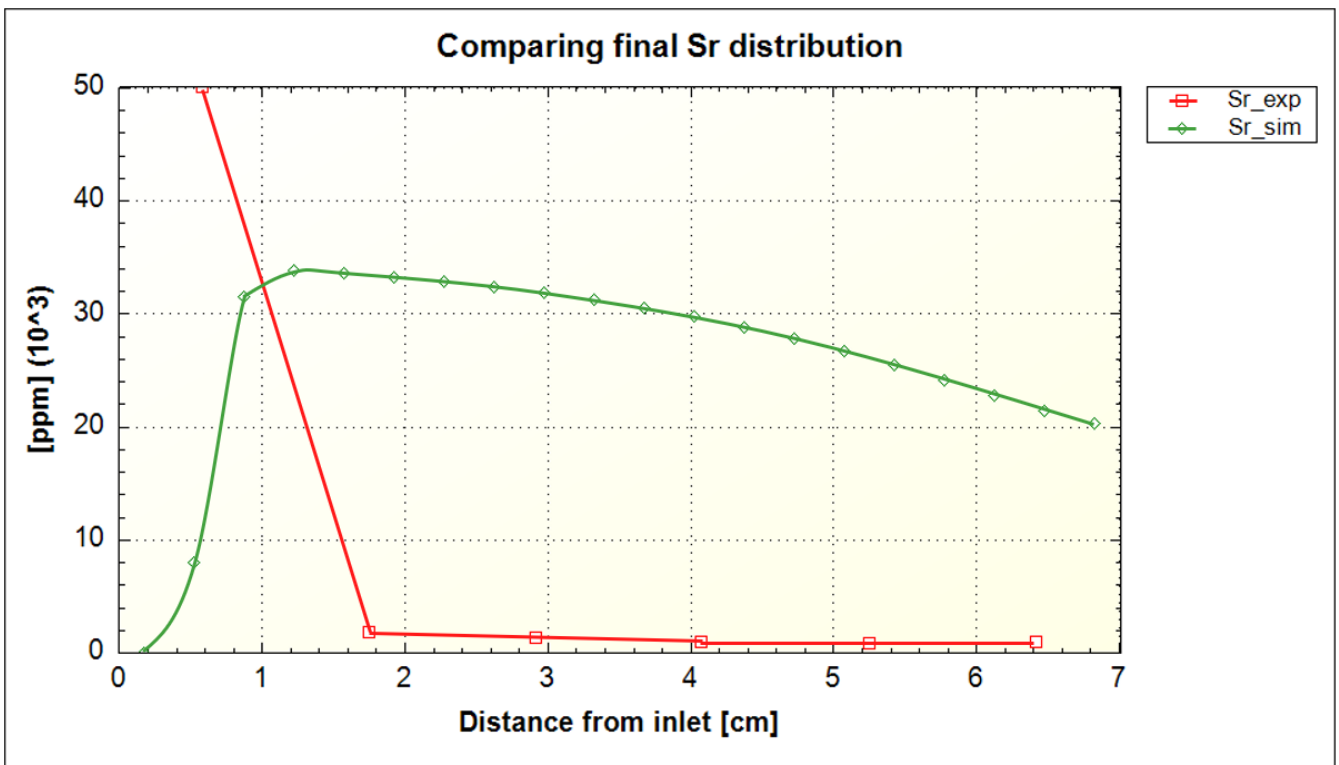


Figure 6.27: Comparing the final distribution of Sr from geochemical analysis (Sr_{exp}) and simulation (Sr_{sim}) of M12. The simulated strontium distribution give a poor fit with the geochemically defined distribution.

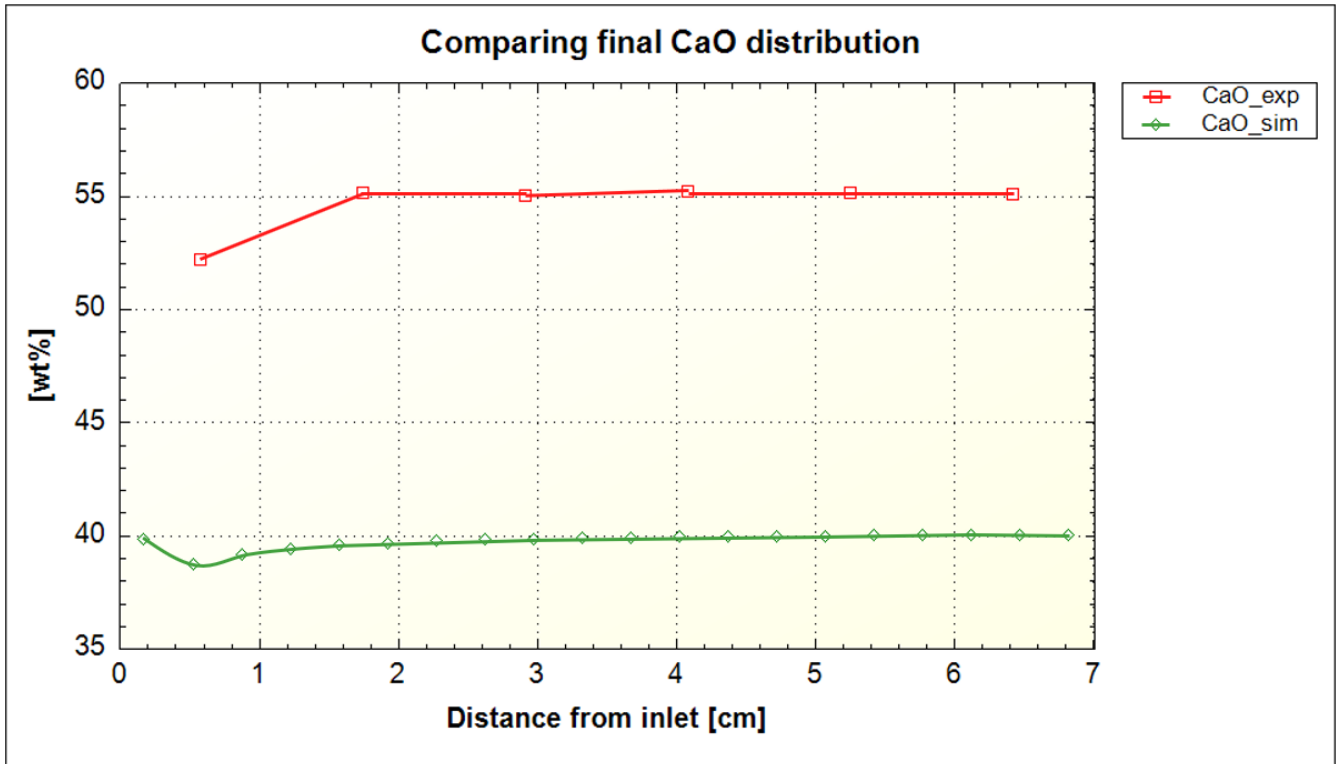


Figure 6.28: Comparing the final distribution of CaO from geochemical analysis (*CaO_exp*) and simulation (*CaO_sim*) of M9. The general under-prediction of CaO content is related to the over-prediction of Sr content, demonstrated with figure 6.30.

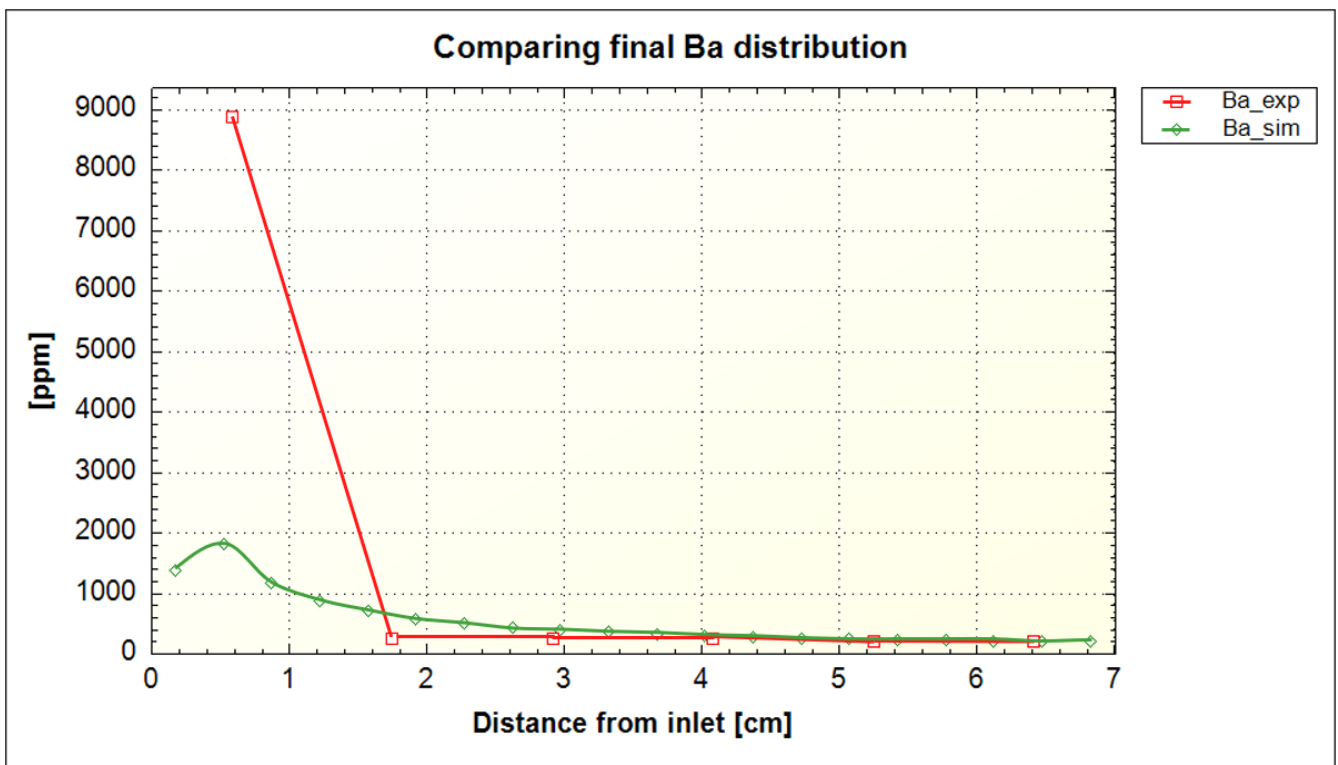


Figure 6.29: Comparing the final distribution of Ba from geochemical analysis (*Ba_exp*) and simulation (*Ba_sim*) of M9. The computed inlet concentration of Ba is significantly lower than the experimental. Under-prediction is related to the too high strontianite (SrCO_3) precipitation, demonstrated in figure 6.30.

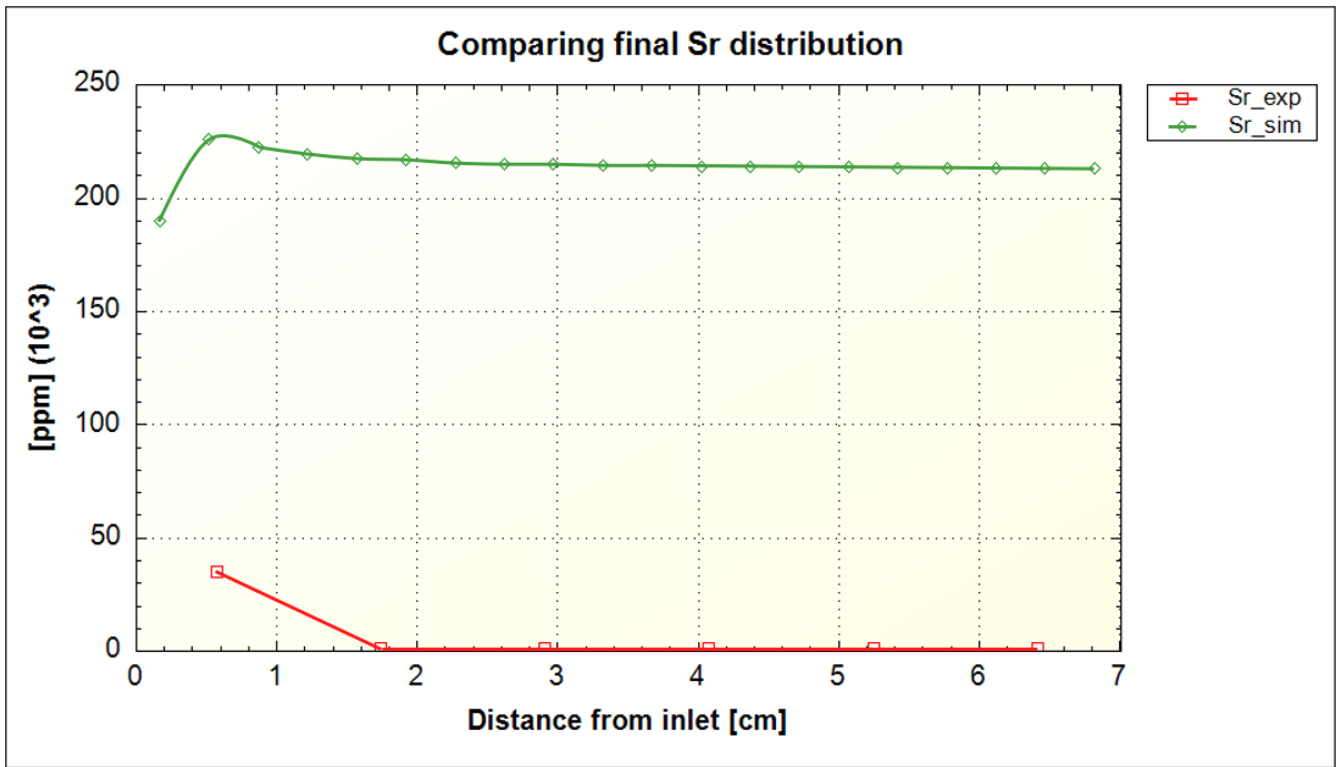


Figure 6.30: Comparing the final distribution of Sr from geochemical analysis (Sr_{exp}) and simulation (Sr_{sim}) of M9.

6.3.1 Mineral Distribution

The MO10 core was flooded with one brine, where calcite (CaCO_3) dissolved and magnesite (MgCO_3) precipitated. Thus, the final mineral distribution only depended on the advection-dispersion-reaction (ADR) equations of two species. The mineral distribution of magnesite was used to tune the reaction rate parameters for both calcite and magnesite, consequently producing a good match for both effluents and final mineral distribution. This tuning resulted in a good match of the mineral distribution. The early spike of MgO content in figure 6.22, was possible to shift more towards the center of the core. This spike-shift would reduce the reaction rate, thus less computed MgO content. For further details, see discussion in subsection 6.2.2 for further details. The CaO experimentally measured content fluctuates around the computed, thus indicating a good match, shown in figure 6.23.

It is worth noting that the inlet concentration of both barium (Ba) and strontium (Sr) were higher than 50 000 ppm (see table 2.4), but the upper detection limit of the ICP-MS is 50 000 ppm. Thus, the plotted inlet concentration of both components are 50 000 ppm. In M12 both the Ba and CaO distribution trends are captured, shown in figures 6.26 and 6.25, respectively. The (potentially) extreme inlet and zero content in the following segments was not reproduced in M12. Similar to the final barium distribution in M12, is the simulated barium content near the inlet of M9 too low. Demonstrated in figure 6.29. Consequently, indicating that the exponent tuning parameters maybe should have been higher, making witherite precipitation rate more sensitive to its degree of saturation.

The strontianite reaction rate constant was not defined in the literature, consequently introducing great uncertainty to the computed dissolving and precipitating behaviour. Illustrated in figures 6.27 and 6.30, the final computed distribution of strontium is the opposite of experimental and too high strontium content in the latter slices. The experimental distribution of strontium indicates that it behaves similar to barium, i.e. more sensitive to its saturation. The error in strontianite precipitating behaviour in M9, may have caused the mismatch of MgO distribution in figure 6.24.

6.3.2 Dissolution-Precipitation Behaviour

In this thesis, it is assumed that dissolution and precipitation reactions occurring are substitution-like reactions, meaning that an equal number of mols are dissolved and precipitated. Such that:

$$\dot{r}_{\text{Mg}^{2+}} + \dot{r}_{\text{Ca}^{2+}} + \dot{r}_{\text{Ba}^{2+}} + \dot{r}_{\text{Sr}^{2+}} = 0. \quad (6.5)$$

To exemplify this, considering the dissolution and precipitation in MgCl_2 flooding of MO10, demonstrated in figure 6.18, the number of magnesium mols that are retained due to magnesite (MgCO_3) formation, equals the number of mols calcium that are produced due to calcite (CaCO_3) dissolution. Considering steady-state reactions in MO10, where dissolution of calcite and precipitation of magnesite are the only reactions considered, the partial differential equations ((3.37) and (3.38)) defining the system give:

$$\dot{r}_{\text{Ca}^{2+}} = -\dot{r}_{\text{Mg}^{2+}}. \quad (6.6)$$

It was postulated by Andersen et al. (2018) that magnesite (MgCO_3) precipitation and calcite (CaCO_3) dissolution are substitution processes. This corresponds with findings of herein. Demonstrated in figure 6.18, the simulated $\sum m_{\text{Me}^{2+}}$ was computed equal to the injected concentration of Mg^{2+} , and the measured effluent fluctuates around this computed simulated value. Consequently, this simulation supports the assumption that the dissolution-precipitation reactions of calcite (CaCO_3) and magnesite (MgCO_3) in MO10 are substitution-like. Moreover, both brine 6 (last sequence in figure 6.19) and 7 (first sequence in figure 6.20) injection in M12, also give the same results as the MgCl_2 injection of MO10. In these brines the injected Mg^{2+} concentrations are approximately $1/9$ and $1/2$ of the MO10 Mg^{2+} concentration, the simulated and measured $\sum m_{\text{Me}^{2+}}$ agree rather good. Hence, supporting the assumption that calcite (CaCO_3) and magnesite (MgCO_3) dissolve and precipitate in a substitution-like manner.

The presence of SO_4^{2-} in brine 4 may have caused the calcite (CaCO_3) dissolution rate to be slightly higher than the magnesite (MgCO_3) precipitation rate. Comparing the measured $\sum m_{\text{Me}^{2+}}$ of brines 4 and 6, shown in figure 6.19, the measured amount is slightly higher than the computed. This statement is based on two observations: 1) the relatively good match of simulated and measured Mg^{2+} effluent, whilst Ca^{2+} effluent is under-predicted, and 2) the sum of the measured divalent cations are consequently higher than the injected Mg^{2+} concentration. On the contrary, this difference may

be a result of surface reactions, e.g. more Ca^{2+} desorb, than Mg^{2+} adsorb. It is worth noting that this observation might be a result of uncertainties from IC measurements, or mixing of the brines. Thus, no final conclusion is drawn from this observation.

Considering brine 9 injection sequences, where Ba^{2+} is the only reactive injected specie, the sum of effluent divalent cations ($\sum m_{\text{Me}^{2+}}$) equal the injected Ba^{2+} concentration. Thus, these sequences support the substitution-like mechanism. By further evaluating the simulated results herein, the Ca^{2+} effluent match very good, whilst Ba^{2+} effluent indicate a witherite (BaCO_3) precipitation rate that is a bit too high, see discussion in subsection 6.2.2 for the explanation. Moreover, the simulation indicates dissolution of magnesite (MgCO_3), which from the experimental results does not occur. The simulated Mg^{2+} effluent correspond difference of simulated and IC measured Ba^{2+} concentrations. There are some possible explanations for the too-high Mg^{2+} simulated effluent, e.g. the mineral selection. Discussed in section 6.1, the minerals selected consist of one divalent cation and one carbonate or sulphate. Consequently, if formation of multi-divalent-cation-bearing carbonates or sulphates occur in the experiment, e.g. hydromagnesite ($\text{Mg}_5(\text{CO}_3)_4(\text{OH})_2 \cdot 4\text{H}_2\text{O}$), the model will not capture it. Seen in table 2.4, presenting the geochemical analysis of the cores, the magnesium content in the flooded slices are higher than in the unflooded end-pieces, yet findings from SEM analysis did not detect any magnesite (MgCO_3) in M12. The SEM analysis did, however, detect magnesium in the flooded slices this was found in clay accumulations in some pores.

Considering the 8th flooding sequence in M12, the sum of all measured cations consequently lie below the injected concentration of Ba^{2+} , thus indicating that more mols of divalent cations are retained than produced. The retained-produced difference might be related to surface reactions. Based on the great amount of Ba^{2+} that is flushed out during the first days of brine 10 injection, i.e. the following sequence, demonstrated in figure 6.20 after 470 days.

A similar explanation could be applicable for the brine 10 sequence of M12. Demonstrated through figure 6.20, Ca^{2+} is the active specie injected, and according to the effluent measurements, the three other divalent cations injected in the chalk core are back-produced. Focusing on the measured $\sum m_{\text{Me}^{2+}}$, which is significantly higher than the injected Ca^{2+} concentration, may indicate that experimental dissolution occur at a higher rate than dissolution. This difference, similar to previous sequences may be a result of surface reactions.

Brine 3 consists of 2 reactive components, both with a concentration of $12 \cdot 10^{-3} \text{mol/litre}$, thus if the substitution-like theory is valid, the measured $\sum m_{\text{Me}^{2+}}$ should be equal $24 \cdot 10^{-3}$. Demonstrated in figure 6.21, did the steady-state effluent of all cations stabilized above this level. Unlike the other sequences that achieved steady-state, discussed earlier, these results indicate that the dissolution rate is higher than the precipitation rate. Korsnes and Madland (2017) observed that the compaction rate reduced during the injection of Sr^{2+} and/or Ba^{2+} , and related this to the size of barium and strontium carbonate minerals, which are greater than calcite (CaCO_3). By comparing this effluent

behaviour with results from M12, the extra effluent of divalent cations seems to be related to retention of Sr^{2+} . As discussed earlier, when Ba^{2+} was injected the measured $\sum m_{\text{Me}^{2+}}$ equal the injected concentration of Ba^{2+} , whilst during Sr^{2+} injection the $\sum m_{\text{Me}^{2+}}$ was slightly higher than the injected Sr^{2+} concentration. No conclusion can be drawn from this observation, but there might be a synergy of the complex interplay between these cations, affecting the dissolution and precipitation rates.

7 | Conclusion

- A 1D advection-dispersion-reaction (ADR) model was developed to match experimental results. The system is defined by a set of partial differential equations, which introduces a substitution-like dissolution and precipitation behaviour for the carbonates. The simulated effluents produce a good fit with the experimental results, consequently indicating that the carbonate dissolution and precipitation behave substitution-like.
- The mineral selection is based on a static model, experimental findings, and literature. Anhydrite (CaSO_4), calcite (CaCO_3), celestite (SrSO_4), magnesite (MgCO_3), strontianite (SrCO_3), and witherite (BaCO_3) were chosen to capture the retention and production the different ions and compute the geochemical alterations.
- Reaction kinetics from literature is demonstrated to produce too high rates for direct application in the ADR model to compute suitable history matches. Consequently, tuning parameters are required to reduce dissolution and precipitation reaction rates. Moreover, dissolution and precipitation, which are two different mechanisms, require different sets of tuning parameters to compute matching results. The exponents p and q are assumed to account for both mechanisms, whilst the net rate reduction factors RF are determined specifically for each mechanism. The trend of the reduction factors is that the dissolution mechanism is several orders of magnitude smaller than the precipitation reduction factor.
- The tuning parameters were determined for the carbonate, whilst the sulphates were not, due to poor matching. The carbonate tuning parameters are presented below:

	Calcite	Magnesite	Strontianite	Witherite
p	1	2	2	3
q	1	2	1	1
RF^{dis}	$2.7 \cdot 10^{-6}$	$2.0 \cdot 10^{-8}$	$1.0 \cdot 10^{-11}$ *	$3.0 \cdot 10^{-21}$
			$7.0 \cdot 10^{-15}$ **	
RF^{prec}	$6.0 \cdot 10^{-5}$	$8.0 \cdot 10^{-3}$	$5.0 \cdot 10^{-10}$	$5.0 \cdot 10^{-8}$

* M9 tuning parameter

** M12 tuning parameter

Table 7.1: Carbonate tuning parameters summarized.

- By comparing experimental with simulated results, it is evident that the more data available to adjust tuning parameters, the model captures more effects and mineral specific ion behaviour. Hence, the model computes better matching results. The ADR model reproduces calcite and magnesite behaviour well, witherite is intermediately matched, and strontianite simulation gave a poor match. The matching of SO_4^{2-} injection sequences where anhydrite and celestite were over-saturated, were not matched. Hence, their tuning parameters were not defined.

7.1 Future Work

To obtain better solutions tomorrow, recommendations from yesterday's experience have to be shared today. Consequently, the bullet points below address challenges met through this work, and non-existing data in the literature needed to develop useful models to history match and predict geochemical alterations.

- Perform flooding experiment with systematic variation of concentration of one reactive specie, e.g. Ba^{2+} or Sr^{2+} , to capture the effect of the degree of super-saturation, in accordance with the theory expressed with figure 3.2. Where only one reactive specie is flooded in each core. A similar suggestion was made by Halvorsen (2013).
- Perform experimental test similar to Hanchen et al. (2008), where magnesium is substituted with barium and strontium.
- Define precipitation parameters that depend on the activity of its component, such as $a_{\text{Me}^{2+}}$ and $a_{\text{CO}_3^{2-}}$ for carbonates, as discussed by Plummer et al. (1978) and Chou et al. (1989).
- Use x-ray diffraction (XRD) to identify what components that combine to form minerals, consequently improve mineral selection.
- Investigate reaction kinetics of several relevant minerals, such as the minerals used herein. The absence of correct and reliable input parameters creates uncertain results, making them more "indications" than "conclusions".
- Use another software to match data. In PHREEQC parameter tuning is done manually, which makes it very time consuming. In this PHREEQC module describing document the advantage of doing this, and how to do it is explained.
- Include variation in available surface sites as a function of what minerals that are present. Demonstrated by Andersen et al. (2018), will the number of sites increase where magnesite is formed.
- From experimental data, define the reaction kinetic parameters for carbonates in accordance with the chemical set-up used by Plummer et al. (1978), Busenberg and Plummer (1986), and Chou et al. (1989). The reaction equations they considered are shown in subsection 5.2.4. Thus, considering the effect of aqueous components that either catalyze or inhibit reaction rates.

Bibliography

- Altree-Williams, A., Brugger, J., Pring, A., and Bedrikovetsky, P. (2019). Coupled reactive flow and dissolution with changing reactive surface and porosity. *Chemical Engineering Science*.
- Andersen, P., Wang, W., Madland, M., Zimmermann, U., Korsnes, R., Bertolino, S., Minde, M., Schulz, B., and Gilbricht, S. (2018). Comparative study of five outcrop chalks flooded at reservoir conditions: Chemo-mechanical behaviour and profiles of compositional alteration. *Transport in Porous Media*, 121(1):135–181.
- Andersen, P. Ø. (2010). Mathematical modeling of water-rock chemistry during water injection and its impact on the composition and porosity of chalk. Master’s thesis, University of Stavanger, Norway.
- Andersen, P. Ø., Evje, S., Madland, M. V., and Hiorth, A. (2012). A geochemical model for interpretation of chalk core flooding experiments. *Chemical engineering science*, 84:218–241.
- Appelo, C. and Parkhurst, D. (2013). Description of input and examples for PHREEQC version 3—a computer program for speciation, batch-reaction, one-dimensional transport, and inverse geochemical calculations: U.S. Geological Survey Techniques and Methods. Available at <https://pubs.usgs.gov/tm/06/a43/>.
- Appelo, C. A. J. and Postma, D. (2005). *Geochemistry, groundwater and pollution*. Balkema, Leiden, 2nd edition.
- Atkins, P. and de Paula, J. (2002). *Atkins’ physical chemistry*. Oxford University Press, Oxford, 7th ed. edition.
- Austad, T. (2013). Water-based EOR in carbonates and sandstones. In *Enhanced Oil Recovery Field Case Studies*, pages 301–335. Elsevier.
- Azimi, G. and Papangelakis, V. G. (2011). Mechanism and kinetics of gypsum–anhydrite transformation in aqueous electrolyte solutions. *Hydrometallurgy*, 108(1-2):122–129.
- Bedrikovetsky, P., Lopes, R., Gladstone, P., Rosario, F., Bezerra, M., and Lima, E. (2004). Barium sulphate oilfield scaling: Mathematical and laboratory modelling. In *SPE International Symposium on Oilfield Scale*. Society of Petroleum Engineers.
- BinMerdhah, A. B., Yassin, A. A. M., and Muherei, M. A. (2010). Laboratory and prediction of barium sulfate scaling at high-barium formation water. *Journal of Petroleum Science and Engineering*, 70(1-2):79–88.
- Bjørlykke, K. (2015). *Petroleum Geoscience: From Sedimentary Environments to Rock Physics*. Berlin, Heidelberg, 2nd ed. edition.

- Blount, C. W. (1974). Synthesis of barite, celestite, anglesite, witherite, and strontianite from aqueous solution. *American Mineralogist: Journal of Earth and Planetary Materials*, 59(11-12):1209–1219.
- Borromeo, L., Egeland, N., Wettrhus Minde, M., Zimmermann, U., Andò, S., Madland, M., and Korsnes, R. (2018). Quick, easy, and economic mineralogical studies of flooded chalk for EOR experiments using raman spectroscopy. *Minerals*, 8(6):221. <https://www.mdpi.com/2075-163X/8/6/221>.
- Bose, S., Hu, X., and Higgins, S. R. (2008). Dissolution kinetics and topographic relaxation on celestite (001) surfaces: The effect of solution saturation state studied using atomic force microscopy. *Geochimica et Cosmochimica Acta*, 72(3):759–770.
- Busenberg, E. and Plummer, L. N. (1986). The solubility of BaCO₃ (cr)(witherite) in CO₂-H₂O solutions between 0 and 90°C, evaluation of the association constants of BaHCO₃⁺ (aq) and BaCO₃⁰ (aq) between 5 and 80°C, and a preliminary evaluation of the thermodynamic properties of Ba²⁺ (aq). *Geochimica et Cosmochimica Acta*, 50(10):2225–2233.
- Carlson, W. D. (1980). The calcite-aragonite equilibrium: effects of sr substitution and anion orientational disorder. *American Mineralogist*, 65(11-12):1252–1262.
- Chagneau, A., Claret, F., Enzmann, F., Kersten, M., Heck, S., Madé, B., and Schäfer, T. (2015). Mineral precipitation-induced porosity reduction and its effect on transport parameters in diffusion-controlled porous media. *Geochemical Transactions*, 16(1).
- Chou, L., Garrels, R. M., and Wollast, R. (1989). Comparative study of the kinetics and mechanisms of dissolution of carbonate minerals. *Chemical geology*, 78(3-4):269–282.
- Cook, C., Andersen, M., Halle, G., Gislefoss, E., and Bowen, G. (2001). An approach to simulating the effects of water-induced compaction in a North Sea reservoir (includes associated papers 73134 and 73135). *SPE Reservoir Evaluation & Engineering*, 4(02):121–127.
- Declercq, J. and Oelkers, E. H. (2014). Carbfix report 4 PHREEQC mineral dissolution kinetics database 5.
- Dove, P. M. and Czank, C. A. (1995). Crystal chemical controls on the dissolution kinetics of the isostructural sulfates: Celestite, anglesite, and barite. *Geochimica et Cosmochimica Acta*, 59(10):1907–1915.
- Egeland, N., Minde, M., Kobayashi, K., Ota, T., Nakamura, E., Zimmermann, U., Madland, M., and Korsnes, R. (2017). Quantification of mineralogical changes in flooded carbonate under reservoir conditions. In *IOR 2017 - 19th European Symposium on Improved Oil Recovery*. EAGE Publications BV.
- Erdemoğlu, M. and Canbazoğlu, M. (1998). The leaching of SrS with water and the precipitation of SrCO₃ from leach solution by different carbonating agents. *Hydrometallurgy*, 49(1-2):135–150.

- Evje, S., Hiorth, A., Madland, M. V., and Korsnes, R. I. (2009). A mathematical model relevant for weakening of chalk reservoirs due to chemical reactions. *NHM*, 4(4):755–788.
- Fathi, S. J., Austad, T., and Strand, S. (2011). Water-based enhanced oil recovery (EOR) by “smart water”: Optimal ionic composition for EOR in carbonates. *Energy & Fuels*, 25(11):5173–5179.
- Fjær, E., Holt, R. M., Raaen, A., Risnes, R., and Horsrud, P. (2008). *Petroleum related rock mechanics*, volume 53. Elsevier.
- Geitle, K. (2013). Chemically induced compaction in fractured and intact chalk cores. Master’s thesis, University of Stavanger, Norway.
- Goody, D. C., Kinniburgh, D. G., and Barker, J. A. (2007). A rapid method for determining apparent diffusion coefficients in chalk and other consolidated porous media. *Journal of Hydrology*, 343(1-2):97–103.
- Halvorsen, C. (2013). Effect of barium and strontium on low salinity waterflooding. Master’s thesis, University of Stavanger, Norway.
- Hänchen, M., Prigiobbe, V., Baciocchi, R., and Mazzotti, M. (2008). Precipitation in the Mg-carbonate system—effects of temperature and CO₂ pressure. *Chemical Engineering Science*, 63(4):1012–1028.
- Heggheim, T., Madland, M., Risnes, R., and Austad, T. (2005). A chemical induced enhanced weakening of chalk by seawater. *Journal of Petroleum Science and Engineering*, 46(3):171–184.
- Heiter, P. F. and Lebedez, D. (2012). On numerical methods for stiff ordinary differential equation systems.
- Hermansen, H., Landa, G., Sylte, J., and Thomas, L. (2000). Experiences after 10 years of waterflooding the Ekofisk Field, Norway. *Journal of Petroleum Science and Engineering*, 26(1-4):11–18.
- Hiorth, A., Jettestuen, E., Cathles, L., and Madland, M. (2013). Precipitation, dissolution, and ion exchange processes coupled with a lattice Boltzmann advection diffusion solver. *Geochimica et Cosmochimica Acta*, 104:99–110.
- Jordan, M. M., Collins, I. R., and Mackay, E. J. (2008). Low sulfate seawater injection for barium sulfate scale control: A life-of-field solution to a complex challenge. *SPE Production & Operations*, 23(02):192–209.
- Kamari, A., Gharagheizi, F., Bahadori, A., and Mohammadi, A. H. (2014). Rigorous modeling for prediction of barium sulfate (barite) deposition in oilfield brines. *Fluid Phase Equilibria*, 366:117–126.
- Kim, S., Chen, J., Cheng, T., Gindulyte, A., He, J., He, S., Li, Q., Shoemaker, B. A., Thiessen, P. A., Yu, B., Zaslavsky, L., Zhang, J., and Bolton, E. E. (2019). PubChem 2019 update: improved access to chemical data. *Nucleic Acids Research*, 47(D1):D1102–D1109.

- Korrani, A. K. N., Sepehrnoori, K., and Delshad, M. (2015). Coupling IPhreeqc with UTCHEM to model reactive flow and transport. *Computers & Geosciences*, 82:152–169.
- Korsnes, R. I. and Madland, M. V. (2017). *The Effect on Compaction Rates by Divalent Anion and Cations on Outcrop Chalk Tested at Reservoir Temperature and Effective Stress Conditions*, pages 706–714. American Society of Civil Engineers (ASCE). Available at <https://ascelibrary.org/doi/abs/10.1061/9780784480779.087>.
- Kristiansen, T. G. and Plischke, B. (2010). History matched full field geomechanics model of the Valhall field including water weakening and re-pressurisation. In *SPE EUROPEC/EAGE Annual Conference and Exhibition*. Society of Petroleum Engineers.
- Laidler, K. J. (1984). The development of the Arrhenius equation. *Journal of Chemical Education*, 61(6):494.
- Laidler, K. J. and King, M. C. (1983). Development of transition-state theory. *The Journal of Physical Chemistry*, 87(15):2657–2664.
- Lasaga, A. (1998). Reaction kinetics in geoscience, 811 p.
- Li, Y.-H., Crane, S. D., and Coleman, J. R. (1995). A novel approach to predict the co-precipitation of BaSO₄ and SrSO₄. In *SPE Production Operations Symposium*. Society of Petroleum Engineers.
- Madland, M., Hiorth, A., Omdal, E., Megawati, M., Hildebrand-Habel, T., Korsnes, R., Evje, S., and Cathles, L. (2011). Chemical alterations induced by rock–fluid interactions when injecting brines in high porosity chalks. *Transport in porous media*, 87(3):679–702.
- Martínez, A. and Uribe, A. (1995). Interfacial properties of celestite and strontianite in aqueous solutions. *Minerals Engineering*, 8(9):1009–1022.
- Marty, N. C. M., Claret, F., Lassin, A., Tremosa, J., Blanc, P., Madé, B., Giffaut, E., Cochapin, B., and Tournassat, C. (2015). A database of dissolution and precipitation rates for clay-rocks minerals. *Applied Geochemistry*, 55:108–118.
- Masterton, W. L. and Hurley, C. N. (2004). *Chemistry: principles and reactions*. Thomson Brooks/Cole, Belmont, Calif, 5th ed. edition.
- Mavroudakis, E., Cuccato, D., and Moscatelli, D. (2019). Determination of reaction rate coefficients in free-radical polymerization using density functional theory. In *Computational Quantum Chemistry*, pages 47–98. Elsevier.
- Megawati, M., Hiorth, A., and Madland, M. (2013). The impact of surface charge on the mechanical behavior of high-porosity chalk. *Rock mechanics and rock engineering*, 46(5):1073–1090.
- Megawati, M., Madland, M. V., and Hiorth, A. (2015). Mechanical and physical behavior of high-porosity chalks exposed to chemical perturbation. *Journal of Petroleum Science and Engineering*, 133:313–327.

- Meling, T. T. (2013). Geochemical modeling of low salinity core flooding. Master's thesis, University of Stavanger, Norway.
- Mindat.org (2019). Mines and Mining - The Hudson Institute of Mineralogy. <https://www.mindat.org/>, date retrieved 12.04.2019.
- Minde, M. W. (2018). *Mineral Replacements in Flooding Experiments Linked to Enhanced Oil Recovery in Chalk*. PhD thesis.
- Morse, J. and Mackenzie, F. (1990). *Geochemistry of sedimentary carbonates*, volume 48 of *Developments in sedimentology*. Elsevier, Amsterdam.
- Nagel, N. (2001). Compaction and subsidence issues within the petroleum industry: From wilming-ton to ekofisk and beyond. *Physics and Chemistry of the Earth, Part A: Solid Earth and Geodesy*, 26(1-2):3–14.
- Oxtoby, D. W. (1992). Homogeneous nucleation: theory and experiment. *Journal of Physics: Condensed Matter*, 4(38):7627.
- Palandri, J. L. and Kharaka, Y. K. (2004). A compilation of rate parameters of water-mineral interaction kinetics for application to geochemical modeling. Technical report, Geological Survey Menlo Park CA.
- Parkhurst, D. and Appelo, C. (1999). Users guide to PHREEQC (v2)—a computer program for spe-ciation, batch-reaction, one-dimensional transport, and inverse geochemical calculations. *Water-resources investigation report*, pages 99–4259.
- Pedersen, J., Jettestuen, E., Madland, M. V., Hildebrand-Habel, T., Korsnes, R. I., Vinningland, J. L., and Hiorth, A. (2016). A dissolution model that accounts for coverage of mineral surfaces by precipitation in core floods. *Advances in water resources*, 87:68–79.
- Plummer, L. N., Wigley, T. M. L., and Parkhurst, D. L. (1978). The kinetics of calcite dissolution in CO₂ -water systems at 5 °C to 60 °C and 0.0 to 1.0 atm CO₂. *American Journal of Science*, 278(2):179–216.
- Pokrovsky, O. S. and Schott, J. (1999). Processes at the magnesium-bearing carbonates/solution interface. II. kinetics and mechanism of magnesite dissolution. *Geochimica et Cosmochimica Acta*, 63(6):881–897.
- Punternvold, T. (2008). *Waterflooding of carbonate reservoirs: EOR by wettability alteration*. PhD thesis.
- Rocha, A., Frydman, M., da Fontoura, S., Rosario, F., and Bezerra, M. (2001). Numerical modeling of salt precipitation during produced water reinjection. In *International Symposium on Oilfield Scale*. Society of Petroleum Engineers.

- Ruddy, I., Andersen, M. A., Pattillo, P., Bishlawi, M., and Foged, N. (1989). Rock compressibility, compaction, and subsidence in a high-porosity chalk reservoir: A case study of Valhall field. *Journal of Petroleum Technology*, 41(07):741–746.
- Ruiz-Agudo, E., Putnis, C. V., Hövelmann, J., Álvarez-Lloret, P., Ibañez-Velasco, A., and Putnis, A. (2015). Experimental study of the replacement of calcite by calcium sulphates. *Geochimica et Cosmochimica Acta*, 156:75–93.
- Rumynin, V. G. (2012). *Subsurface Solute Transport Models and Case Histories: With Applications to Radionuclide Migration*, volume 25. Springer Science & Business Media.
- Sævik, P. N. (2011). Reactive transport in porous media. Master’s thesis, The University of Bergen.
- Saldi, G. D., Jordan, G., Schott, J., and Oelkers, E. H. (2009). Magnesite growth rates as a function of temperature and saturation state. *Geochimica et Cosmochimica Acta*, 73(19):5646–5657.
- Shiraki, R. and Brantley, S. L. (1995). Kinetics of near-equilibrium calcite precipitation at 100°C: An evaluation of elementary reaction-based and affinity-based rate laws. *Geochimica et Cosmochimica Acta*, 59(8):1457–1471.
- Stephen King (2012). *11.22.63*. Hodder And Stoughton Ltd.
- Sulak, A. and Danielsen, J. (1988). Reservoir aspects of Ekofisk subsidence. In *Offshore Technology Conference*. Offshore Technology Conference.
- Sylte, J., Thomas, L., Rhett, D., Bruning, D., and Nagel, N. (1999). Water induced compaction in the Ekofisk field. In *SPE Annual Technical Conference and Exhibition*. Society of Petroleum Engineers.
- Talman, S., Wiwchar, B., Gunter, W., Scarge, C., Spencer, R., and Chou, I. (1990). Dissolution kinetics of calcite in the H₂O-CO₂ system along the steam saturation curve to 210°C. *Fluid-Mineral Interactions: A Tribute to HP Eugster*, pages 41–55.
- Tansey, J. F. (2016). *Multiscale pore network modeling of carbonate acidization*. PhD thesis.
- Temple, E., Jordan, M., Williams, H., Kjelstrup, S., Kilibarda, M., and Johansen, K. (2019). Development of a barium sulphate scale inhibitor for chalk solid loaded conditions. In *SPE International Conference on Oilfield Chemistry*. Society of Petroleum Engineers.
- Todd, A. C. and Yuan, M. (1990). Barium and strontium sulfate solid solution formation in relation to North Sea scaling problems. *SPE Production Engineering*, 5(03):279–285.
- Volcke, E. I., Van Hulle, S., Deksissa, T., Zaher, U., and Vanrolleghem, P. (2005). Calculation of pH and concentration of equilibrium components during dynamic simulation by means of a charge balance. Technical report, BIOMATH Tech. Report, Ghent University, Ghent, Belgium.

- Wang, W., Zhou, C., Liu, Y., Wu, Z., and Huang, F. (2019). Equilibrium Mg isotope fractionation among aqueous Mg^{2+} , carbonates, brucite and lizardite: Insights from first-principles molecular dynamics simulations. *Geochimica et Cosmochimica Acta*.
- Witthüser, K., Arnepalli, D., and Singh, D. N. (2006). Investigations on diffusion characteristics of granite and chalk rock mass. *Geotechnical and Geological Engineering*, 24(2):325–334.
- Wolf, R. E. (2005). What is ICP-MS? and more importantly, what can it do? *US Geological Survey*, 7.
- Zeppenfeld, K. (2006). Crystallization kinetics of strontianite from $\text{Sr}(\text{HCO}_3)_2$ solutions. *Geochemistry*, 66(4):319–323.
- Zhang, P., Tweheyo, M. T., and Austad, T. (2007). Wettability alteration and improved oil recovery by spontaneous imbibition of seawater into chalk: Impact of the potential determining ions Ca^{2+} , Mg^{2+} , and SO_4^{2-} . *Colloids and Surfaces A: Physicochemical and Engineering Aspects*, 301(1-3):199–208.
- Zieba, A. and Nancollas, G. (1994). Constant composition kinetics studies of the simultaneous crystal growth of alkaline earth carbonates: the calcium/strontium system. *Journal of Crystal Growth*, 144(3-4):311–319.
- Zimmermann, U., Madland, M. V., Neramoen, A., Hildebrand-Habel, T., Bertolino, S. A., Hiorth, A., Korsnes, R. I., Audinot, J.-N., and Grysan, P. (2015). Evaluation of the compositional changes during flooding of reactive fluids using scanning electron microscopy, nano-secondary ion mass spectrometry, x-ray diffraction, and whole-rock geochemistry compositional changes during flooding. *AAPG Bulletin*, 99(5):791–805.

A | Electron Microscopy Analysis

In the following energy dispersive x-ray spectroscopy (EDS) spectrum, energy characteristics of palladium (Pd) appear on all analyzes. This is a result of the preparation of the samples, as discussed in subsection 2.4.2, consequently the Pd peaks are neglected. The images are taken with backscattered electron (BSE), thus the brighter phases have a higher atomic mass than the darker ones.

In the table presented below, the semi-quantified relative amounts of the detected elements are presented.

Element	Figure A.1		Figure A.2		Figure A.4		Figure A.3	
	<i>wt%</i>	<i>Atomic%</i>	<i>wt%</i>	<i>Atomic%</i>	<i>wt%</i>	<i>Atomic%</i>	<i>wt%</i>	<i>Atomic%</i>
Carbon	-	-	8.4	17.9	21.4	52.6	38.4	60.7
Oxygen	27.5	57.5	24.9	39.7	18.5	34	26.1	31
Strontium	42.1	16.1	-	-	0.4	0.1	33.1	7.2
Sulphur	22.4	23.4	-	-	-	-	-	-
Calcium	1.7	1.4	66.6	42.4	0.9	0.6	2.4	1.2
Barium	6.4	1.6	-	-	58.8	12.6	-	-

Table A.1: Semi-quantification of elements from EDS analysis.

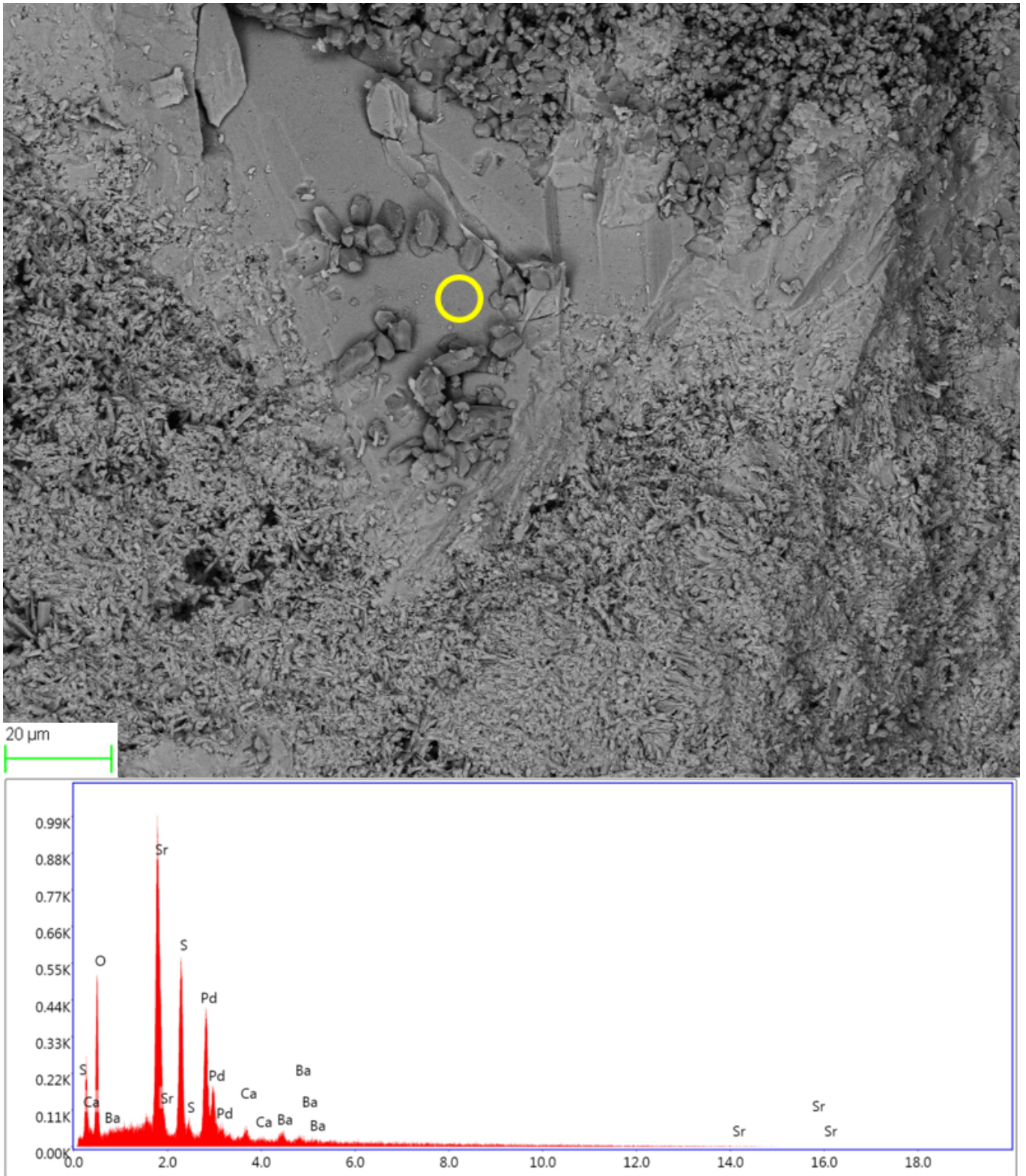


Figure A.1: EDS of the inlet slice (s1. in figure 2.5 B)) of M9. The spectrum of the are within the yellow circle shows findings of strontium, sulphide, oxygen, calcium, carbon and oxygen. This BSE SEM finding and EDS analysis caused the inclusion of celestite (SrSO_4) in the modeling, as discussed in section 6.1.

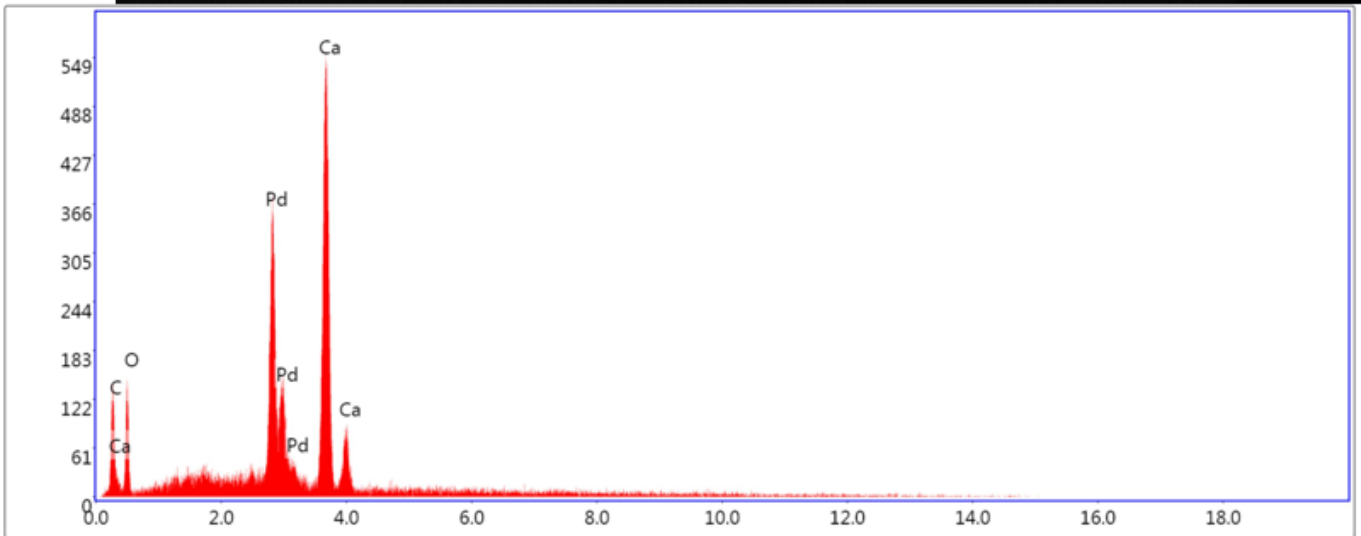
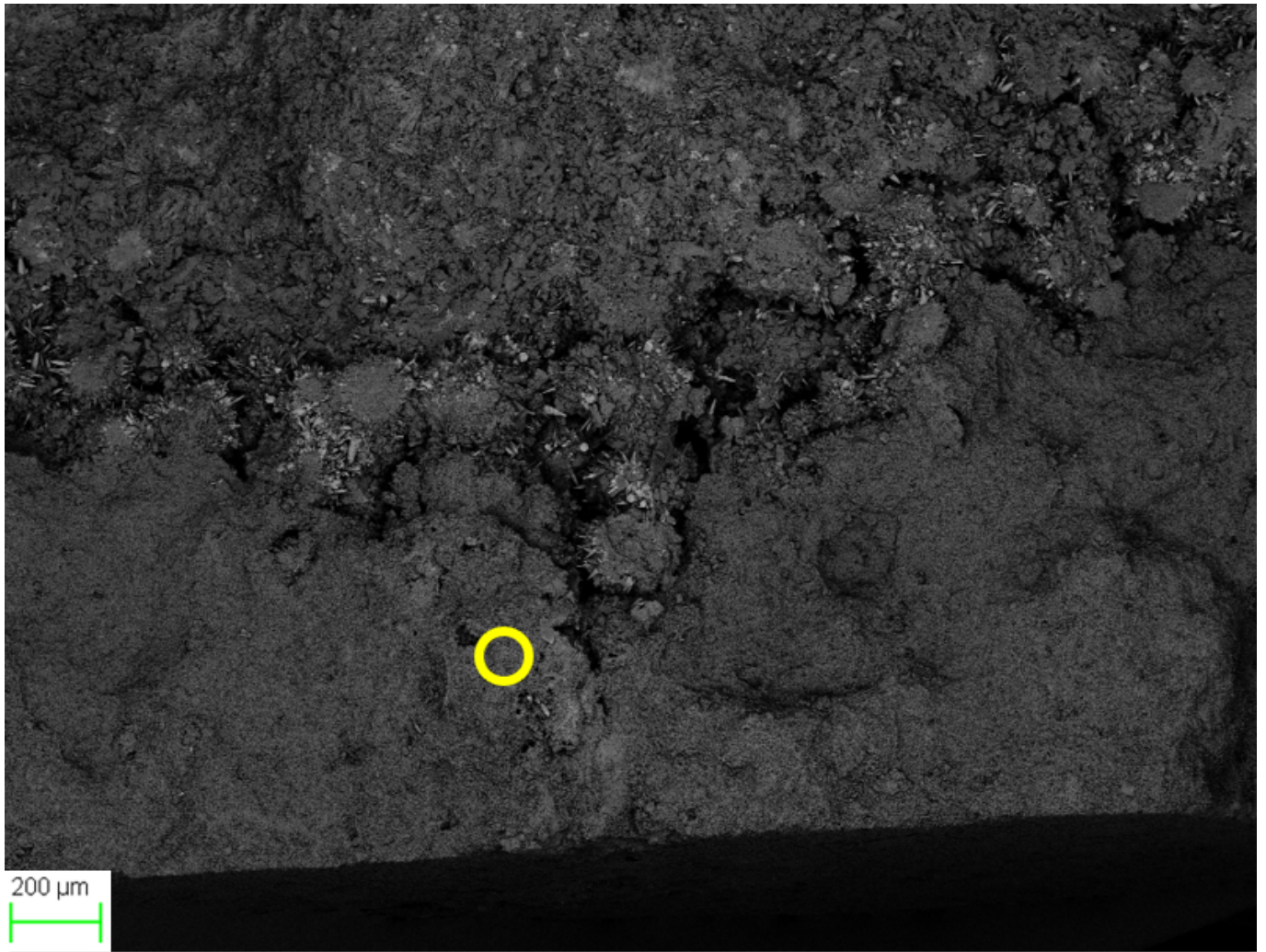


Figure A.2: EDS of the inlet slice (s1. in figure 2.5 B)) of M12. The spectrum of the are within the yellow circle shows findings of calcium, carbon and oxygen. This was an expected result, since the Mons chalk has an purity of 99wt% CaCO_3 Megawati et al. (2015); Korsnes and Madland (2017); Andersen et al. (2018). Nevertheless, the EDS analysis supports the inclusion of calcite.

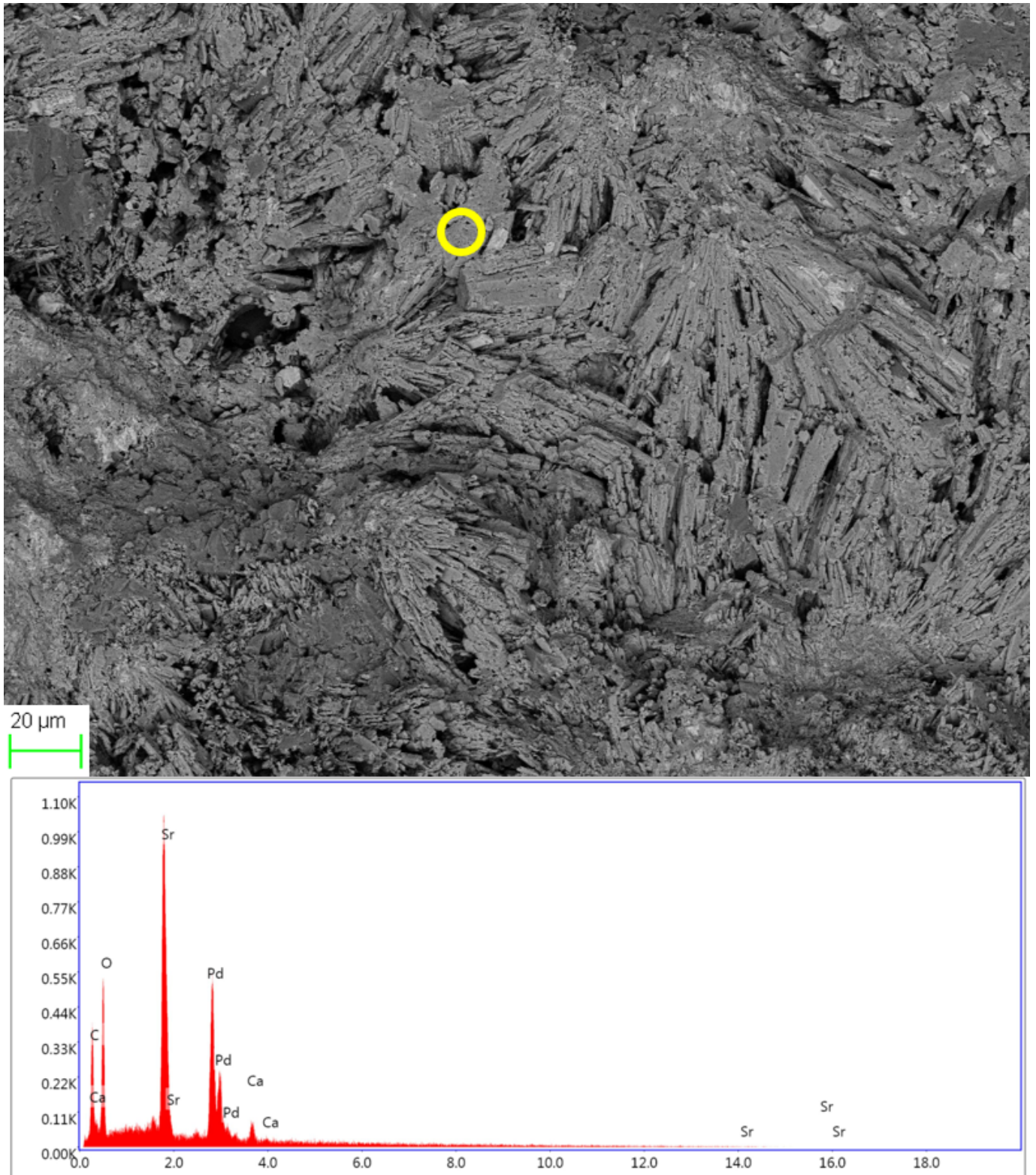


Figure A.3: EDS of the inlet slice (s1. in figure 2.5 B)) of M12. The spectrum of the area within the yellow circle shows findings of strontium, sulphide, oxygen, calcium, carbon and oxygen. It was assumed that the loss and gain of Sr^{2+} could be explained by a strontium-carbonate, but the crystallography of presented with this BSE SEM image and EDS analysis supports the choice of strontianite (SrCO_3), discussed in section 6.1.

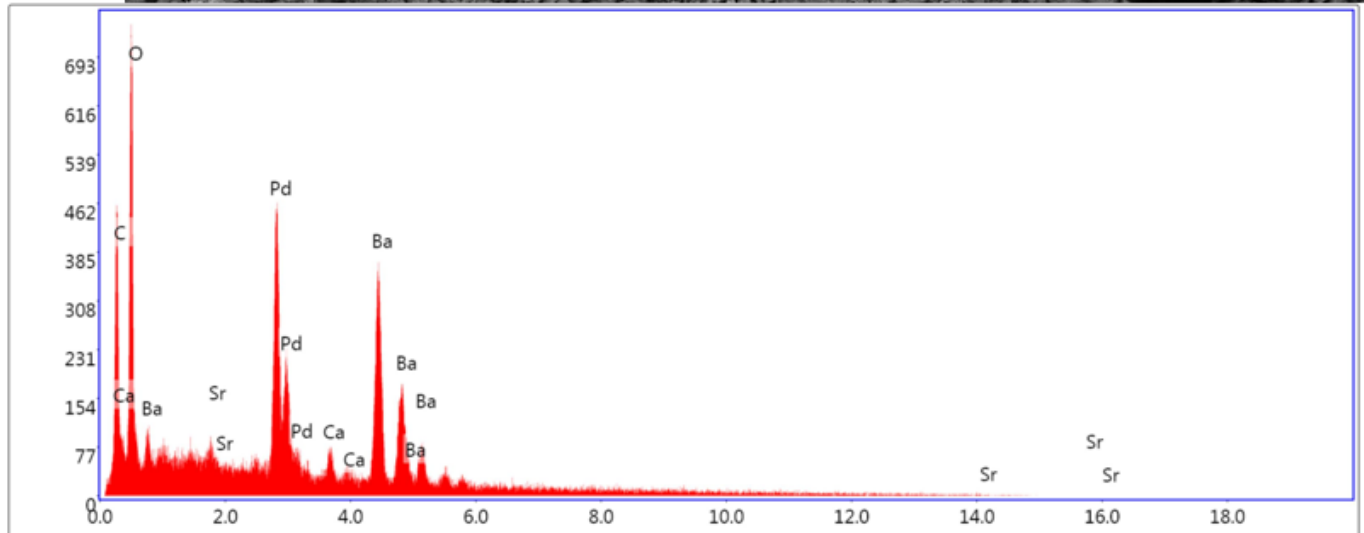
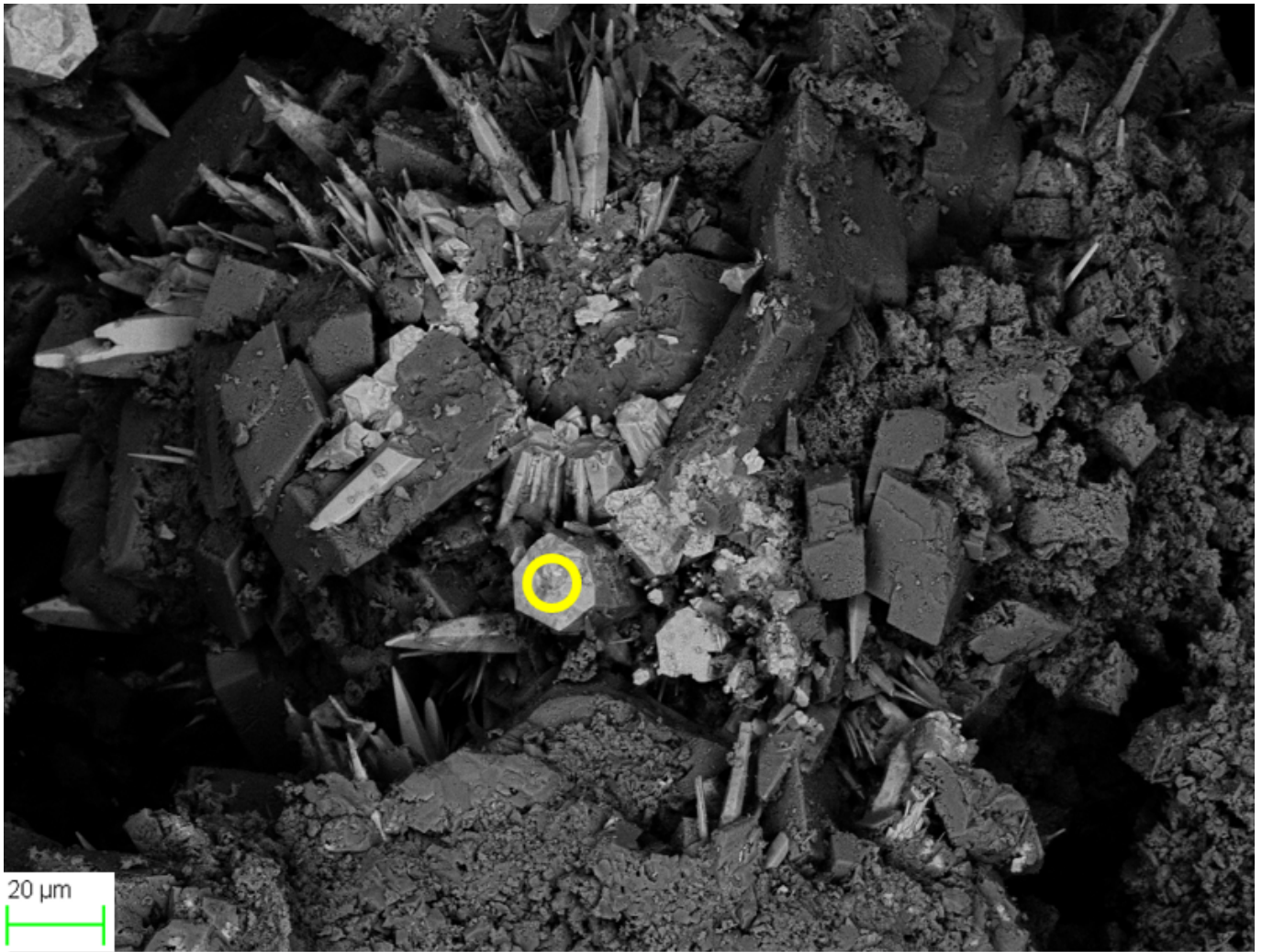


Figure A.4: EDS of the inlet slice (s1. in figure 2.5 B)) of M12. The spectrum of the are within the yellow circle shows findings of barium, carbon, oxygen, and sparse amount of strontium and calcium. It was assumed that the loss and gain of Ba^{2+} could be explained by a barium-carbonate, but the hexagonal crystallography detected with this BSE SEM image and the EDS analysis supports the choice of witherite ($BaCO_3$), discussed in section 6.1.

B | Poster Presentations

This thesis was presented with a poster both at the IOR NORWAY conference, and at the graduation ceremony at the University of Stavanger.

At the IOR NORWAY conference 19th and 20th of March held at the University of Stavanger, this thesis was presented. A poster was made to demonstrate the objective, methodology, results at that time, and future work. For more information about the conference see: IOR NORWAY 2019.

At the graduation ceremony, the essence of the work was presented. The poster was intended to present the academic performed during the Master of Sciences thesis', to fellow students, the department and the industry.

Introduction

Water injection is a well proved enhanced oil recovery (EOR) method, and mechanisms related to the method has extensively been studied. Laboratory experiments of core flooding has demonstrated the composition of the injected brine is an important factor when flooding carbonate rock. The concentration of divalent ions, e.g. Ca^{2+} , Mg^{2+} , and SO_4^{2-} , has proved to affect the stability of the carbonate matrix, and the oil recovery.

On a world basis approximately 60 % of oil and 40 % of gas are held in carbonate reservoirs. On the Norwegian Continental Shelf (NCS) the Ekofisk and Valhall fields are chalk carbonate reservoirs. Both fields have experienced reservoir enhanced compaction and seabed subsidence in regions flooded with sea water.

Chemical effects of brine composition in carbonate reservoirs has been extensively studied, but is not yet completely understood. The geochemical alteration induced by specific ions and ion composition. Geochemical alteration of carbonate rock is controlled by more factors than brine composition, e.g. temperature.

Objectives

- Develop a 1D reaction-transport model in PHREEQC and Matlab, to match effluent measurements from flooding experiments, with 10 different Na-Cl-Ca-Mg-SO₄-Ba-Sr brine compositions.
- Suggest and quantify possible mineral and surface interactions that explain the experimental data.
- Evaluation and prediction of scaling / permeability alteration.
- Couple reaction to compaction to suggest explanation of water weakening effects.

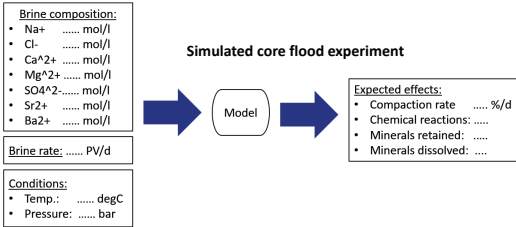


Figure 1: Workflow scheme of model – forward simulation.

Methods

Static modelling:

- Static model developed in PHREEQC v.3.4.
- 10 different brines and potential mixes of these equilibrated with atmospheric CO₂ at standard conditions, and further equilibrated with Calcite (CaCO₃) at reservoir conditions.
- Evaluate probability of mineral precipitation.

Dynamic modelling:

- Defining the initial system:
 - Mons Belgium chalk assumed pure Calcite (Megawati et al. 2015).
 - Petrophysical and physical properties of cores (Korsnes et al. 2017).
 - Test temperature 130°C and pore pressure 0.7 MPa.

- Match the model with effluent data using transport equation (ADR-process):
Rate of Change = Advection + Dispersion + (Chemical) Reactions

$$\frac{\partial c_i}{\partial t} = -v_w \frac{\partial c_i}{\partial x} + D_L \frac{\partial^2 c_i}{\partial x^2} + \text{reaction terms}$$

- Defining chemical reaction kinetic equation (main focus):

$$\text{Reaction rate} = -RF_i \left(\frac{A}{V}\right) (k_{1,i} + k_{2,i} a_h^{n_i}) \cdot \text{sign}(SI) \cdot |1 - S_i \cdot \Omega_i|^{m_i}$$

- RF_i = Reduction factor – tuning parameter
- All other parameter are given or calculated

Given interpretation data:

- Effluent concentration vs. time for 7 ions.
- 10 different injected brine compositions.

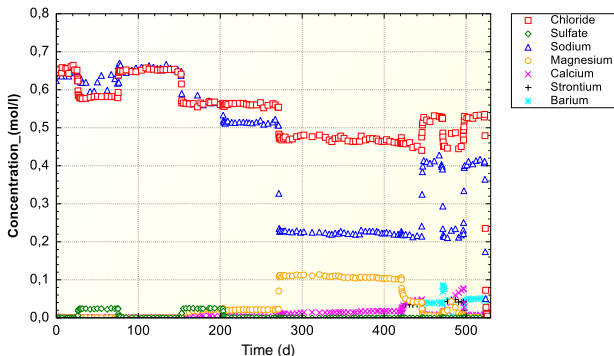


Figure 2: All effluent concentration measured with ion chromatography of 1 of 2 cores flooded by Korsnes et al. (2017). 8 different brine compositions were sequentially flooded. Note: No simulations in this figure.

Results

Potential precipitants:

- 15 minerals gave oversaturated solutions, i.e. potential precipitants. Further evaluation using literature and experimental results, gave a list of 5 minerals to include in the dynamic model.
- Figure 3 is an example illustrating SI-evaluation based on PHREEQC static simulation. Figure 4 shows effluent concentrations from Na-Cl-Mg-SO₄ brine flooding indicate Mg retention, but no retention of SO₄ ions.

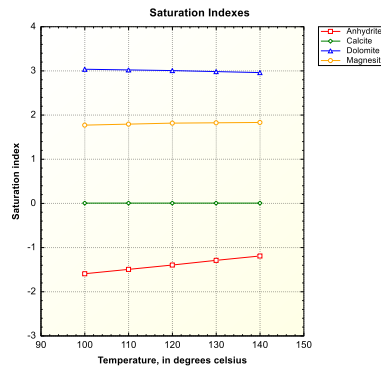


Figure 3: A Na-Cl-Mg-SO₄ brine (Brine 4 in Korsnes et al. (2017)) in equilibrium with atmospheric CO₂ at sc., further equilibrated with solid Calcite (CaCO₃) at 130°C and 0.7 MPa.

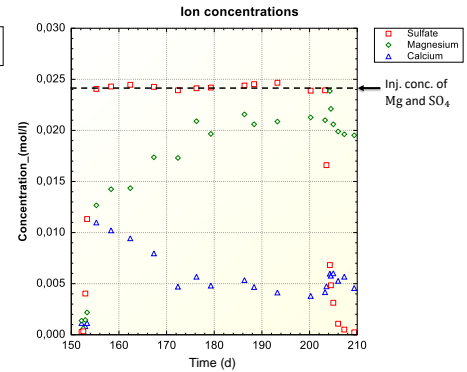


Figure 4: Both injected and effluent concentrations from flooding experiment with a Na-Cl-Mg-SO₄ brine (Brine 4 in Korsnes et al. (2017)). Illustrating validity of static saturation index evaluation, by loss of Mg.

Matching effluent concentrations:

- Using kinetic rate parameters from literature, neglecting surface reactions, only focusing on Calcite and Witherite precipitation-dissolution reactions.
- At steady state, the simulation indicate a substitution-like reaction between Calcite and Witherite, due to: $\text{Loss of } Ba^{2+} \approx \text{Gain of } Ca^{2+}$
- Simulation in figure. 5 indicate that there is a substitution-like reaction between Calcite and Witherite as the system stabilizes.
- $RF_{\text{Calcite}} = 2 \cdot 10^{-5}$, $RF_{\text{Witherite}} = 10^{-17}$
- Note: Calcite is more soluble than Witherite.

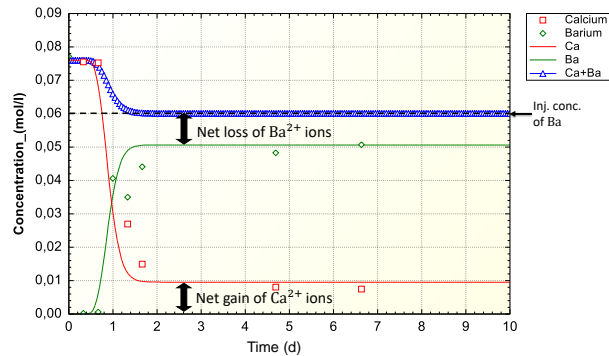


Figure 5: A Na-Cl-Ba brine (Brine 9 in Korsnes et al. (2017)) injected into a Calcite (CaCO₃) core at 130°C and 0.7 MPa.

Conclusions

- Ca-, and Sr-sulphates, and Ca-, Mg-, Ba-, and Sr-carbonate minerals explain experimental results.
- $RF_i < 1$

Further work

- Tune RF_i in the dynamic PHREEQC model to better match the experimental data.
- Improve model to predict geochemical effects

References:

Korsnes, R. I., & Madland, M. V. (2017) The Effect on Compaction Rates by Divalent Anion and Cations on Outcrop Chalk Tested at Reservoir Temperature and Effective Stress Conditions. In Poromechanics VI (pp. 706-714).
Megawati, M., Madland, M. V., & Hirth, A. (2015). Mechanical and physical behavior of high-porosity chalks exposed to chemical perturbation. Journal of Petroleum Science and Engineering, 133, 313-327.

Acknowledgement

The authors acknowledge the Research Council of Norway and the industry partners, ConocoPhillips Skandinavia AS, Aker BP ASA, Eni Norge AS, Equinor ASA, Neptune Energy Norge AS, Lundin Norway AS, Halliburton AS, Schlumberger Norge AS, Wintershall Norge AS, and DEA Norge AS, of The National IOR Centre of Norway for support.

Contact information

Magnus Kongestøl Raaholt
+47 995 70 407
magnusraaholt@gmail.com

Introduction

Seawater injection is a well proved method to improve oil recovery in carbonate reservoirs, and mechanisms related to the method has extensively been studied. Water weakening is one these mechanisms that studied, as it causes an engineering challenge for field development and enhance the compaction drive mechanism. Laboratory experiments of core flooding has demonstrated the composition of the injected brine is an important factor when flooding carbonate rock. The concentration of divalent ions, such as Ca^{2+} , Mg^{2+} , and SO_4^{2-} , has proved to affect the stability of the carbonate matrix, and the oil recovery.

In the industry dissolution and precipitation of carbonates are associated with permeability reduction, scaling and well bore instability. These petrophysical alterations have been proved by multiple experiments, and methods to reduce have been a thoroughly been investigated. Observations from Korsnes and Madland (2017) where the creep compaction rate of outcrop chalk cores reduced as BaCl₂ and SrCl₂ brines were injected, indicate that the incorporation of Ba^{2+} and Sr^{2+} ions in the carbonate lattice re-stabilize the carbonate matrix. An other interesting observation from Korsnes and Madland (2017) was that even though the chalk strength increased, the permeability was not crucially reduced. In following sequence in the same experiment, SO_4^{2-} was injected, causing severe permeability reduction. Consequently indicating that injection of Ba^{2+} and Sr^{2+} brines, absent of SO_4^{2-} , the chalk matrix deformation is retarded, whilst the permeability is preserved. On NCS it is common practice to inject seawater, which contains sufficiently high amounts of SO_4^{2-} to cause severe scaling, consequently water treatment or scale inhibition are required to preserve permeability in carbonate reservoirs. Water treatment equipment, such as the Seabox™, can reduce the sulphate content of seawater, thus allowing for new long-term strategies for choice of injection brine composition.

Many reactive flow experiments have demonstrated effects of specific ions and ion compositions of the injection brine in flooding chalk cores, but what compositions that give the desired reactions in these complex systems remains unclear.

Objectives

- Develop a 1D advection-dispersion-reaction model in PHREEQC, to match effluent measurements from flooding experiments, with 10 different Na-Cl-Ca-Mg-SO₄-Ba-Sr brine compositions.
- Improve geochemical modelling by including barium and strontium carbonates.
- Suggest and quantify possible mineral and surface interactions that explain the experimental data.

Methods

Static modelling:

- Static model developed in PHREEQC v.3.4.
- Evaluate possible precipitants.

Dynamic modelling:

- Defining the initial system:
 - Mons Belgium chalk assumed pure Calcite (Megawati et al. 2015).
 - Petrophysical and physical properties of cores (Andersen et al. 2018; Korsnes et al. 2017).
 - Test temperature 130°C and pore pressure 0.7 MPa.
 - Match the model with effluent data using transport equation (ADR-process):
Rate of Change = Advection + Dispersion + (Chemical) Reactions

$$\partial_t m_i = -\partial_x(v m_i) + \partial_x(D_L \partial_x m_i) + \dot{r}_i$$

- Defining chemical reaction kinetic equation (main focus):

$$\dot{r}_i = -RF_i \left(\frac{A_0}{V} \right) k_i \cdot \text{sign}(SI) \cdot |1 - \Omega_i^{p_i}|^{q_i}$$

- RF_i , p_i , q_i – tuning parameter
- All other parameter are given or calculated

Mineral	Dissolution reaction
Anhydrite	$CaSO_4(s) \rightleftharpoons Ca^{2+}(aq) + SO_4^{2-}(aq)$
Calcite	$CaCO_3(s) \rightleftharpoons Ca^{2+}(aq) + CO_3^{2-}(aq)$
Celestite	$SrSO_4(s) \rightleftharpoons Sr^{2+}(aq) + SO_4^{2-}(aq)$
Magnesite	$MgCO_3(s) \rightleftharpoons Mg^{2+}(aq) + CO_3^{2-}(aq)$
Strontianite	$SrCO_3(s) \rightleftharpoons Sr^{2+}(aq) + CO_3^{2-}(aq)$
Witherite	$BaCO_3(s) \rightleftharpoons Ba^{2+}(aq) + CO_3^{2-}(aq)$

Table 1: Dissolution reactions for included minerals

Results (1)

	Anhydrite	Calcite	Celestite	Magnesite	Strontianite	Witherite
p	1	1	0.5	2	2	3
q	1	1	2	2	1	1
RF^{dis}	ND	$2.7 \cdot 10^{-6}$	ND	$2.0 \cdot 10^{-8}$	$1.0 \cdot 10^{-11}$	$3.0 \cdot 10^{-21}$
RF^{prec}	ND	$6.0 \cdot 10^{-5}$	ND	$8.0 \cdot 10^{-3}$	$5.0 \cdot 10^{-10}$	$5.0 \cdot 10^{-8}$

Table 2: Final tuning parameters.

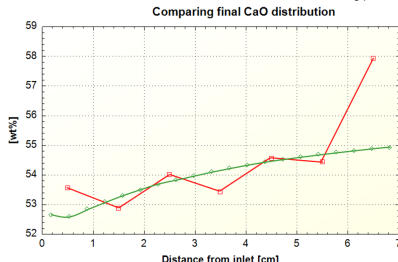


Figure 1: Comparing the final distribution of CaO from geochemical analysis (CaO_exp) and simulation (CaO_sim) of MO10. Since the MO10 core is assumed to initially consist of pure calcite (CaCO₃) the model compute a good dissolution rate and distribution of calcite, resulting in a good CaO match in the 6 first slices.

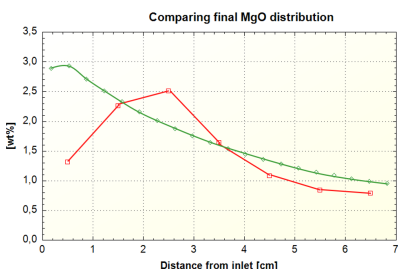


Figure 2: Comparing the final distribution of MgO from geochemical analysis (MgO_exp) and simulation (MgO_sim) of MO10. Simulation does not capture the gradual increasing MgO content in the three first slices. Simulation indicate a higher total content of MgO compared to geochemical analysis.

Results (2)

Figure 3: Final simulated results in the MO10 core. The tuning parameters used are listed in table 2. The IC measured effluents are presented as data points, whilst the lines represent the simulated effluent. $\sum m_{Mg^{2+}}$ symbolize the sum of all divalent cations, for both measured with IC and simulated. Results indicate substitution-like dissolution-precipitation reactions of calcite (CaCO₃) and magnesite (MgCO₃) in this core. Mg²⁺ was injected at $0.219 \frac{mol}{liter}$.

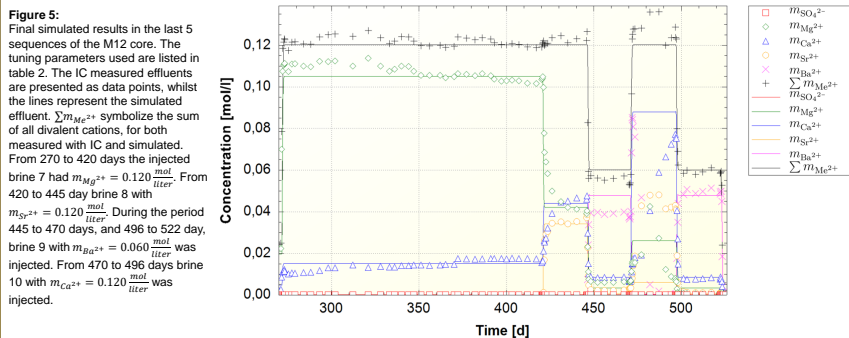
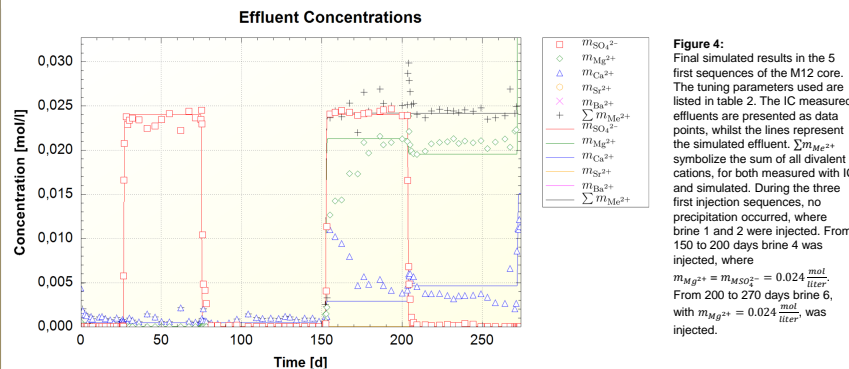
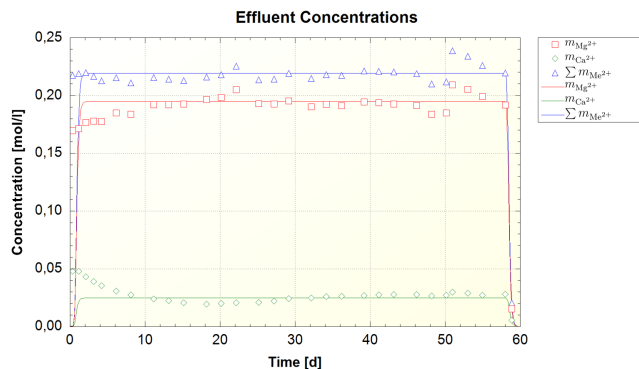


Figure 5: Final simulated results in the last 5 sequences of the M12 core. The tuning parameters used are listed in table 2. The IC measured effluents are presented as data points, whilst the lines represent the simulated effluent. $\sum m_{Mg^{2+}}$ symbolize the sum of all divalent cations, for both measured with IC and simulated. From 270 to 420 days the injected brine 7 had $m_{Mg^{2+}} = 0.120 \frac{mol}{liter}$. From 420 to 445 day brine 8 with $m_{Sr^{2+}} = 0.120 \frac{mol}{liter}$. During the period 445 to 470 days, and 496 to 522 day, brine 9 with $m_{Ba^{2+}} = 0.060 \frac{mol}{liter}$ was injected. From 470 to 496 days brine 10 with $m_{Ca^{2+}} = 0.120 \frac{mol}{liter}$ was injected.

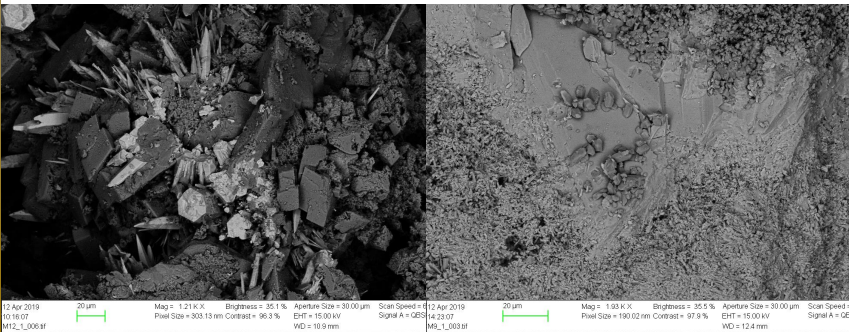


Figure 6: SEM analysis indicating the presence of secondary minerals such as witherite (BaCO₃) (left) and celestite (SrSO₄) (right).

Conclusions

- Reaction kinetic parameters from the literature require tuning parameters to match reactive flow experiments.
- Dissolution and precipitation, being two different mechanisms, require different sets of tuning parameters.
- The 1D ADR model produced good matching results for the effluent concentrations.
- The carbonate dissolution and precipitation reaction behave in a substitution-like manner.

Further work

- Extensive investigation of reaction kinetics of strontium and barium bearing carbonates.
- Perform less complex chalk core experiments.
- Perform geochemical analysis, e.g. XRD, to evaluate what minerals that are formed.

References:

- Korsnes, R. I., & Madland, M. V. (2017) The Effect on Compaction Rates by Divalent Anion and Cations on Outcrop Chalk Tested at Reservoir Temperature and Effective Stress Conditions. In Poromechanics VI (pp. 706-714).
- Megawati, M., Madland, M. V., & Hirth, A. (2015). Mechanical and physical behavior of high-porosity chalks exposed to chemical perturbation. Journal of Petroleum Science and Engineering, 133, 313-327.
- Andersen, P., Wang, W., Madland, M., Zimmermann, U., Korsnes, R., Bertolino, S., Minde, M., Schulz, B., and Gilbricht, S. (2018). Comparative study of five outcrop chalks flooded at reservoir conditions: Chemo-mechanical behaviour and profiles of compositional alteration. Transport in Porous Media, 121(1):135-181.

Contact information

Magnus Kongestøl
Raaholt
+47 995 70 407
magnusraaholt@gmail.com